**CENTRO DE INVESTIGACIÓN Y DE ESTUDIOS AVANZADOS DEL INSTITUTO POLITÉCNICO NACIONAL**

Unidad Mérida

**DEPARTAMENTO DE FÍSICA APLICADA**

# “Evaluación de 3 fases cristalinas de TiO2 para la fabricación de celdas fotovoltaicas flexibles sensibilizadas con colorante para su aplicación en interiores”

TESIS

Que presenta

**Roberto Carlos Avilés Betanzos**

Para obtener el grado de

**Doctor en Ciencias**

en

**Fisicoquímica**

Director de Tesis:

**Dr. Gerko Oskam**

Mérida, Yucatán, México Mayo de 2024

**CENTRO DE INVESTIGACIÓN Y DE ESTUDIOS AVANZADOS DEL INSTITUTO POLITÉCNICO NACIONAL**

Unidad Mérida

**DEPARTMENT OF APPLIED PHYSICS**

# "Evaluation of 3 crystalline phases of $TiO_2$ for the fabrication of flexible dye-sensitized photovoltaic cells for indoor application"

THESIS

Presented by

**Roberto Carlos Avilés Betanzos**

To obtain the degree of:

**Doctor of Science**

in

**Physical Chemistry**

Thesis Director:

**Dr. Gerko Oskam**

Merida, Yucatan, Mexico May 2024

**AKNOWLEDGMENT**

Thanks to my parents and my brothers Wilson Avilés, Tomasa Betanzos, Kevin Avilés and Miguel Avilés for all the support they have given me.

Thank you Dr. Gerko Oskam for giving me your trust and above all for your support both inside and outside the laboratory.

I thank the National Council of Science and Technology for the financial support received during this time.

I thank the Center for Research and Advanced Studies of the National Polytechnic Institute Unidad Mérida for allowing me to use its facilities and giving me the opportunity to develop academically.

I thank Dr. Román Castro for having motivated me to continue with my academic training.

Thanks to Dr. Marina Freitag for her friendship, advice and teachings that were valuable for the development of this work. Thank you for allowing me to use the facilities in your laboratory at the University of Newcastle, Newcastle Upon tyne, England. To your entire work group for giving me your friendship and teachings.

Thank you Dr. Dena Pourjafari because, despite having a very complicated schedule, I could always count on you. Thank you for guiding me through this work, for your advice, teachings, for always having a positive attitude, for having so much patience with me, but above all for your friendship.

Thank you Dr. Wendy Padrón and Dr. Diecenia Peralta for your advice, teachings, your patience, your friendship and for all the invaluable support you gave me during this work.

Thanks Dr. Renan Escalante and Dr. Alberto Vega for helping me clarify doubts and guiding me in the use of laboratory equipment.

The analysis presented in this thesis were carried out at the National Laboratory of Nano and Biomaterials, CINVESTAV-IPN; funded by the projects FOMIX-Yucatán 2008-108160, CONACYT LAB-2009-01-123913, 292692, 294643, 188345 and 204822. I thank Dr. Patricia Quintana for access to LANNBIO, M.C. Daniel Aguilar Treviño for obtaining the diffractograms and M.C. Mario Herrera Salvador for corrective maintenance of the D-8 Advance diffractometer

Thanks to Dr. Victor Rejón Moo from CINVESTAV-Mérida and Dr. Isabel Arce García from Newcastle University for the SEM images.

Thanks to my laboratory colleagues for advising me and sharing their experience in laboratory work. All contributed to the improvement in the experimental setups and in the interpretation of the results obtained.

Thanks.

## RESUMEN

El enfoque principal del trabajo es la fabricación celdas solares flexibles sensibilizadas con tinte sobre sustratos plásticos conductores (ITO-PEN) mediante procesos escalables, energéticamente sostenibles y utilizando materiales no tóxicos para su aplicación en la generación de energía eléctrica en ambientes de interiores. Para esto se exploró la preparación de pastas acuosas de $TiO_2$ libres de surfactantes para la elaboración de fotoelectrodos que puedan ser químicamente sinterizados a bajas temperaturas de 120 °C, en lugar de 500°C generalmente usado. En este trabajo se realizó la síntesis de las 3 fases cristalinas de $TiO_2$ (anatasa, rutilo y brookita), su caracterización estructural y su evaluación como película activa en fotoelectrodos tanto rígidos como flexibles. El trabajo se divide en tres partes, en la primera parte se buscó una formulación adecuada del electrolito que pudiera hacer que una DSSCs que utiliza una película sinterizada a baja temperatura funcione de manera correcta. Tres diferentes formulaciones de electrolito con el par redox de yoduro/triyoduro fueron evaluadas utilizando una pasta acuosa de baja temperatura (pasta A). En la segunda parte, la formulación de la pasta A fue modificada con el fin de obtener una película más homogénea y transparente (pasta C). Fotoelectrodos preparados con esta pasta seleccionada se sensibilizaron con un tinte orgánico de alta eficiencia (Y123) y la configuración fue evaluada utilizando la formulación óptima del electrolito de yoduro descubierta y comparada con un par redox basado en un complejo de cobre. Posteriormente, se realizaron caracterizaciones fotovoltaicas de los dispositivos en condiciones simuladas de exteriores e interiores y se utilizó de impedancia electroquímica para tener un mejor entendimiento del funcionamiento interno de estas configuraciones de baja temperatura. La tercera parte del trabajo se centra en la fabricación de pastas de anatasa y brookita para la fabricación de DSSCs de alta eficiencia con lo que se demuestra

la viabilidad de los materiales sintetizados para producir dispositivos con un gran potencial para competir con las eficiencias récord actuales.

## ABSTRACT

The main focus of the work is the fabrication of flexible dye-sensitized solar cells on conductive plastic substrates (ITO-PEN) through scalable, energetically sustainable processes and using non-toxic materials for their application in the generation of electrical energy in indoor environments. For this, the preparation of aqueous binder-free $TiO_2$ pastes was explored for the preparation of photo electrodes that can be chemically sintered at low temperatures of 120 °C, rather than generally used 500 °C. In this work, the synthesis of the 3 crystalline phases of $TiO_2$ (anatase, rutile and brookite), their structural characterization and their evaluation as an active film on both rigid and flexible photo electrodes was carried out. The work is divided into three parts, in the first part a suitable formulation of the electrolyte that could make a DSSCs that uses a film sintered at low temperature to work properly was explored. Three different electrolyte formulations using the redox pair iodide/triiodide were evaluated using a low-temperature aqueous paste (paste A). In the second part, the formulation of paste A was modified in order to obtain a more homogeneous and transparent film (paste C). Photo electrodes prepared with this paste were sensitized with a high-efficiency organic dye (Y123) and the configuration was evaluated using the optimal iodide electrolyte formulation discovered and compared using a copper complex based redox pair. Subsequently, photovoltaic characterizations of the devices were carried out in simulated outdoor and indoor conditions and electrochemical impedance characterizations were used to have a better understanding of the internal functioning of these low-temperature configurations. The third part of the work focuses on the preparation of anatase and brookite pastes for the manufacture of high-efficiency DSSCs, which demonstrates the viability of the synthesized materials to produce devices with great potential to compete with current record efficiencies.

**CONTENT**

## LIST OF FIGURES

## LIST OF TABLES

# INTRODUCTION

## 1. General

In this section, a general overview of the thesis topic and fundamental concepts of photovoltaic technology with a focuss on dye-sensitized solar cells will be presented. Additionally, the most relevant works carried out by various research groups regarding the development of different methodologies for the preparation of plastic photoelectrodes for flexible DSSCs will be shown.

### 1.1. Global situation

The world's population is constantly increasing and the current growing energy requirements of modern technological advancements associated with this have become in an urgent demand for a greater supply of energy [1][2]. This urge in energy consumption has created a need for clean and sustainable energy production, and avoid the use of fossiel fuels which are currently the world's primary sources of energy and are becoming increasingly scarce and depleted with time. Because of this situation, there is an increase in environmental problem, such as greenhouse effects, air and water pollution, among others [3][4]. Concerns about the environmental consequences have led to the scientific community to develop non-polluting, abundant, and cost-effective energy sources while simultaneously, mitigate the effects of climate change and enable a shift towards a society based on renewable energy in the near future [5][4].

## 1.2 Renewable Energy

Renewable energy (RE) resources old great potential to meet the present world energy demand. They can enhance diversity in energy supply markets providing commercially attractive options to meet specific needs for energy services (particularly in developing countries and rural areas), and offer possibilities for local manufacturing of equipment while securing long-term sustainable energy supply and reducing global atmospheric emissions. Different types of RE, are currently being used for global sustaoinable and clean energy production, such as, wind energy, geothermal energy, energy produced by the fall of water in damps, energy produced by waves and ocean currents, etc. However, among all the available sources of renewable energy, solar energy stands out as the one with the greatest potential to meet the demands of our modern world since the energy coming from the sun can potentially meet the global energy consumption [6][7][8].

## 1.3. The sun as a clean energy source

The fusion reactor nature of the sun (hydrogen transformed to helium due to gravitational forces) determines the energy produced in the interior of the solar sphere which is radiated out to the space at temperatures of many millions of degrees. This energy emitted in the form of solar radiation is the result of the several layers that emit and absorb radiation of various wavelengths. The energy of a photon ($E_{ph}$) is proportional to the frequency ($v$) by a factor of $6.626 \times 10^{-34}$ Js, called the planck constant $h$:

$$E_{ph} = h \cdot v \tag{1}$$

The wavelenght $\lambda$ of the light is proportional to the reciprocal frequency given by:

$$\lambda = \frac{c}{v} \tag{2}$$

Where $c$ is the speed of the light (2.99 x $10^8$ m/s) and to get the energy in electron volts units, we must devide by the elementary charge $q$ (1.6 x $10^{-19}$ As) so we can easiliy transform $\lambda$ to $E_{ph}$:

$$E_{ph} \cdot \lambda = \frac{h \cdot c}{q} = 1240\ eV \cdot nm \tag{3}$$

The extraterrestrial solar radiation emitted by the sun and its distance to the earth result in a nearly constant intensity of solar radiation outside of the earth's atmosphere and, in conjunction with its spectral distribution, have been measured by various methods. Total solar irradiance (TSI) is defined a the measure of the solar power over all wavelengths per unit area incident on the earth's upper atmosphere perpendicular to the incoming sunlight at a distance of one astronomical unit ($1.495 \times 10^{11}$ m, the mean earth-sun distance) and is valid for the temporal changes in the sun's instantaneous output. The National Renewable Energy Laboratory in the 2000 ASTM Standard Extraterrestrial Spectrum Reference E-490-00, through several measurements, has stablish a value for the TSI of 1366.1 W/m$^2$. The term solar constant $G_{SC}$ is used only to describe the long-term mean value of TSI and it can be approximated to the spectrum of a black body at a temperature of 5973 K [9][10][11].

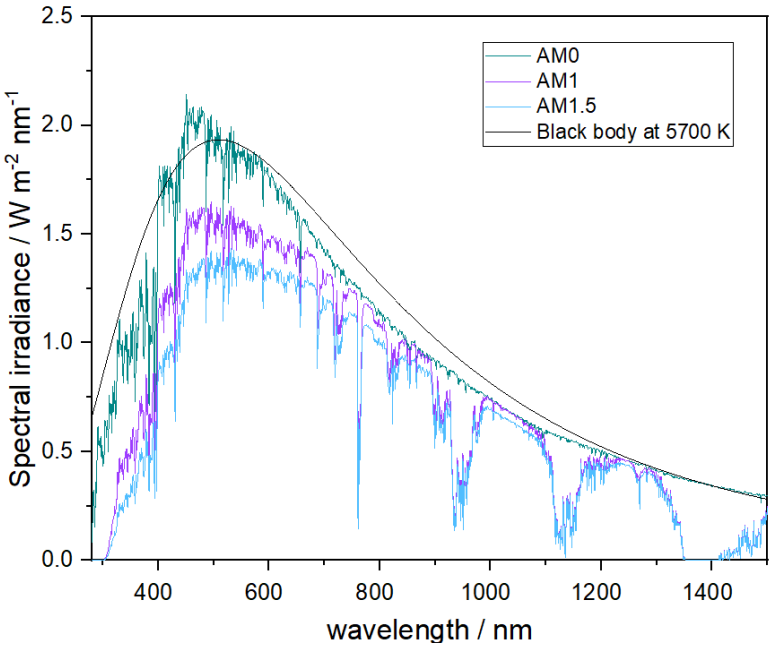


Figure 1. Sun spectral irradiance outside the earth's atmosphere (AM0), on earth's zenith angle of 0° (AM1), at 48.2° (AM1.5) and black body spectral irradiance at 5700K. Raw data taken from https://www.nrel.gov/grid/solar-resource/spectra-am1.5.html.

The intensity of the solar radiation, in its way towards the earth, is attenuated by the atmosphere when it passes through due to scattering by air molecules, dust particles and absorption by ozone, $CO_2$ and $H_2O$. The amount of attenuation depends on the path length of the ray through the atmosphere is expressed in terms of air mass AM. AM0 correspond to the radiation without atmosphere or extraterrestrial irradiation, AM1 is defined as the ratio of the mass of atmosphere through which beam radiation passes to the mass it would pass through if the sun were at the zenith (i.e., directly overhead) when zenith angle ($\theta_Z$) is zero and AM1.5 correspond when the sun is at a zenith angle of 48.2° (equation 4). The solar irradiance at AM1.5 is 1 kW/m$^{-2}$, typically referred to as AM1.5G, where G is defined as the sum of direct and scattered light of the global radiation.

$$AM = \frac{1}{cos\theta_Z} \quad (4)$$

The sun's energy that reaches the earth's surface every year amounts to an astounding 3.8 million exajoules, which is more than enough to satisfy the entire global energy demand. Moreover, the use of solar energy for electricity generation is not only environmentally safe, but also exceptionally clean [12][13].

In this regard, photovoltaic (PV) technology has emerged as a promising contender for a low-consumption future of sustainable electricity production and reduce the dependence of fossil fuels consuption due to its ability to convert solar radiation into electrical energy, a phenomenon known as the photovoltaic effect [14][15][16][17][18].

### 1.4. Generations of photovoltaic (PV) technology

Nowadays, the world is getting closer to meet the objective of transitioning towards a sustainable energy-dependent societ thanks to the efforts of the scientific community and the significants advances of the PV technology. It is expected that solar energy could reach 15-30% of the total globalenergy production by the year 2050. Solar power continues to lead the way in this important effort, and the progress has sorted it into three different stages: first, second, and third generations. [19] [20][21] [22][23].

### 1.4.1.. First generation solar cells

The first generation of photovoltaic solar cells (1G) is predominantly comprised of light absorbing semiconducting material crystalline silicon wafers [24]. These cells were the first modern approachc in the solar technology and paved the way for further advancements. Silicon (Si) is the most widely used material for commercial PV owing to their large-scale integration, good performance, stability which renders them exceptional commercial efficiency and extensive utilization representing almost 90% of the photovoltaic solar cell industry [25][26][27] [28][29][30].

This technology can be further subdivided into three main groups: single-crystalline or mono-crystalline (mc-Si), poly-crystalline (pc-Si) silicon solar cells, and multi-junction (mj) solar cells.

### 1.4.2. Second generation solar cells

These technologies include amorphous silicon and various inorganic semiconductor materials like thin-film gallium arsenide (GaAs), copper indium gallium selenide (CIGS), cadmium telluride (CdTe), and copper indium selenide ($CuInSe_2$). The main focus of 2G technology is to reduce costs even more, an important issue for 1G, which was achieve this by using thin-film technologies with direct bandgap materials that absorb more light. These improvements have brought performance on par with traditional silicon devices and expanded the range of PV technologies available [27][31].

The thin films, usually just a few microns thick, contribute significantly in reducing costs because they use less material compared to wafer-based technology [32]. However, even though there have been advancements in 2G, there are still present some issues. One major drawback is that while the best results are comparable to 1G, commercially available 2G solar cells often do not perform as well. Additionally, 2G solar cells degrade faster in sunlight, which can make them unsuitable for certain outdoor uses. [33]. Moreover, the manufacturing and environmental expenses associated with both 1G and 2G solar cells remain significant and there are still issues related to the availability and toxicity of raw materials. For example, the scarcity of tellurium (Te) and gallium (Ga) contributes to high production costs, while concerns about the toxicity of cadmium (Cd) and arsenic (As) restrict their usage [34][35].

### 1.4.3. Third generation solar cells

Third-generation solar cells (3G) represent a significant advancement in solar cell technology since 1990, after more than twenty years of research and development. [36]. These advanced cells demonstrate the progress made in solar cell technologies and are continually advancing towards reaching their maximum potential. [37]. Currently, third-generation solar cells are attracting considerable attention from the scientific community because of their benefits compared to traditional solar devices. These advantages include the possibility of lower processing costs, faster payback periods, and environmental sustainabilit holding great promise for minimizing the environmental footprint of energy generation. [23].

Another attractive aspect of 3G PV is their often cheaper manufacturing methods, making them a promising alternative because they could produce highly efficient devices for converting light into electricity at a lower cost [38][39][3]. The 3G photovoltaic technology is expected to have a significant impact on the renewable energy sector particularly in energy supporting applications, such as building-integrated PV, other product-integrated and portable devices. It is also well suited for various recent developments, including IoT (Internet-of-Things) applications [40][41].

This most recent generation of photovoltaic systems include key technologies, such as, organic solar cells (PCE ≈ 19.2%), quantum dot solar cells (PCE ≈ 18.1%), perovskite solar cells (PCE ≈ 26%) and dye-sensitized solar cells (DSSCs, PCE ≈ 13%) [14]. However, it is important to note that each of these technologies has its own advantages and disadvantages [42]. Table 1 summarizes the PV generations, efficiencies, as well as main advantages and disadvantages .

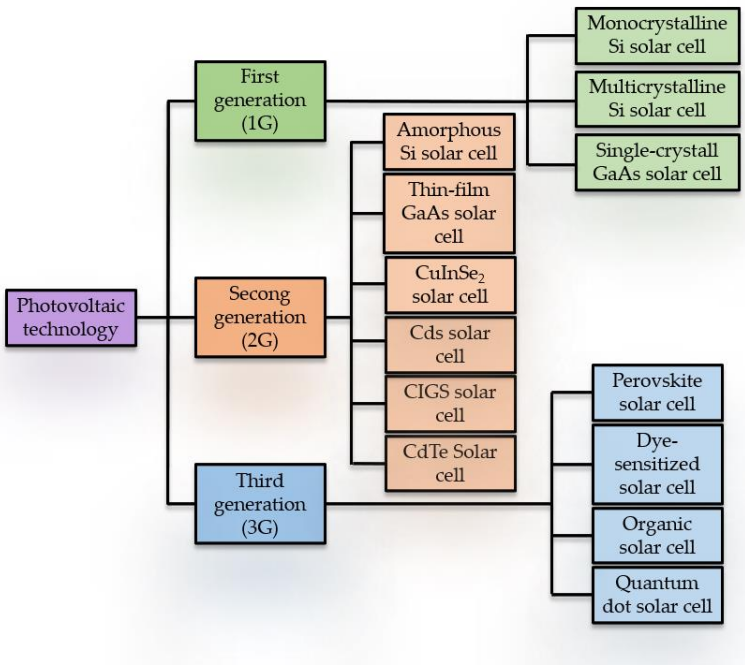


Figure 2. Schematic representation of the three generations of photovoltaic technologies [43].

Table 1. An overview of the three generations of photovoltaic technologies is presented. Main advantages and disadvantages are highlighted.

| Photovoltaic Generations | Technology | Advantages | Disadvantages | Efficiency (%) * |
|---|---|---|---|---|
| 1G | Monocrystalline Si solar cell | Stability<br>High performance<br>Long service life | High manufacturing cost<br>Temperature sensitivity<br>Absorption issues<br>Material loss | 26.8 |
| | Multicrystalline Si solar cell | Simple manufacturing procedures<br>Profitable<br>Decreased silicon waste | Lower efficiencies than MSi-cell<br>High temperature sensitivity | 23.3 |
| | Single-crystalline GaAs solar cell | High electron mobility<br>High thermal stability<br>Efficient light absorption | Expensive production cost<br>Small ingot size<br>Brittle waffers | 27.8 |
| 2G | Thin-film GaAs solar cell | High stability<br>Low temperature sensitive<br>Better absorption than MSi-cell<br>High efficiency | Extremely expensive | 29.1 |
| | Amorphous Si solar cell | Less expensive<br>High availability<br>Non-toxic<br>High absorption coefficient | Lower efficiency<br>Difficult for dopant materials<br>Poor minority of carrier life-time | 14.0 |
| | CdTe solar cell | High absorption rate<br>Less material required | Lower efficiency<br>Cd extremely toxic<br>Temperature sensitive | 22.3 |
| | CIGS solar cell | Less material required | Expensive<br>Not stable<br>Temperature sensitive | 23.6 |

| | | | | |
|---|---|---|---|---|
| | | Low production cost | Low stability | |
| | Dye-sensitized solar cell | Easy manufacture process | Use of volatile solvents | 13.0 |
| | | High efficiency in Low light operation | | |
| | | Lower internal temperature operation | | |
| **3G** | | Low production cost | | |
| | Organic solar cell | Light weight | Low efficiency | 19.2 |
| | | Thermal stability | | |
| | Quantum dot solar cell | Low production cost | High toxicity | 18.1 |
| | | Low energy consumption | Degradation | |
| | Perovskite solar cell | Low cost-simplified structure | Unstable | 26.0 |
| | | High efficiency | Toxic materials | |

* Efficiencies reported according to 2024 NREL efficiency chart [44].

### 1.5. Dye-sensitized solar cells

Dye-sensitized solar cells (DSSCs) are notable electrochemical devices among other 3G solar cell technologies tha resemble the photosynthesis in plants [37]. DSSCs are the first 3G technology that has caught a lot of attention as a new solar technology because they could be cheaper to make and easier to produce [14]. Even though research on DSSCs started more than 30 years ago, there have been big improvements recently, with a lot of work put into making them work better both outside and indoors [45].

The development of DSSC technology started back in 1972 with a solar cell using chlorophyll-sensitized zinc oxide, facing limitations due to low efficiency, absorbing only 1% of sunlight with a single layer of dye molecules [46][39]. However, a significant breakthrough occurred in 1991, boosting efficiency to 7.1% and converting about 80% of absorbed photons into electricity. This was achieved by introducing a new dye sensitizer paired with a nanostructured, mesoporous $TiO_2$ structure, as documented in Nature by O'Regan and Grätzel [47][15].

DSSCs, also known as Grätzel cells, have gained attention for mass production because of several benefits: they can be made using cheap and readily available materials, and they are produced through a simple, fast screen-printing process, not requiring a vacuum [4][48][49]. DSSCs can withstand environmental impurities, making them easy to manufacture and process in regular conditions. Recently, spectacular improvements have been reported, showing an efficiency of 15% under solar illumination [50]. Additionally, there's a move towards making DSSCs on lightweight flexible substrates like plastic or metal foils. [51][19]. Unlike glass electrodes, which have limits due to fragility, weight, and shape, flexible DSSCs maintain the attractive qualities of rigid ones (translucency and polychromaticity), and can be used on curved surfaces like clothing, bags, car roofs, and sensors [52][3]. FDSSCs offer the potential for significant cost reduction as they are compatible with large-scale roll-to-roll processing and low-cost industrial methods to print dye-sensitized solar cells. In addition, the whole processes can be done at low temperature and under atmospheric pressure [4]][53]. Using flexible materials becomes more important for meeting the need for a fast solar devices manufacturing, with flexible materials, the industry can speed up production and make a large amount of panels needed for solar technology to succeed [54].

rrently, silicon-based solar cells are leading the market for outdoor solar panel applications because they can match the natural sunlight's spectrum which makes them absorb and convert solar energy efficiently, maximizing power generation and potential efficiency [55][56]. However, silicon solar cells do not work as well indoors because the indoor lighting spectrum does not match well with their spectral sensitivity [20]. DSSCs, on the other hand, are in fact better aligned with the spectral characteristics of indoor lighting, allowing them to effectively harness and convert available indoor light for energy generation in both indoor and outdoor conditions [57].

DSSCs have a remarkable ability to work well even with diffuse ambient light, including light during dawn, dusk, or on cloudy days, which usually does not get used [25]. When thet are subjected to low-intensity irradiation (0.3–0.5 sun), the efficiency of DSSCs is comparable to that of silicon-based solar cells [56]. The superior performance under low intensity illumination and because they can be optimized to work with the spectrum of light emitted by indoor fluorescent and LED lights (400-650nm), DSSCs are one of the best options for capturing indoor light which have led to energy conversion efficiencies of over 32%. [21][58][59][57].

### 1.5.1. DSSC elemental structure

The dye-sensitized solar cell is composed of four fundamental components that are essential for its effective operation. In the following, the components are detailed.

### 1.5.2. DSSC components

In this section, the main components of DSSCs are described.

#### 1.5.2.1.. Working electrode

The photoelectrode consists of a substrate onto which a mesoporous oxide layer (MOL) is deposited. This layer facilitates the transfer of electrons generated by the absorption of sunlight by the sensitizer. Extensive research and development efforts have been undertaken to formulate the photoanode in DSSCs, exploring diverse materials such as ZnO, $Nb_2O_5$, $SnO_2$, and $WO_3$. These nanostructured materials have been synthesized in variety of different morphologies such as nanotubes, nanorods, nanowires and nanocrystals. with the aim of amplifying dye adsorption and optimizing electron injection [60]. Among these materials, titanium dioxide, also known as titanium (IV) oxide or titania, is highly attractive for next-generation solar cells due to Their exceptional transparency across the visible spectrum, remarkable stability, non-toxicity, and substantial specific surface area [61].This inorganic compound with the chemical formula $TiO_2$, stand out as the most promising candidate for DSSCs.

$TiO_2$ is cheap, non-toxic, chemically stable, and easily accessible in big numbers. Typically used in DSSCs as a mesoporous architecture film with a large surface area deposited onto the TCO, it satisfies the crucial requirement of generating high carrier mobility within the cell, thereby reducing electronic transport resistance. It is the basic ingredient in white paints, cosmetics, sunscreens, and other products. The $TiO_2$ film's structural characteristics are crucial since mesoporosity increases the amount of dye molecules that may be adsorbed over its wide surface

area, which raises the DSSC's incident light absorption percentage and the higher the crystallinity (achieved at high-temperature thermal treatments, above 400 °C) decreases the defects in the lattice minimizing electron losses, the higher the crystallinity of $TiO_2$.

Titanium dioxide is slightly oxygen deficient, $TiO_{2-x}$ (x=0.01).The material is an n-type semiconductor because of this slight oxygen shortage, which may be brought on by $Ti^{3+}$ contaminants. It exists in three well-known polymorphs that are also found in nature: a) anatase, b) rutile and c) brookite.

Anatase is one of the titanium dioxide crystalline phases with a tetragonal crystal structure with a band gap typically of 3.20 eV with a negative conduction band edge at -0.50 eV Vs NHE. Rutile has one of the highest refractive indices at visible wavelengths of any known crystal and also exhibits a particularly large birefringence and high dispersion with a tetragonal crystal structure with a band gap typically of 3.52 eV with a negative conduction band edge at -0.42 eV Vs NHE . Brookite is the orthorhombic variant of titanium dioxide, which occurs in four known natural polymorphic forms with a band gap typically of 3.26 eV with a negative conduction band edge at -0.49 eV Vs NHE (minerals with the same composition but different structure). Brookite is rare compared to anatase and rutile and, like these forms, it exhibits photocatalytic activity and also has a larger cell volume than either anatase or rutile.

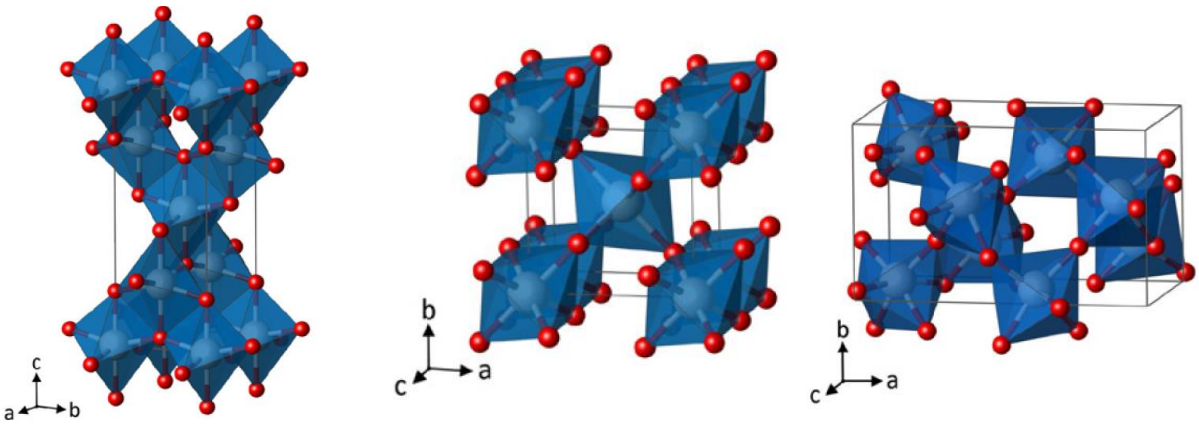


Figure 3. $TiO_2$ polyforms. a) Anatase, b) rutile and c) brookite [62].

$TiO_2$ is typically synthesized by sol-gel which is a one of the simplest ways to make $TiO_2$ nanoparticles from the Ti(IV) alkoxides' breakdown. The hydrolysis of titanium(IV) alkoxides is a general reaction that yields nanocrystalline anatase and can be written as follows:

$$Ti(OR)_4 + 2H_2O \rightarrow TiO_2 + 4ROH \quad (5)$$

where R is an alkyl, most commonly an isopropyl, butyl, or ethyl group. The nanocrystals are then treated by hydrothermal growth and peptization. The main advantage of this method is because it works at low temperatures and pressures allowing for adjusting optical and physical properties of materials as needed. The factors that affect the type of nanostructures produced include the temperature, time, pressure, and type of solvent used in the reaction. Additionally, the particles morphology and crystallinity can be changed by adjusting the chemical composition and pH of the solution. Depending on the chemicals and conditions used, this method offers flexibility in controlling the properties of the nanoparticles [63], [64], [65], [66].

#### 1.5.2.2. Dye sensitizer

The sensitizer is a thin layer of dye molecules adsorbed to the surface of the mesoporous oxide layer and its function is to capture sunlight and inject electrons to the oxide layer. Via functional groups and a variety of interactions, including covalent bonds, electrostatic interactions, hydrogen bonds, van der Waals forces, etc., the dyes are bonded to the surface of $TiO_2$ particles. The carboxyl groups of the dye and the hydroxyl groups on the surface of $TiO_2$ form the strongest and most stable couplings. The carboxyl groups are responsible for immobilizing the sensitizer on the nanocrystalline surface of $TiO_2$, acting as anchors. This allows for large quantum yields to occur during the electron transfer processes of the excited state of the dye molecule. Thus, The bonding structure of the dye molecules adsorbed on the semiconductor surface has a significant impact on the efficiency of electron injection into the $TiO_2$ conduction band [67].

The efficiency of the DSSC mainly depends on the molecular structure of the dyes and this are categorized into three types: inorganic, organic and natural dyes in based with their structural configuration. Inorganic dyes, like ruthenium (Ru) based coordination complexes are highly efficient and provide the best results, although they are very expensive and hard to purify. Natural dyes are promising for DSSCs because they are easy to make, easy to find, cheap, biodegradable, pure, reduce the need for expensive metals, can be made with simple chemicals. However, they do not generate as much electricity producing devices with efficiencies below 2% [68][69][70].

Because DSSC efficiencies has reached  over 10%, there has been a recent increase in interest in organic dyes, such as Y123, as photosensitizers [71], [72][73]. They are popular because of their large molar absorption coefficient, easy tunable redox potential through molecular structural diversification, and comparatively cheap cost. Additionally, this kind of sensitizer displays a mechanism that inhibits electronic recombination through a push-pull design. In this mechanism, when dye molecules are excited by light absorption, the acceptor groups transfer the negative charge density of the molecule from the electron donor group to the semiconductor surface. By preventing back electron transfer to the dye and enhancing electron injection to the semiconductor conduction band, this process facilitates dye regeneration by the redox pair in the electrolyte [74], [75], [76].

**1.5.2.3.. Electrolyte**

In an electrochemical device, the substance known as the electrolyte facilitates ionic conductivity between the positive and negative electrodes. The electrolyte's primary roles in the DSSC is to regenerate the oxidized dye and act as an internal conducting channel that promotes ion transport between the photoelectrode and the counter electrode through diffusion. Important DSSC properties, such as, stability and energy conversion efficiency are significantly impacted by the electrolyte, for example,  electrolyte's redox potential influences the $V_{OC}$, and the transit of the redox pair components within the electrolyte influences the $J_{SC}$, FF is influenced by the diffusion of charge carriers and the resistance to charge transfer at the electrolyte/electrode interface. The size of the redox species, the solvent's viscosity, the redox mediator's concentration, and the spacing

between the electrodes are some of the variables that can significantly affect the final performance of a DSSC [77].

Typically, the most popular transport medium in conventional DSSCs are liquid electrolytes, which has also yielded the highest efficiencies, although solid-state have lately gained a lot of attention. Important features on liquid electrolytes include low viscosity (which reduces resistance to charge carrier transfer), excellent conductivity, good interfacial wetting between the electrodes, and ease of preparation. The organic solvent, the redox pair, and additives make up the liquid electrolyte of a conventional DSS having each of these three components a distinct function in the photovoltaic functioning of DSSCs. Additives are added to the electrolyte in order to optimize the photovoltaic performance of the DSSC. Small amounts of electronic additives can greatly alter the photovoltaic parameters of a cell. The organic solven is the setting where the redox couple's ions dissolve and spread. Because acetonitrile (AN) and valeronitrile (VN) have a high dielectric constant, their combination at a volume ratio of 85:15 (AN:VN) is the most widely used formulation [78][79].

A DSSC's redox electrolyte is an essential part that influences the device's long-term stability and cell performance. The reduced species of the redox pair is in charge of regenerate the photoexcited dye again to its groung state during the DSSC photo electrochemical cycle. The produced oxidized species then diffuse to the counter electrode, where they undergo reduction. The most used redox shuttle in DSSCs is iodine electrolyte, which has produced a maximum PCE of 12.4% under one sun's illumination [80]. Because transition-metal complexes like Co complexes increase the open-circuit voltage ($V_{OC}$) of the device, they have cought a lot of attention as redox shuttles. However, there are still issues with slow mass transfer and significant reorganization energy required. Cu

complexes have drawn a lot of interest lately. Using an $[Cu(tmby)]^{+}/[Cu(tmby)_2]^{2+}$ redox shuttle and cosensitized organic dyes, a record solar cell achieved an efficiency of 15.2% with a high $V_{OC}$ of over 1 V under simulated 1-sun irradiation [50]. When combined with organic dyes and a PEDOT counter electrode, the more positive redox potential of Cu redox pairs provides a greater $V_{OC}$ to the DSSC, which is the primary benefit of utilizing them in the electrolytes. Though they seem promising, caution should be exercised when utilizing them because research has indicated that these particular redox couples are more likely to enhance electronic recombination in DSSCs [81][82][83][84][85].

#### 1.5.2.4. Counter electrode

Usually made of glass or plastic, the counter electrode is fluorine-doped tin oxide (FTO) or indium tin oxide (ITO), covered in a catalyst substance that promotes electrocatalytic activity to minimize the oxidized species of the redox mediator by reducing the oxidized form of the mediator through the flow of electrons from the external circuit. There is currently a wide variety of materials available for the fabrication of these components as a result of the scientific community's intensive research efforts in this subject. The most suitable ones are platinum (Pt), carbon materials (graphite, activated carbon, black carbon, single-walled carbon nanotubes), and poly(3,4-ethylenedioxythiophene) (PEDOT), as they have demonstrated appropriate characteristics as counter electrodes. In this regard, PEDOT-based counter electrodes are a very competitive and effective substitute because of their many benefits, including excellent structural flexibility, low cost, stability, outstanding conductivity (750 S/cm), and exceptional transparency to visible light and that they can maintain an electrocatalytic actividad in film thicknesses of up to 240 nm [45].

The deposition of this material must be carried out on flexible plastic substrates using an appropriate and straightforward method that has high electrocatalytic activity and strong chemical stability for the redox reactions. Electrochemical polymerization is a widely used technique for depositing PEDOT onto conductive plastic surfaces. This approach has the advantage of being able to operate at low temperatures and using water as a solvent, which is a non-toxic material, easyly scalable solution perfect for applications involving the manufacture of DSSC in industrial settings. This makes the use of PEDOT as a counter electrode a viable option for manufacturing flexible DSSCs on plastic substrates [86], [87], [88].

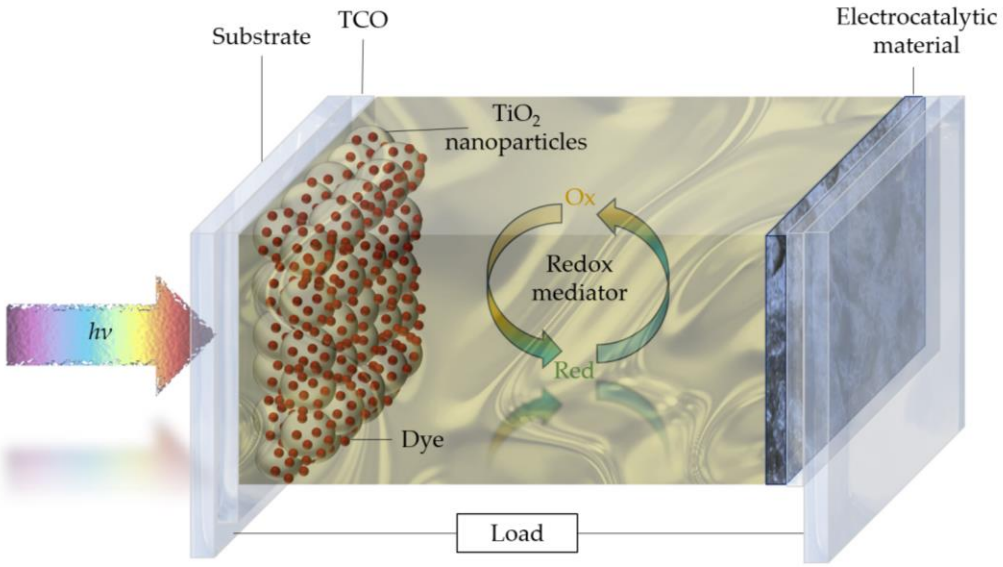


Figure 4. Schematic representation of the main components of a DSSC [43].

.

### 1.6. Ambient photovoltaics

DSSCs have outperformed other solar cell technologies in diffuse light and even artificial lighting such as light-emitting diodes (LEDs), fluorescent (FL) tubes, and halogen tubes installed mostly inside buildings, due to their superior spectral match in the visible region and their remarkable ability to sustain a high photovoltaic even under these conditions [89]. The intensity of standard interior lighting ranges from 200 to 2000 lux and comparing the solar irradiance is equivalent to around 1% of the typical AM 1.5G although iluminance is related to the human eye perception (photonic eye response) rather than power [21][90], [91], [92], [93], [94].

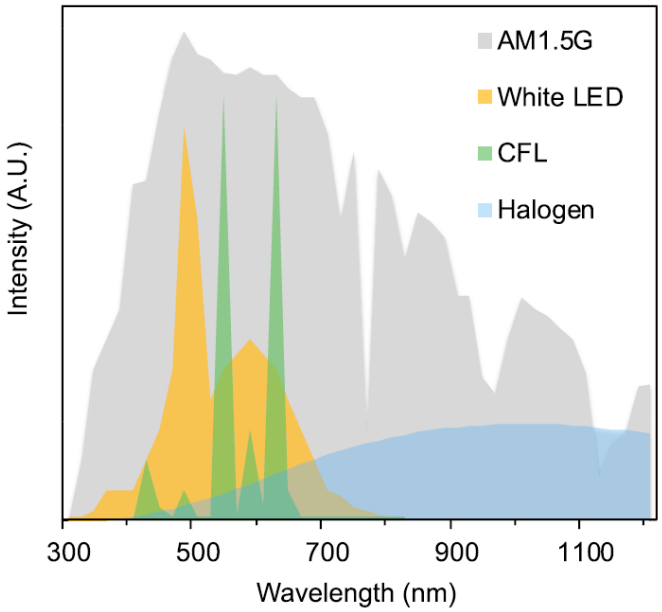


Figure 5. Different light sources spectra, AM1.5G (grey), White LED (yellow), Compact fluorescent lamp (CFL, green) and halogen lamp (blue)[95].

Commercially, their reasonable stability in less demanding indoor conditions is acceptable and this is the main reason why The ASC's (Angstrom Solar Center) DSSC group have concluded that in order for this technology to gain hold in the market, needs to be focus first on interior applications, where the requirements for durability and efficiency are less strict than those for outdoor applications and a lifetime of at least 5 years is sufficient for consumers [1][96]. Wireless sensor nodes (WSNs), which are independent electronic devices with exceptionally low power consumption, are in high demand due to the recent rise of the IoT but the useful lives of conventional wired power sources and batteries are limited, necessitating ongoing maintenance and occasional replacement. In this regard, DSSCs have recently demonstrated exceptional power conversion efficiencies of 38% under 1000 lux indoor light conditions and 1.0 V open circuit voltage proving to be able to power this technology [92][37][21][89]. Moreover, there are sustainability benefits, by using domestic illumination to power small electronic gadgets the carbon footprint associated with use batteries and their disposal can be sustantially decreased, though the carbon footprint of alkaline battery production is smaller than that of lithium-ion batteries, it is still present [8].

In this context, the commercialization of devices designed to operate in indoor lighting conditions is underway, pioneered by companies like Ambient Photonics, with a focus on IoT applications using DSSCs as the power source. In addition, FDSSCs can aslso be used in everyday indoor and diffuse light applications such as charging cell phone batteries, backpacks as showcasted by Gcell company [97]. This demonstrate  how small DSSC-powered gadgets represent a significant industry innovation by offering practical solutions for settings where artificial lighting or diffuse

light predominates, suggesting that this could be the potential future for indoor technology, with this type of solar cells leading the way.

### 1.7. Strategies for flexible photoelectrodes manufacturing

In this section, the most significant work in the field, including a wide range of studies that have made notable development and progress of current techniques for flexible, plastic-based DSSC (FDSSCs) will be presented. Pioneering works that have motivated the progress of the latest techniques as well outstanding and innovative works will be included. In addition, the most novel and cutting-edge techniques that have emerged in the scientific landscape will be presented.

#### 1.7.1. Low-temperature physical-chemical binding

Commercial P25 has been combined with binding agents like $TiCl_4$ or $[Ti(OiPr)_4]$. At low temperatures, Ti(IV) alkoxides can hydrolyze and crystallize inside the semiconductor oxide network, facilitating adhesion between the film and substrate and chemically connecting the titania nanoparticles [98][99][100]. Using acid-base chemistry to change the pH and chemically sinter the film involves introducing a small amount of ammonia solution to acidic $TiO_2$. This is another binder-free method. Increasing concentrations of $CH_3COO$- and $NH_4^+$ ions cause flocculation, which functions as a "electrolyte glue" [51]. As a result of hydroxyl groups forming on the $TiO_2$ surface after drying, there is an increase in connection between the particles, which causes a viscosity rise [100][101]. Using commercial Degussa P25 and hexafluorotitanic acid as a binding

agent, Holliman et al. described an aqueous paste that was binder-free and employed at low temperatures to chemically sinter $TiO_2$ particles. By using this method, the condensation protonation–dehydration processes on the $TiO_2$ surface and the formation of Sn–O–Ti bonds between the $TiO_2$ and ITO substrate enhanced the interparticle connection [102]. Another method that increases the crystallinity, surface area, and porosity of the film is surface modification of $TiO_2$ nanoparticles using trimethyloxysilane. When compared to bare $TiO_2$, the modified $TiO_2$ displayed a higher degree of dye loading because of a better interaction between the dye anchoring groups and the Ti-O-Si bonds as well as the free -OH groups of the $TiO_2$ nanoparticles [103].

Miyasaka et al.'s previous research on low-temperature binder-free coatings for FDSSC electrodes (<130 °C) was conducted using a colloidal solution made of two different-sized $TiO_2$ particles in *t*-butanol and water. The larger particles, which had an average size of about 200 nm and functioned as a material for light scattering, were held together by the smaller particles, which had an average size of about 60 nm, acting as a binding agent [104][105]. Moreover, other research groupss have employed a variety of particle sizes (small, medium, and big) to bind the medium-sized $TiO_2$ particles together by filling up the spaces between them; the larger particles serve as light scattering centers [106].

Researchers have combined commercial P25 with deionized water or dry ethanol and stirred for several weeks to alter the surface chemistry of bare P25 in order to create a homogenous and viscous dispersion [107]. Also, several hours of ball-milling the titania slurries have produced smaller agglomerates, fewer cracks, and more uniform films. Due to an increase in surface area, the ball-milled films show great mechanical stability and increased dye loading [100][101][108].

### 1.7.2. Film transfer techniques

Lift-off techniques have become a viablealternative to maintain interparticle connectivity because the lack of sintering in low-temperature films, which makes it difficult to provide effective particle interconnectivity. These method first sinter the material on a template, which is then transferred to an FPCS (flexible plastic conductive substrate) to ensure the appropriate interparticle connections,. In a lift-off approach described by Dürr et al., an electrode that has already been sintered is moved to a second plastic substrate while retaining its original electrical characteristics. They produced a glass substrate with a thin layer of gold (10–20 nm). A high-temperature annealed (>450 °C) $TiO_2$ layer was then placed on top of this. The material used for this transfer layer was a composite made up of one sublayer of $TiO_2$ rods in the top section and one sublayer of spheres in the lower part. The mechanical qualities are improved by this mix of morphologies, leading to an improved lift-off procedure [109]

.

Kafafi and colleagues have deposited mesoporous $TiO_2$ films onto ITO-PET substrates using a laser processing technique. A colloidal solution of commercial P25, water, acetylacetone, Triton X-100, and polyethylene glycol was utilized for this purpose. A $TiO_2$ layer was formed onto a borosilicate glass plate and then transferred to an ITO-PET substrate using the laser direct-write technique (LDW) [110][111]. Additionally, Huang et al. described a roll pressure rolling method paired with laser-assisted lift-off for the fabrication of $TiO_2$ photoelectrodes on ITO-PET substrates, resulting in an efficiency of 4.2% [49].

Ma et al. explored at another film-transfer method. By employing friction transfer of a sintered $TiO_2$ layer, they were able to create a $TiO_2$ coating on a flexible ITO-PET substrate. They applied a sintered $TiO_2$ sheet coated with a doctor blade and a low-temperature $TiO_2$ dispersion to the ITO-PET substrate. This sintered film was transferred across the ITO-PEN in direct contact with the $TiO_2$ layer underneath. Because of the friction created between the layers, the sintered layer was thus transferred from the ceramic tile to the bottom layer's surface [112]. While this technology has demonstrated some rather good efficiency, it is indisputable that converting this methodology into a continuous manufacturing process is quite difficult.

### 1.7.3. $TiO_2$ film compression

A technique for continuously creating a nanostructured film on FPCSs was patented in 2000 by Hagfeldt and associates. They proposed an FPCS roll that is set up to create a continuous web that moves in the direction of a pair of pressure rollers. A colloidal suspension is deposited, allowed to evaporate, and then squeezed by the rollers along its path. The film's compression aids in the breakup of big agglomerates, increasing the specific surface area and producing a highly light-scattering effect. The final product is a porous, nanostructured, mechanically stable coating with good adhetion to the substrate. They studied how the porous layer was affected by the compression of a planar steel press plate and demonstrate that the porosity of the film reduces with increasing applied pressure. The internal surface area, however, increased somewhat from 60.6 to 63.9 $m_2/g$. The compressed films displayed a more uniform pore size distribution in terms of BET pore size, with unpressed powder having pore sizes between 40 and 60 nm and pressed films having pore sizes between 30 and 40 nm. An important benefit of this automated method's introduction is that

it enables a high-speed, continuous roll-to-roll manufacturing process [54][113][114][96]. The same team created a detailed step-by-step base for the fabricating FDSSCs on ITO-PET and reported employing fluorescent light to achieve a maximum power output of roughly 2.3 $\mu W/cm^2$ at 250 lux, making it one of the first FDSSC modules for indoor conditions [53].

Numerous study teams have concentrated on refining this method following this discovery by maximizing experimental parameters such applied pressure [115]. Pressure changes cause the $TiO_2$ films' microstructure to change and the interparticle connection to improve, which raises photon-induced charge transfer and slowed down recombination kinetics ][116]. As a result, when the applied pressure increased, the electron transport resistance reduced. Faster electron transport and less back electron recombination are the outcomes of a more compact $TiO_2$ film structure, which improves the $J_{SC}$ [117][118][119].

Cheng et al. discussed the application of a cold isostatic pressure (CIP) technique in relation to the compression technique for the creation of superior $TiO_2$ flexible electrodes. Using P25 and ethanol, a 30 weight percent (wt%) titania solution was made, and it was coated onto ITO-PET using the doctor blade method. After being moved to a polyethylene envelope, the films were crushed using a CIP device and sealed under vacuum ($10^{-1}$ Torr). The films had a homogeneous free-crack surface architecture and a strong bond between the particles, both of which point to good interparticle connectivity [120].

### 1.7.4. Low-temperature deposition techniques

The low-temperature deposition methods that are most frequently employed are inkjet printing, screen printing, spin coating, spray coating, blade coating (also known as doctor blading), and slot-die. To produce homogenous, crack-free films, the printing parameters must be modified. Each process has pros and cons. since previously indicated, the primary problem with these techniques is the preparation binder-free colloids, pastes, or dispersion media without binder, since this has an immediate impact on the uniform and complete covering of the substrate, which is followed by the adhesion of the film to the substrate.

Due to a number of advantages that allow for uniform and controlled particle deposition, electrophoretic deposition (EPD) has drawn interest among low-temperature deposition techniques. EPD's main benefit is its low temperature capability, which makes it ideal for coating ITO-PEN substrates without causing damage. The method of EPD offers a great promise for handling low-temperature films [121][122][123]. Nevertheless, drawbacks render it less appropriate for the industrial manufacturing of thin films. Large-scale production demands efficiency and speed, which can be hampered by the low deposition technique used in EPD. Applying EPD to a sizable area can take some time and it might be technically challenging to achieve uniformity and consistency on a wide scale.

Various strategies have been explored to improve the adherence of $TiO_2$ nanoparticles to the substrate and the interconnection between them, in an effort to find ways that may be adapted to

these processes. The most pertinent post-treatments for low-temperature films are shown below [124][125][126][127][128].

### 1.7.5. UV irradiation post-treatment

The connectivity of $TiO_2$ particles has been further enhanced and film uniformity has been improved through the use of UV light. Precursors are frequently used in this post-treatment to prepare the colloidal solution, which, upon UV irradiation, enhances interparticle connection inside the film. Another effective technique for eliminating organic and inorganic residues from the $TiO_2$ film that come from the suspension during the production process is UV irradiation [129][130][131][132][133][134][135]. However, as exposure to UV might alter $TiO_2$ films' adhesion to the substrate and the dye sensitizer's adsorption, caution must be taken while employing this approach. SEM and FTIR spectroscopy are useful techniques to show whether or not the organic contaminants on the $TiO_2$ surface are removed without changing the film's morphology. Additionally, the films' dye loading may be improved by UV treatment [130].

Ayllón et al. investigated the production of low-temperature $TiO_2$ photoelectrodes for FPCSs using UV irradiation. They suggested a different technique for making thick sheets of porous $TiO_2$. By using a soluble precursor of $TiO_2$ that photodegrades, they were able to increase adhesion to the substrate and encourage the creation of necking between the particles. With the help of an ultrasonic bath, they combined commercial P25, titanium(IV) bis(ammonium lactate)dihydroxide (TALH), Triton-X, and water to create a colloidal solution. Small $TiO_2$ particles are formed as a result of the photodegradation of TALH, and these particles serve as cement for electrical

connections between larger particles. Following doctor blading of the film onto an ITO-PET substrate, the film was exposed to UV light for six hours at 80 °C using a medium-pressure mercury lamp. The organic nature of this precursor allows its removal after UV irradiation [132].

### 1.7.6. Microwave irradiation post-treatment

Microwave treatment is a method that has a lot of promise for producing solar cells utilizing FPCSs. By using this post-treatment, the local temperature inside the film may be significantly raised, which will speed up the sintering process without causing any harm to the FPCS. By encouraging the electrical connections between $TiO_2$ nanoparticles, this post-treatment improves photovoltaic output, current density, and efficiency [136][137][138][139].

### 1.7.7. Accelerated electron beam (EB) post-treatment

Accelerated electron beam (EB) post-treatment is another low-temperature (50 °C) method for FPCSs. This method achieves particle necking without causing damage to the FPCS by varying the accelerating voltage to regulate the electron's penetration depth into the $TiO_2$ layer. By grinding a blend of commercial $TiO_2$ P25, water, and ethyl alcohol, Yamaguchi et al. created a binder-free paste that was then doctor-bladed onto an ITO-PET substrate. After the film was subjected to the EB, the manufactured DSSCs achieved an efficiency of 2.1%. They demonstrate that $TiO_2$ particle necking was effectively accomplished at room temperature using this technique [140].

### 1.7.8. Combination of different strategies

Numerous research teams have demonstrated that combining various techniques will significantly increase the performance of FDSSCs. A combined press approach using a $TiO_2$-water-based paste and a UV-$O_3$ surface treatment both before and after paste deposition was reported by Yamaguchi et al. In the paste, they employed two distinct $TiO_2$ particle sizes with weight ratios of 7:3, 20 nm, and 100 nm, respectively. By using ISO/DIS 15814 to test the ad the substrate, they proved that the $TiO_2$ nanoparticles had a good mechanical adhesive strength to the substrate. Using this technique, a FDSSC achieved an efficiency of 8.1%; additionally, by applying an anti-reflecting layer to the DSSC's exterior, the RCPV, AIST, in Japan, confirmed a certified power conversion efficiency of 7.6% [141][142].

By examining the combined effects of electrophoretic deposition of colloidal commercial P25 and the mechanical compression method using non-polar volatile organic liquids to fill the pores of dry TiO2 films, Zaban et al. investigated a method to produce an improved $TiO_2$ nanoporous electrode on FPCSs [143]. The production of laser-sintered $TiO_2$ electrodes for FDSSC was documented by Huan Yang et al. ethanol was used with commercial P25 Degussa to create a paste without binder. The photoelectrode was made by compressing the film (200 MPa for 30 s) in a cold isostatic pressing machine after the paste was applied using a doctor blade technique on an ITO-PEN substrate. To promote a consistent local sintering (550 °C) of the film without causing damage to the FPCS, infrared laser sintering (1065 nm) was employed. This helped in the creation of necking between $TiO_2$ nanoparticles and the conversion of some of the nanomaterial's anatase phase into rutile phase. These tactics improved the effectiveness of charge collection, incident light

absorption, and efficiency from 4.6% to 5.7%, indicating a possible use of this technique for the roll-to-roll manufacturing of FDSSC [118].

Also, other groups have described the deposition of a blocking compact layer to hinder the recombination process [144][145]. In addition to suppressing interfacial charge recombination between injected electrons and dye cations, the low-temperature compact $TiO_X$ on the ITO surface or the $Al_2O_3$ electron recombination blocking layer on a $TiO_2$ film also improves the adhesion between ITO-PEN and the $TiO_2$ film [146][147].

One of the earliest studies on the co-sensitization impact of $TiO_2$ films to increase FDSSC efficiency was conducted by Miyasaka and colleagues. On an ITO-PEN substrate, they applied a commercial binder-free $TiO_2$ paste (PECC-K01), and then they heat-dried the material for 10 minutes at 150 °C. They employed various dyes (FL, N719, and black dye) to increase the range of absorption. Through adjusting the duration of immersion in the various dye baths, they managed to produce a co-sensitized FDSSC with a 5.10% efficiency [148].

Another interesting low-temperature method (<200 °C) was documented by Kunzmann and associates were the Ru(II)-based N3 dye was incorporated into the anatase $TiO_2$ network. The powders were dissolved in 100% ethanol (EtOH) for the pastes preparation. It was demonstrated that the integrated network layer promoted resistance to electron recombination with the electrolyte and improved device stability. In addition to a top integrated network layer, they used a bottom layer consisting of a P25:$TiO_{2\text{-}sp}$ mixture (80:20) to maximize the short-circuit current density and

collection yields. They reported multilayered photoelectrode devices with an efficiency of 8.75% that are stable up to 600 h under operation conditions [149].

An effective, flexible, organic dye-based DSSC was created by Kim and colleagues utilizing a redox electrolyte based on cobalt. On a flexible ITO-PEN substrate, they created a hierarchically structured $TiO_2$ film (HS-$TiO_2$) by employing a high molar extinction coefficient organic dye (JH-1) ($\varepsilon = 50{,}000\ M^{-1}cm^{-1}$).. A 10% (wt/v) commercial P25 powder in an ethanol solution was directly electro-sprayed onto the FPCS. After then, the film was compressed for ten minutes at 10 MPa. Through optimization of the HS-$TiO_2$ photoelectrode's thickness, they were able to achieve an efficiency of 6.12% using this arrangement [150][151].

Table 2. provides a summarized compilation of critical parameters utilized in pioneering work on the development of FDSSCs [43].

| **Substrate Type** | Applied T (°C)/Time (h) | Strategy Applied to the Low-T Films | Deposition Method | Active Layer Compositions | Thickness (μm) | Dye | Electrolyte | Counter Electrode | PCE (%) at 1 Sun | Ref. |
|---|---|---|---|---|---|---|---|---|---|---|
| **ITO-PET** | 100/12 | Laser direct-write technique | - | Colloidal $TiO_2$ paste of P25, Degussa), water, acetylacetone, Triton X-100, PEG | 12 | N3 | $I^-/I_3^-$-based | E-beam-evaporated-pt | 0.71 | [110] [111] |
| **FTO glass** | 100/24 | - | Spin coating | Synthesized colloidal $TiO_2$ solution | 1 | N3 | $I^-/I_3^-$-based | Pt-coated FTO glass | 1.22 | [22] |
| **ITO-PET** | Room T | Compression by rollers | Doctor blade | P25, ethanol | 8 | N719 | $I^-/I_3^-$-based | Porous carbon and porous platinized | 2.3 | [113] [152] [114] |
| **ITO-PET** | Room T | Compression | Doctor blade | P25, ethanol | 12 | Black and red dye | $I^-/I_3^-$-based | Platinized $SnO_2$ powder pressed on ITO-PET | 5.5 | [96] |
| **ITO-PET** | Room T | Compression (adjusting the pressure and thickness of the deposited layer) | Doctor blade | P25, ethanol or water | - | N719 | $I^-/I_3^-$-based | Platinized Sb-doped $SnO_2$ | 2–3 (6.1% at 0.1 sun) | [53] |
| **PET-ITO** | <80 | UV irradiation | Doctor blade | P25, TALH solution, Triton X-100, water | 12 | N3 | $I^-/I_3^-$-based | Pt-coated FTO glass | 2% | [132] |
| **PET-ITO** | 130/4 | UV irradiation | Doctor blade | commercial $TiO_2$ suspension (Solaronix) | - | N719 | Polymer electrolyte | Sputtered Pt on PET-ITO | 0.23 | [130] |
| **ITO-PET** | - | Compression using stainless-steel plates and using $Al_2O_3$ electron recombination blocking layer | Doctor blade | P25, dry ethanol | 8 | Ru-based | Polymer electrolyte | Sputtered Pt on ITO-PET | 2.5 (5.3% at 0.1 sun) | [147] |
| **ITO-PET** | 50 | Accelerating electron-beam (EB) shower | Doctor blade | $TiO_2$ paste of P25 in ethyl alcohol | 10 | N3 | $I^-/I_3^-$-based | Pt-coated FTO glass | 2.1 | [140] |
| **ITO-PET** | 80/20 | Chemical vapor deposition + UV irradiation + microwave irradiation | Electrophoretic deposition | Commercial $TiO_2$ (F-5), tert-butyl alcohol, acetonitrile | 10 | Ru-based | $I^-/I_3^-$-based | Pt-coated FTO glass | 3.8 | [137] [138] |
| **FTO glass** | 100/12 | Hydrothermal crystallization of $TiCl_4$ as a chemical glue | Doctor blading | Commercial P25, $TiCl_4$ | 10 | Ru-based | $I^-/I_3^-$-based | Pt-coated FTO glass | 6.23 | [98] |
| **ITO-PET** | - | Multi-mode microwave heating | Spray coating | Slurry of synthesized $TiO_2$ nanoparticles | 60 | Ru-based | $I^-/I_3^-$-based | Pt-coated FTO glass | 2.16 | [139] |
| **ITO-PET** | Room T | Laser-assisted lift-off combined with a roll-pressing process | Mechanical pressing and transferring | Sintered $TiO_2$ tape | 14 | N719 | - | Hydrolysis Pt counter electrode | 4.2 | [49] |
| **ITO-PET** | Room T | In situ hydrolysis using TTIP, UV ozone treatment | Doctor blade | P25, TTIP, ethanol | 8 | N3 | $I^-/I_3^-$-based | Platinized ITO-PET | 3.27 | [153] |
| **FTO** | 150/0.25 | Acid–base chemistry | Doctor blade | Synthesized $TiO_2$ particles, ammonia solution | 4.3 | N719 | $I^-/I_3^-$-based | Pt-coated FTO | 2.55 | [51] |
| **ITO-PEN** | <150 | Using binding agent (HCl) | Doctor blade or screen printing | Colloidal solution of $TiO_2$ with different particle sizes | 10 | N719 | $I^-/I_3^-$-based with different solvents | Pt-coated FTO glass | 5.8 (6.4% at 0.23 sun) | [104] |

| | | | | | | | | | | |
|---|---|---|---|---|---|---|---|---|---|---|
| **ITO-PEN** | 130 | Surface treatment of ITO using sputtered $TiO_x$ layer as a buffer layer followed by anodization | Doctor blade | Commercial binder-free paste (Peccell) | 12 | D149 | $I^-/I_3^-$-based | Pt-coated FTO glass | 3.7 | [144] |
| **ITO-PEN** | <150 | Sputtered $TiO_x$ layer as a buffer layer followed by anodization, and using co-adsorbent | Doctor blade | Synthesized $TiO_2$ nanoparticles with different sizes, tert-butanol, water | 10 | N719, SJW-E1 | $I^-/I_3^-$-based with different solvents | Pt-sputtered FTO glass | 6.31 | [145] |
| **ITO-PEN** | 150 | $TiO_x$ compact blocking layer | Doctor blade | Binder-free $TiO_2$ paste | 3.5 | D205 | $I^-/I_3^-$-based | Pt-sputtered FTO glass | 5.2 | [146] |
| **ITO-PET** | Air drying | Surface-modified $TiO_2$ nanoparticles | Doctor blade | Synthesized $TiO_2$ nanoparticles, methyl glycine, trimethoxy silane, toluene | 33 | N749 and N719 | $I^-/I_3^-$-based and Co-based | Platinum coated | 4.1 | [103] |
| **ITO-PET** | 120 | Condensation protonation–dehydration reaction using $H_2TiF_6$ as a binding agent to chemically sinter the $TiO_2$ particles | Doctor blade | P25, $H_2TiF_6$, water | - | N719 and SQ1 | $I^-/I_3^-$-based | Pt-coated | 4.2 | [102] |
| **ITO-PEN** | 120/0.25 | Cold isostatic pressing (CIP)+ laser sintering | Doctor blade | P25, ethanol followed by ball-milling | 13 | N719 | $I^-/I_3^-$-based | Pt-coated ITO-PEN | 5.7 | [118] |
| **ITO-PEN** | 150 | Combination of compression method and light confining effect of $TiO_2$–water paste | Doctor blade | Paste of $TiO_2$ nanoparticles with different sizes and ethanol | 4–8 | N719 | $I^-/I_3^-$-based | Pt-sputtered ITO-PEN | 7.4 | [120] |
| **ITO-PEN** | Room T | Compression method | Doctor blade | Paste of $TiO_2$ nanoparticles with two different sizes and ethanol | 6–10 | N719 | $I^-/I_3^-$-based | Pt-sputtered ITO-PEN or Ti foil | 7.6 | [142] |
| **ITO-PET** | 200 | Lift-off technique + compression method | Transfer process | $TiO_2$ nanosphere and nanorods | 8–10 | Ru-based | Polymer gel based on $I^-/I_3^-$ | Pt-evaporated ITO-PET | 5.8 | [110] |
| **ITO-PET** | 150 | Post-treatment with $TiO_2$ sol | Electrophoretic deposition | Commercial $TiO_2$ (F-5 and G-2), t-butyl alcohol, acetonitrile | 5–20 | N719 | $I^-/I_3^-$-based | FTO glass | 4.1 (4.3% at 0.23 sun) | [123] |
| **ITO-PEN** | 150/0.5 | Ball milling | Doctor blade or spin coating | P25, ethanol | 1–16 | N719 | $I^-/I_3^-$-based | Pt-coated ITO-PEN | 4.2 | [108] |
| **ITO-PEN** | 150/0.5 | Ball milling + chemically modification of slurry with HCl | Doctor blade | P25, ethanol | 8 | N719 | $I^-/I_3^-$-based | Pt-coated ITO-PEN | 5.0 | [100] |
| **ITO-PEN** | 150/0.5 | Ball milling + chemically modification of slurry with HCl and ammonia | Doctor blade | P25, ethanol | 10.3 | N719 | $I^-/I_3^-$-based | Pt-coated ITO-PEN | 4.9 | [101] |
| **ITO-PET** | Air drying | Cold isostatic pressure (CIP) | Doctor blade | Commercial P25 | 17.5 | N719 | $I^-/I_3^-$-based | Pt-coated ITO-PEN | 6.3 (7.4% at 0.15 sun) | [120] |
| **ITO-PEN** | 100/2 | UV irradiation and heat treatment | Spin coating | P25, acetylacetone, water, triton X-100 | 10–15 | N3, N719 | $I^-/I_3^-$-based liquid electrolyte and solid electrolyte based on polysaccharide | Pt-coated ITO-PEN | 2.63 | [133] |

| | | | | | | | | | | |
|---|---|---|---|---|---|---|---|---|---|---|
| **ITO-PEN** | 150 | Low-temperature chemical sintering of the graded film | doctor blade | P25 and $TiO_2$ (12, 28, and 100 nm) | 3–4 | K-N719 | $I^-/I_3^-$-based | Pt-coated FTO glass | 3.05 | [106] [154] |
| **ITO-PET** | 100/30 | Alkoxide hydrolysis of TIIP, resulting in an interconnection between the particles | Dip coating | Nanocrystalline colloid of titanium isopropoxide (TIIP) in an ethanolic dispersion of commercial P25 | 2 | Ru-based | Synthesized gel electrolyte based on $I^-/I_3^-$ | Platinized ITO-PET | 3.2 (3.4% at 0.125 sun) | [154] |
| **ITO-PET** | - | Direct UV irradiation of the oxide nanoparticles and using light scattering particles | Coating with a glass rod | Synthesized $TiO_2$, pentan-2,4-dione, Triton X-100, water | 1.1 and 2.3 | N3 | $I^-/I_3^-$-based | Pt-coated FTO glass | 2.5 | [135] |
| **ITO-PEN** | 125/1 | Friction-transfer technique + compression method | Spray coating | Paste of P25, TBT, ethanol | 28 | N719 | $I^-/I_3^-$-based | Pt-coated ITO-PEN | 5.7 | [112] |
| **ITO-PEN** | 150 | Using smaller particles for interconnection between bigger particles | Doctor blade | Paste of $TiO_2$ nanoparticles (9, 23, and 60 nm) | 5–6 | KN-719 | $I^-/I_3^-$-based | Platinized ITO glass | 3.93 | [116] |
| **ITO-PEN** | Air drying | Compression method | Doctor blade | Paste $TiO_2$ nanoparticles with different sizes | 6–12 | N719 | $I^-/I_3^-$-based | Pt-coated ITO-PEN | 4.21 | [117] |
| **ITO-PEN** | 150/0.16 | - | Doctor blade | commercial binder-free $TiO_2$ paste (Peccell) | 10 | co-sensitization FL and N719, FL and black dye | $I^-/I_3^-$-based | Pt-sputtered FTO glass | 5.10 | [148] |
| **ITO-PEN** | 140/0.5 | Compression | Doctor blade | binder-free colloidal suspension of commercial P25 | - | N719 | $I^-/I_3^-$-based | Pt-coated ITO-PEN | 4.39 | [115] |
| **ITO-PEN** | Room T | Resonant multiple light scattering effect | Electrospray coating | Hierarchically structured $TiO_2$ and P25 | 3–12 | JH-1 | Co-based | Pt-Ti-sputtered ITO-PEN | 6.12 | [151] |
| **ITO-PEN** | 120 | Using binding agent $H_2TiF_6$ to interconnect the particles | Doctor blade | Homemade $TiO_2$ anatase: rutile (80:20, w:w), $H_2TiF_6$, water, TIIP. | 1.17 | Y123 | $I^-/I_3^-$ based | PEDOT-coated ITO-PEN | 1.27 | This work |

# OBJECTIVES

## 2. Problem statement

The photoanode is essential to dye-sensitized solar cells because it carries out vital tasks such as effective dye molecule adsorption, electron injection and transport procedures. To enhance the solar cell's ability to harvest light, a high density of dye sensitizers must be anchored, which requires a large surface area. In addition, the photoanode transports photogenerated electrons, which necessitates effective charge separation and low recombination losses. Thus, to achieve high-performance DSSCs, the design and optimization of the photoanode structure and materials are crucial [46].

The substrates for DSSCs that are most frequently utilized are glass, plastic, and metal. However, using glass substrates can not be used in order to meet the requirements for large-scale production. Alternatively, there are viable alternatives available in three basic DSSC configurations: plastic and metal substrates [97]. Although metal substrates have demonstrated encouraging efficiency, they still have some disadvantages, such as the potential for electrolyte solution components to cause corrosion.. Hence, careful consideration should be taken in the selection of electrolyte components to ensure compatibility with the chosen substrate type. Additionally, the high-temperature sintering process employed with metal substrates can give rise to oxidation concerns, needing additional steps that complicate large-scale manufacturing processes [155].

One significant disadvantage of using metal substrates in DSSCs is that they are opaque. Such DSSCs must be illuminated from the front side via the counter electrode, which lower the conversion efficiency. This can be explained by partial light reflection caused by different molecular species in the redox electrolyte solution or by the electrocatalyst placed on the counter electrode [46]. Interestingly, plastic substrates like indium-doped tin oxide polyethylene naphthalate (ITO-PEN) and indium-doped tin oxide polyethylene terephthalate (ITO, $In_2O_3$:Sn) (ITO-PET) have several benefits, like being lightweight and flexible, which makes them ideal for reel-to-reel (R2R) production methodsIn addition, these substrates function better than their metal equivalents, displaying acceptable levels of transparency (80% at 550 nm), a sheet resistance of roughly 10 Ω/sq, and excellent chemical stability inside the electrolyte. In addition, these substrates function better than their metal equivalents, displaying acceptable levels of transparency (80% at 550 nm), a sheet resistance of roughly 10 Ω/sq, and excellent chemical stability inside the electrolyte. [156][157].

The conventional $TiO_2$ paste composition consists of viscous solvents and organic binders, which necessitate a high-temperature sintering procedure (usually 400–500°C) to create efficient electrical connectivity between particles. However, because plastic substrates have a low thermal stability, using them makes the high-temperature procedure difficult. It is imperative to fabricate the titania layer of DSSCs at low temperatures on flexible plastic substrates because low substrate thermal stability (about 150 °C) poses a major challenge. Novel approaches and methods have been acrried out to overcome these obstacles and permit the deposition of $TiO_2$ layers at temperatures that are within the permissible range for conducting polymers [97]. This has therefore encouraged researchers to investigate a range

of approaches, mostly centered on enhancing the characteristics of the $TiO_2$ paste and using different pre- and post-treatment strategies, in order to produce flexible devices with high efficiency [115][158][159].

A few particular conditions must be met in order to prepare a screen-printable $TiO_2$ nanocrystalline paste without the need for the sintering procedure. First, in the event that the commonly employed insulating binder components are not present, the paste must have a high enough viscosity. Electron charge transport between $TiO_2$ particles may be hindered by binders in dry film [160]. Second, it is crucial that the paste adheres firmly to the ITO-coated PEN's hydrophobic surface. Moreover, it is essential that all of the paste's liquid ingredients evaporate completely at temperatures lower than 150 °C [149].

In order to prevent any potential corrosion of the underlying ITO layer, all components of the paste should also display inert qualities. This can be achieved, for example, by preventing the inclusion of acidic precursors, which could also undermine interparticle connections [104]. One more important factor that needs to be carefully considered is the usage of ultrathin films (~ 6 μm). Four reasons are served by these thin films on flexible substrates: (i) to reduce the distances over which electrons diffuse; (ii) to improve mass transport by decreasing the distance over which ions diffuse; (iii) to improve the adhesive properties between the paste and the substrate because thicker films are more likely to delamination; and (iv) to reduce the occurrence of macroscopic cracks [120]. One of the most desirable options in this regard is the creation of a paste without the use of organic surfactants. The creation of a low-temperature screen-printable $TiO_2$ paste is a substantial difficulty for

FDSSC manufacturing. To successfully get over this important issue and overcome the challenge, creative solutions are needed for industrial outputs.

## 2.1. General objetive

To evaluate three $TiO_2$ crystalline phases to prepare a binder-free aqueous $TiO_2$ paste with enhanced interparticle conexion, improved transparency and strong adhesion to ITO-coated PEN substrates for FDSSCs and high-temperature pastes for high-performance DSSCs.

## 2.2 Specific Objectives

To synthesize different $TiO_2$ crystalline phases (anatase, rutile and brookite) for their evaluation on flexible and rigid DSSC.

To apply two different powder cleaning traetments to remove organic compounds and increase hydroxyl groups from the $TiO_2$ surface to improve dye loading.

To incorporate of $TiO_2$ anatase and rutile in the binder-free aqueous paste formulation to improve electron transport and improve interparticle connection.

To incorporate of a $H_2TiF_6$ and Titanium isopropoxide as $TiO_2$ binding agents in the binder-free aqueous paste to improve interparticle connection, produce an homogeneous transparent film and obtain a strong adhesion between the films and the plastic substrates.

To explore two different $TiO_2$ particles dispersion methods to obtain a stable coloid for the preparation of binder-free aqueous pastes for FDSSC and high-temperature proccessed pastes for high-performance DSSC.

To find an optimal electrolyte formulation using $I^-/I_3^-$ as the redox couple for a low-temperature DSSC.

To evaluate the performance of a high molar extinction coefficiente dye (Y123) to maximize the light absorption and improve the efficciency of a low-temperature DSSC.

To compare the performance of $I^-/I_3^-$ and the Cu-based redox pair in low-temperature DSSCs using a binder-free $TiO_2$ paste, Y123 dye and PEDOT counter electrode.

To characterize the photovoltaic performance of the fabricated devices under simulated outdoor and indoor conditions.

To characterize the internal kinetics for the optimal low-temperature configuration by electrochemical impedance spectroscopy.

## DEVELOPMENT

### 3. Theoretical background

Photovoltaic (PV) technology is one of the most promising RE technologies. Popular configurations for photovoltaic systems include stand-alone, grid-connected, and hybrid setups growing quickly around the world. PV technology is the most direct method of converting solar energy into electrical power working by using the photovoltaic phenomenon, which was discovered in 1839 and was originally noticed by Henri Becquerel, generally defined as the emergence of an electric voltage between two electrodes attached to a solid or liquid system upon shining light onto this system .

### 3.1. Photovoltaic parameters

At a certain photocurrent, an illuminated solar cell can produce a specific photovoltaic. A solar cell's operating point is a set of photovoltaic and photocurrent values at which it can function. Starting from Ohm's law:

$$R = \frac{V}{I} \tag{6}$$

In a simplistic approach, at very low R, the photovoltage is very low and at very high R, the photocurrent is very low. A solar cell is said to be operating in both short- and open-circuit conditions when its R value is either infinitely high or equal to zero. Short-circuit current ($I_{SC}$) and open-circuit voltage ($V_{OC}$) are the terms used to describe the photovoltaic and

photocurrent values under short- and open-circuit situations, respectively. When a solar cell operates both in short- and open-circuit, its electric power is equal to zero.

A solar cell's current-voltage characteristic, or I–V characteristic, is a plot of all potential operating points within a range. The schematic representation of a solar cell's I–V characteristics under illumination is shown in Figure 6. The solar cell's maximum power can be achieved at a single voltage and current combination ($V_{mp}$ and $I_{mp}$, respectively). The maximum power point (mpp) is the location on the I–V characteristic of an illuminated solar cell:

$$P_{mpp} = I_{mp} \cdot V_{mp} \tag{7}$$

Measuring the $I_{SC}$ and $V_{OC}$ values is simple. Thus, rather than characterizing the solar cell with Imp and Vmp, it is more convenient to characterize the maximum power of a solar cell using $I_{SC}$ and $V_{OC}$. The additional parameter establishes the relationship between the product of $I_{SC}$ and $V_{OC}$ and the product of $I_{mp}$ and $V_{mp}$. This parameter, also known as the fill factor (FF), indicates the degree to which the $I_{mp}$-$V_{mp}$ rectangle fills the $I_{SC}$-$V_{OC}$ rectangle.

$$FF = \frac{I_{mp} \cdot V_{mp}}{I_{SC} \cdot V_{OC}} \tag{8}$$

When considering the solar cell active area, short circuit current density $J_{SC}$ (mA / $cm^2$) can be used as a measure of a solar cell's efficiency (η), which is defined as the ratio between the

power extracted at the solar cell's mpp and the power of the sunlight at which the solar cell is illuminated ($P_{sun}$):

$$\eta = FF \cdot J_{SC} \cdot V_{OC} \quad (9)$$

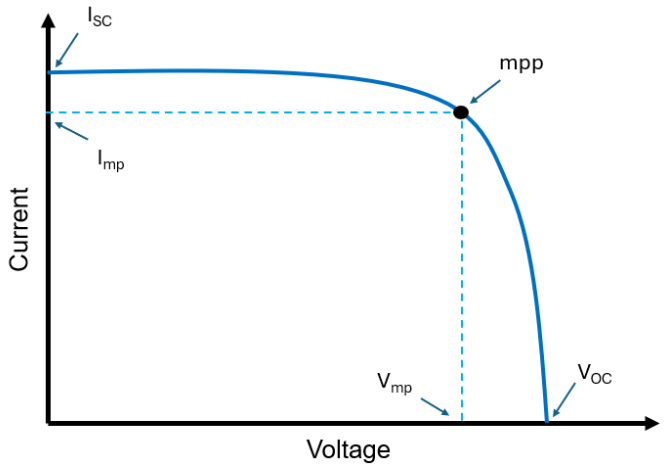


Figure 6. Example of a current–voltage characteristic (a) and of the corresponding power–voltage characteristic (b) of a solar cell under illumination. The short-circuit current density, the open-circuit voltage, the maximum power point and the voltage and current density at the maximum power point are denoted by $I_{SC}$, $V_{OC}$, mpp, $V_{mp}$ and $I_{mp}$, respectively.

### 3.1.1 Diode equation

The equivalent circuit of the ideal solar cell (Figure *7*) consists of two distinct parts that represent the two fundamental functions of a solar cell. The photocurrent generator, or current source powered by light, is the first component. In order for the current to flow through the second element in one direction but not the other, it must satisfy the requirement of charge separation.

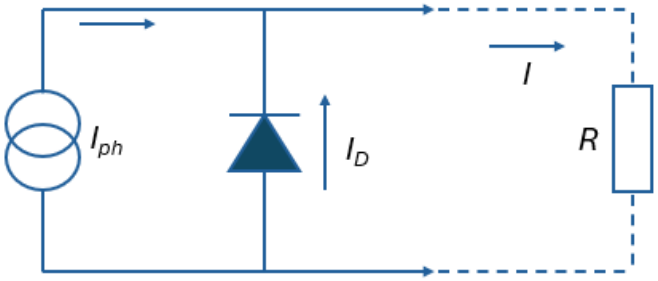


Figure 7. Equivalent circuit of an ideal solar cell containing a photocurrent generator and a diode for charge separation and connected to a R.

This is the characteristic property of a diode, the second element in the equivalent circuit of an ideal solar cell. A current across a diode ($I_D$) is described by the diode equation.

$$I_D = I_0 \cdot \left[ exp \cdot \left( \frac{q \cdot V}{k_B \cdot T} \right) - 1 \right] \quad (10)$$

The proportionality factor, often known as the diode saturation current or diode saturation current density ($I_0$), is contained in the diode equation. Each solar cell has a unique diode saturation current that is influenced by the geometry, materials of the contact and absorber. While the voltage is multiplied by $q$ and divided by the product of $k_B$ and T, the diode saturation current is multiplied by an exponential of the voltage. With a rise in positive voltage, the diode current grows exponentially (forward direction or forward bias). The diode current should to be zero at zero voltage. This is the reason why the diode equation's exponential term needs to have 1 subtracted from it. The diode current drops to the extremely

low negative $I_0$ (reverse bias or reverse direction) at negative voltage. A diode equation can be used to characterize any charge-selective contact. A perfect diode has a very high resistance in the reverse direction and a very low resistance in the forward direction. The photocurrent is not shifted by the diode; rather, it passes through the R. As a result, the photocurrent must be substracted from the diode current since it is a reverse current. The ideal solar cell's diode equation is the result of this:

$$I = I_0 \cdot \left[ exp \cdot \left( \frac{q \cdot V}{k_B \cdot T} \right) - 1 \right] - I_{ph} \qquad (11)$$

By setting $I_{ph}$ equal to $I_{SC}$, equation 11 can be utilized to analyze the I-V characteristics of illuminated solar cells. At AM1.5G, the $I_{SC}$ typically has values in the tens of $mA/cm^2$. For ease of use, the I–V properties of solar cells under light are frequently shown in the first quadrant. The negative current is shown in the solar cell's I–V characteristic for this purpose. $I_{SC}$ and the negative $I_{ph}$ are conventionally correlated. However, for n-type materials (as most DSSCs), photocurrent is generally defined as positive.

### 3.1.2. Open circuit voltage

By setting the current to zero, equation 11, one can determine the $V_{OC}$ of a perfect solar cell. Depending on the components and the interfaces connecting the materials that comprise the diode, the value of $I_0$ can vary by several orders of magnitude. The fact that $I_0$ limits $V_{OC}$ indicates how crucial $I_0$ is to a solar cell's function. In order to maximize the performance of

solar cells in general, $I_0$ must be minimized. As $I_{SC}$ increases, so does the value of $V_{OC}$. Figure 8 illustrates the dependence of $V_{OC}$ on $I_{SC}$ for three distinct values of $I_0$.

$$V_{OC} = \frac{K_B \cdot T}{q} \cdot \left(\frac{I_{SC}}{I_0} + 1\right) \approx \frac{K_B \cdot T}{q} \cdot ln\left(\frac{I_{SC}}{I_0}\right) \tag{12}$$

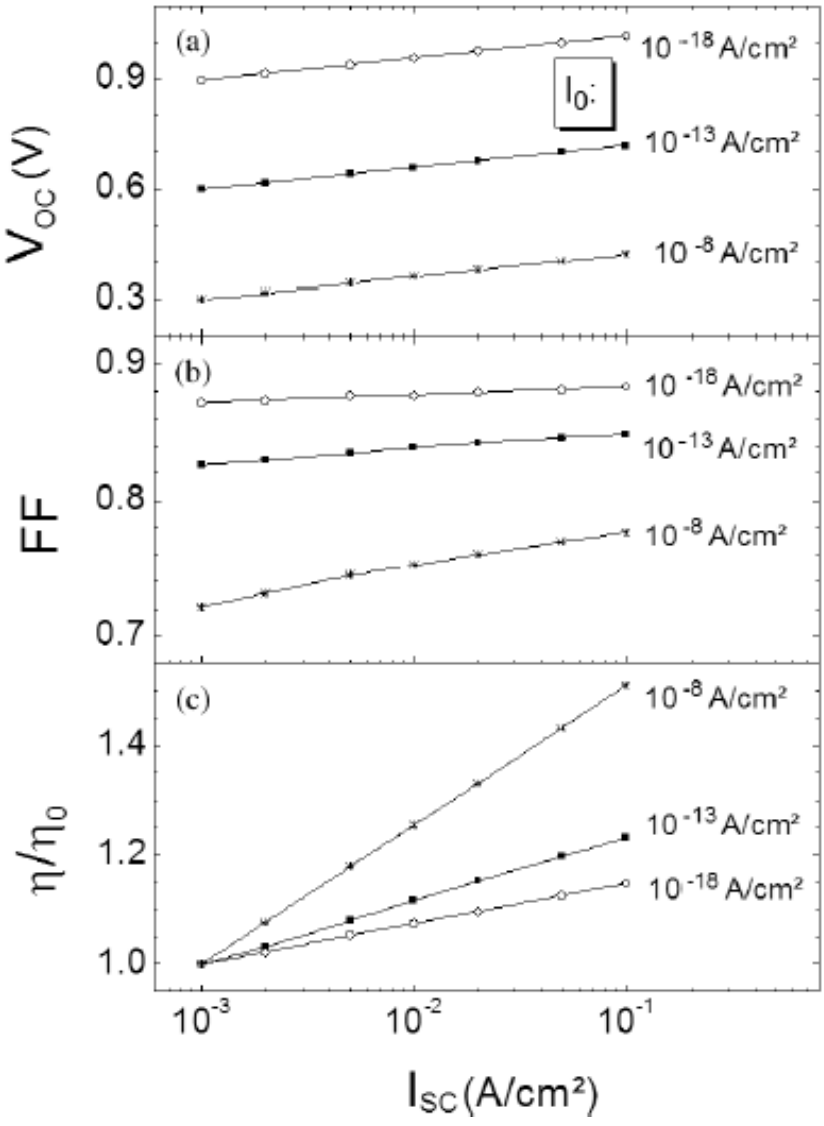


Figure 8. Dependence of $V_{OC}$ (a), FF (b) and the normalized η (c) on $I_{SC}$ for an ideal solar cell with $I_0 = 10^{-18}$, $10^{-13}$ and $10^{-8}$ A/cm$^2$ . Taken from [13].

### 3.1.3. Fill Factor

Equation 8 can be simulated to get $I_{mp}$ and $V_{mp}$, which will allow to calculate the FF. For instance, Figure 8 (b) shows the FF plotted as a function of $I_{SC}$ for $I_0 = 10^{-18}$, $10^{-13}$, and $10^{-9}$ A/cm$^2$. The FF is higher for the lower $I_0$ at fixed $I_{SC}$. At fixed $I_0$, the FF rises as $I_{SC}$ grows. For low values of $I_0$, the FF rise with rising $I_{SC}$ is weak. For instance, the FF varies about between 0.87 and 0.88 for $I_{SC}$ between 1 and 100 mA/cm$^2$ at $I_0 = 10^{-18}$ A/cm$^2$. Conversely, with smaller values of $I_0$, the increase in FF with increasing ISC is stronger. For instance, the FF varies approximately between 0.72 and 0.78 for $I_{SC}$ between 1 and 100 mA/cm$^2$ at $I_0 = 10^{-8}$ A/cm$^2$.

### 3.1.4. Solar cell efficiency

Since FF, $I_{SC}$, and $V_{OC}$ all dependent on light intensity, the solar energy conversion efficiency is dependent on the sun power $P_{sun}$. The following takes into account the ratio of two solar energy conversion efficiencies ($\eta/\eta_0$), where the index 0 is connected to the lower value of $P_{sun}$:

$$\frac{\eta}{\eta_0} = \frac{FF}{FF_0} \cdot \frac{I_{SC}}{I_{SC,0}} \cdot \frac{V_{OC}}{V_{OC,0}} \cdot \frac{P_{sun,0}}{P_{sun}} \tag{13}$$

If we assume that $I_{SC}$ increases linearly with increasing light intensity, that is, that $I_{SC}$ is proportional to $P_{sun}$, then equation 13 can be simplified. Thus, with relation to equation 12, one obtains:

$$\frac{\eta}{\eta_0} = \frac{FF}{FF_0} \cdot \frac{T}{T_0} \cdot \frac{V_{OC}}{V_{OC,0}} \cdot \frac{ln\frac{I_{SC}}{I_0}}{ln\frac{I_{SC,0}}{I_{0,0}}} \tag{14}$$

If heating produced by increased $P_{sun}$ is neglected and a constant $I_0$ is taken for granted, equation 14 can be made even simpler. One must take care while making these two assumptions because $I_0$ can rely on $P_{sun}$ and T of solar cells normally increases with increasing $P_{sun}$. Following a transformation, the equation that follows is produced:

$$\frac{\eta}{\eta_0} = \frac{FF}{FF_0} \cdot \left[1 + \frac{X}{ln\frac{I_{SC,0}}{I_{0,0}}}\right] \tag{15}$$

$$X = \frac{P_{sun}}{P_{sun,0}} \tag{16}$$

The concentration factor is denoted by X. As found in section 3.1.3. Fill Factor, the ratio of the FFs is greater than 1, and X, as well as the natural logarithm of the ratio of $I_{SC,0}$, and $I_0$, are positive. Consequently, a perfect solar cell's η increases with increasing light intensity. This explains why focused sunlight produces the highest possible solar energy conversion efficiencies.

### 3.1.5. Series and parallel resistance

Ohmic resistances cause losses in every solar cell. For instance, in a solar cell, parallel resistances are caused by defects such as local shunts, while series resistances are caused by contact resistances or material resistances. The analogous circuit of a real solar cell consists of one common series resistance ($R_s$) and one common parallel resistance ($R_p$), also known as shunt resistance (Figure 9).

There is an equal current that flows through both the $R_S$ and the R. Hence, the voltage drop across the $R_S$ decreases the potential across the R. Additionally, the current passing through the $R_p$ lowers the current flowing through the R. The following diode equation considers the voltage drop across Rs and the current shunted by $R_p$, with the assumption that the voltage drop across $R_S$ is much less than $V_{mp}$:

$$-1 = I_0 \cdot \left[exp\left(\frac{q \cdot (V - I - R_s)}{k_B \cdot T}\right) - 1\right] + \frac{V - I - R_s}{R_p} - I_{SC} \qquad (17)$$

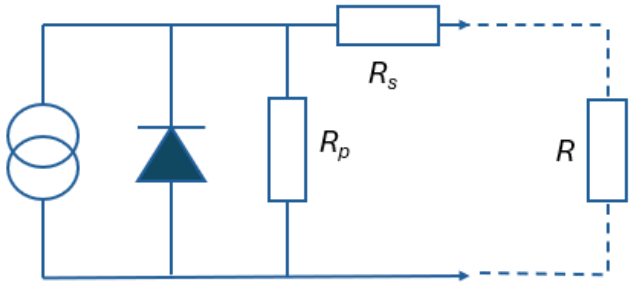


Figure 9. Equivalent circuit of a real solar cell containing a photocurrent generator, a deal diode, a shunt resistance ($R_p$) and a series resistance ($R_s$) and connected with a load resistance (R).

The $R_s$ and $R_p$ have a significant impact on a solar cell's I–V properties. In the following, the effects of $R_S$ and $R_p$ on I-V characteristics will be examined independently for a solar cell with fixed $I_0$ ($10^{-13}$ A/cm$^2$) and fixed $I_{SC}$ (0.04 A/cm$^2$). In these circumstances, $V_{OC}$ approaches 0.7 V and R is around 17 Ω cm$^2$ in the case of the ideal solar cell. It should be noted that, depending on $R_S$, the $I_{SC}$ in equation 17 and the short-circuit current produced at zero potential ($I^*_{SC}$ in (Figure 10, (a)) might differ significantly.

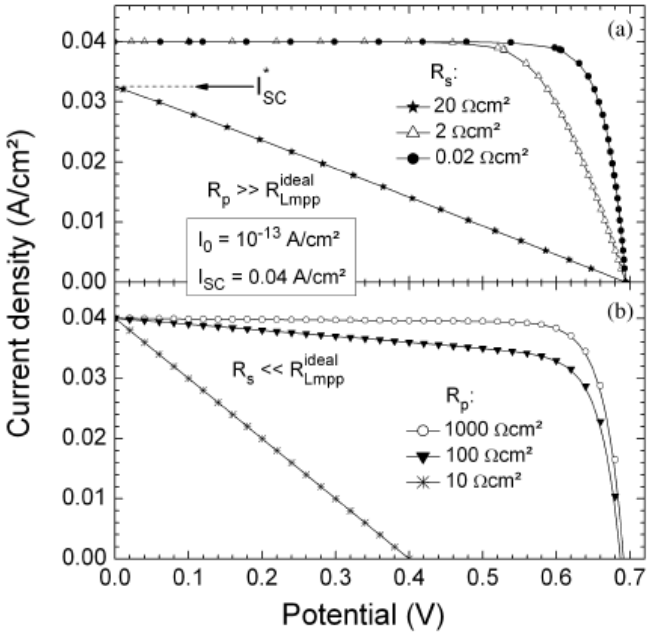


Figure 10. I–V characteristics for a solar cell with negligible $R_p$ (a) or $R_s$ (b) for different values of $R_s$ (a) and $R_p$ (b) and $I_0 = 1_0{}^{-13}$ A/cm$^2$ and $I_{SC}$ = 0.04 A/cm$^2$ [13].

The I-V characteristics for solar cells where $R_s$ are roughly three or one orders of magnitude lower than the ideal solar cell or extremely close to it, and for which $R_p$ can be omitted, are displayed in Figure 10 (a). For the I–V characteristics with $R_s$ = 0.02 cm$^2$ and $R_s$ = 2 cm$^2$, the values of $I_{SC}$ and $V_{OC}$ are nearly same, whereas FF dramatically falls for the I–V characteristic

with $R_s = 2\ cm^2$. Even with additional increases in $R_s$, the value of $V_{OC}$ stays unchanged since $R_s$ has no effect while there is no current flowing. However, $I^*_{SC}$ falls to less than $I_{SC}$, at around $0.032\ A/cm^2$, and at $R_s = 20\ cm^2$, the I–V characteristic becomes a straight line.

For a linear I–V characteristic, the FF is 0.25. The lowest possible FF of a solar cell is 0.25, which can be represented by an equivalent circuit as seen in Figure 9. High Rs limit values for FF and $I_{SC}$. The I–V characteristics for solar cells with Rp that are around two or one orders of magnitude greater than ideal solar cell or very close to it, and for which Rs can be omitted, are displayed in Figure 10 (b). Since the shunt resistance can be disregarded under the $I_{SC}$ condition, which corresponds to an endlessly low R, the values of $I_{SC}$ are the same for any $R_p$. The solar cell with $R_p = 100\ cm^2$ has a somewhat lower $V_{OC}$ value than 0.4 V for the solar cell with $R_p = 10\ cm^2$. When $R_p = 10\ cm^2$, or FF = 0.25, the I–V characteristic becomes a straight line and low $R_p$ limit the values for FF and $V_{OC}$.

### 3.1.6. Measurements of I-V characteristics

To determine the FF and, thus, the η, the full I–V properties of illuminated solar cells must be measured. Additionally, the entire I–V characteristics can be used to determine the $R_s$ and $R_p$. Variable resistance is required to probe various working points since the current to voltage ratio varies at each point along the I–V characteristic The measurement of η is commonly performed using a solar simulator. The standard test conditions (STC; AM1.5G with 1000 $W/m^2$ and T of the solar cell at 25 °C) are the common standard for the characterization of the η of solar cells. A solar simulator is an artificial light source with an intensity spectrum

very close to that of the sun at AM1.5. At AM1.5, the sun spectrum must be artificially recreated using the right light sources, light source combinations, and light filters. For instance, a blackbody with a T of 5800 K can be used to imitate the sun spectrum at AM0. There are no related blackbodies on earth, however, a light source with a T in the arc of roughly 10,000 K is a xenon arc lamp. A xenon arc lamp's maximum intensity is reached at a wavelength of roughly 300 nm. In addition, a xenon arc lamp has a large number of intense spectral lines, particularly in the near infrared spectrum. The solar simulator has extra filters to remove the strong infrared lines from the xenon arc lamp and to collect light in the AM1.5G spectrum's lower intensity areas. The solar cell is connected to a source measurement device and maintained at 25°C in a tempered holder [13][161][162].

### 3.2. DSSC operation mechanism

An examination of the particular functions performed by each of the elements in the DSSC and the operating mechanism is presented in the section that follows.

Figure 11 illustrates the technique by which dye-sensitized solar cells convert solar radiation into electrical energy. This process is similar to the photoinduced electron transfer process that takes place during photosynthesis in plants. A unique and distinguishing aspect of DSSCs is the mechanism, which seeks to resemble various natural processes. The dye has a function analogous to that of chlorophyll in plants. When incoming photons are absorbed by the sensitizer, which form a monolayer adsorbed on the surface of the mesoporous metal oxide, the energy conversion process is initiated. The energy of the photon is enough to

trigger an electronic excitation in the sensitizer. Process 1 involves the promotion of electrons from their ground state into an excited state. The transition from the highest occupied molecular orbital (HOMO) to the lowest unoccupied molecular orbital (LUMO) is how this is simplified in the literature. The excited state electrons may have a higher energy upon stimulation and can travel to the metal oxide photoanode's conduction band (process 2). At the dye-metal oxide interface, charge separation happens at a time interval of femtoseconds to picoseconds. The transparent conducting oxide coating covering the glass substrate is reached by the injected electrons after diffusing through the nanostructured, mesoporous metal oxide film (process 3). The timescale for this process is between nanoseconds to microseconds. At the same time, in the nano-to microsecond time frame, electron donation from a reduced species in the electrolyte returns the oxidized sensitizer molecules to their ground state; this process is known as "hole" transfer to the electrolyte (process 4). When electrons from the counter electrode pass through the external circuit and catalyze the redox couple's reverse reaction, the circuit is closed and the oxidized redox mediator eventually diffuses to the counter electrode (process 5). As a result, the solar cell is entirely regenerative, with the injected and collected electrons moving through the external wiring to perform work.

### 3.3. Recombination procceses

To maximize a DSSC's performance, electronic recombination processes must be prevented. Non-desired recombination of electrons with holes is known as "electrical recombination" and it can seriously affect a device's efficiency. Recombination occurs through a number of routes, and optimizing these pathways is crucial to improving the overall efficiency of DSSCs. One route involves the excited state electrons' non-radiative relaxing at the sensitizer's LUMO energy level, which leads to their return to the ground state (process 6). An increased degree of dye molecule aggregation at the metal oxide surface is frequently associated with this phenomena. During this phase, the dye's LUMO electrons may also recombine with the redox electrolyte in a matter of milliseconds to seconds (process 7).

Moreover, electrons have to travel a significant distance (2 to 10 micrometers) after being injected into the conduction band in order to reach the photoanode's TCO. Electrons encounter obstacles on their journey due to insufficient interparticle connections and/or electronic trap states brought on by surface-level defects in the crystal lattice of the metal oxide. If an electron stays in the conduction band for too long, there is a greater chance that it will deviate from its intended path. This could result in electrons being transported to the redox electrolyte surrounding the metal oxide or back-transferred to oxidized dye molecules (process 8 and 9). Finally, even after reaching the anode, electrons still have to cross the TCO surface in order to reach the external circuit. The reduction of oxidized species in the redox electrolyte can cause the TCO to be lost if it comes into touch with it (step 10). A number of

design techniques have been devised for the photoanode, dye molecules, and redox mediators to stop this kind of electron recombinations [43].

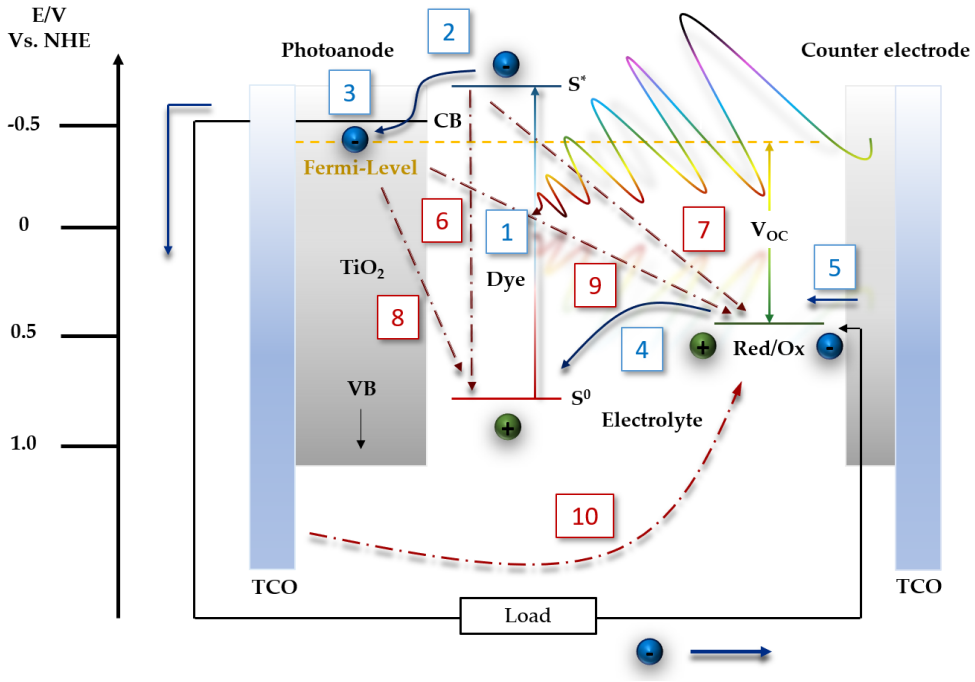


Figure 11. Figure shows the charge flow pathways within a DSSC in an energy diagram. The favorable operating flow is indicated by blue numbers and arrows, while the red numbers and arrows represent various electronic recombination pathways. Blue and green spheres represent electrons and "holes", respectively [43].

### 3.4. DSSC photovoltaic parameters

One can measure a DSSC's overall performance under irradiation by measuring its efficiency of converting sunlight into electric power under typical irradiation circumstances (100 $mW/cm^2$, AM 1.5G).

The potential difference between the electrolyte's redox potential and the metal oxide's electrons' Fermi level determines the voltage at which J equals zero is known as the $V_{OC}$. A number of variables, including incident light harvest efficiency, charge injection efficiency, and charge collecting efficiency, affect $J_{SC}$, which is a crucial parameter.This is the maximum current density that is generated when the cell is under short circuit zero bias conditions. One important performance factor that has a big impact on a solar cell's efficiency is its FF. Its simplified definition is the maximum power output divided by the product of $J_{SC}$ and $V_{OC}$. The point on the J–V curve where the voltage and current density are denoted by the symbols $V_{max}$ and $J_{max}$, respectively, is where the greatest power output occurs. [4][23].

### 3.5. Rheology

The study of soft, complex matter's flow and deformation is known as rheology. Its objectives are to comprehend, simulate, and predict the behavior of these kinds of systems. The experimental, metrological equivalent of rheology is called rheometry and easuring the material functions analyzed by rheology is its primary goal . This is achieved by subjecting materials to precise stress or deformation in rheometers, specialized equipment. Shear is commonly used to measure flow, and torque and flow rate measurements are used to derive the shear parameters of stress (τ) and strain rate ($\hat{\gamma}$) and the formula for viscosity (η) is:

$$\eta = \frac{\tau}{\hat{\gamma}} \tag{18}$$

This is more accurately referred to as apparent viscosity. Different definitions of viscosity exist, such as differential viscosity, which is the slope of the curve relating stress and strain rate, and plastic viscosity, which is the slope of stress versus strain rate for a plastic material, as will be covered below. As such, it is crucial to specify the precise type of viscosity when reporting results. Newtonian behavior is the most basic type, where stress and strain rate have a linear connection and there is no stress at zero strain rate. Many fluids exhibit plastic behavior, also known as Bingham behavior, in which flow only begins beyond a certain stress level (referred to as the yield stress) and the connection between stress and strain rate is linear once flow has begun. Pseudoclastic thinning, also known as shear thinning, is another typical phenomenon where viscosity reduces with increasing strain rate. While thickening behavior is occasionally observed in materials, it is uncommon in suspensions [163].

Rheological behavior of solid-particle suspensions in liquids is typically useful since the suspensions operate like a fluid in most situations. The volume proportion of solid particles in the suspension and the degree of particle agglomeration or flocculation are two important factors influencing this behavior. Viscosity increases significantly as the volume fraction of solids ($\phi$) increases. Einstein identified the relationship between viscosity and solids volume fraction and proposed it as follows:

$$\eta = \eta_c(1 - 2.5\phi) \tag{19}$$

where $\eta_c$ is the fluid phase's viscosity and $\eta$ represents the suspension's viscosity. It was eventually discovered, nevertheless, that this equation is only applicable at rather low volume

fractions. The viscosity gradually increases from what equation 19 predicts as the volume fraction is raised above a few percent. A number of equations have been devised to better characterize the relationship between viscosity and volume fraction; Krieger and Dougherty's equation is one that is often utilized in colloidal suspensions:

$$\eta = \eta_c \left(1 - \frac{\phi}{\phi_m}\right)^{-[\eta]\phi_m} \tag{20}$$

where $\phi_m$ is the highest volume fraction that can be achieved for the specific particle assembly. The highest volume fraction for spheres packed closely at random is 65%. Intrinsic viscosity, or [η], is the other parameter and is defined as:

$$[\eta] = \lim_{\phi \to 0} \frac{\frac{\eta}{\eta_c} - 1}{\phi} \tag{21}$$

For spherical particles, the intrinsic viscosity is 2.5, while for nonequant forms, it is greater. The considerable increase in viscosity observed as $\phi \rightarrow \phi_m$ is appropriately predicted by equation 20.

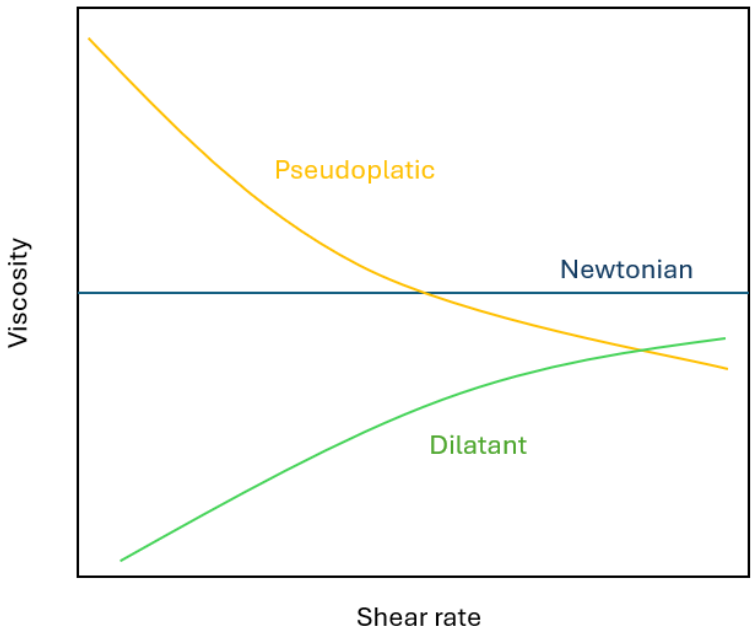


Figure 12. Typical plot of the behaviour of viscosity of different fluids with shear rate. Newtonian fluids (blue), pseudoplastic (yellow) and dilatant (green). Adapted from [163].

The degree of particle dispersion or flocculation is the other factor influencing flow behavior. Since colloidal particles, or those with a diameter of less than one micrometer, have the ability to flocculate on their own, floceulation is particularly crucial. As illustrated in Figure 13, flocculated particles either form discrete aggregates or a gel (a continuous three-dimensional network). Since shear may readily break the forces, which are frequently quite weak, enough stress can be applied to rupture the flocculated network and cause the suspension to start flowing. The yield stress is the pressure at which such a breakdown takes place.Thus, flocculation results in plastic behavior, where the forces keeping particles together are reflected in the yield stress.

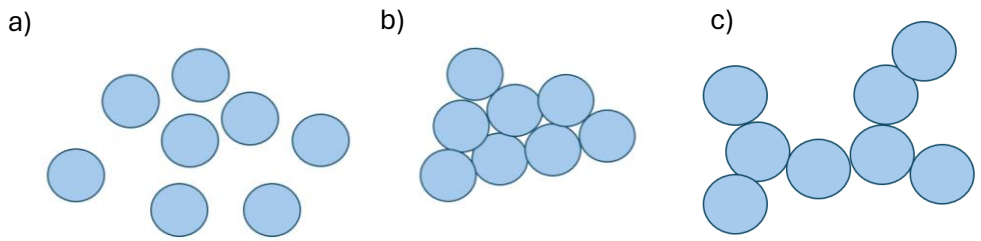


Figure 13. Showing the suspension microstructures. a) dispersed, b) agglomarated or aggregated and c) gelled. Adapted from [163].

Even though the suspension flows, this breakdown is frequently not complete at the yield stress, and as the strain rate is increased further, the flocculation that is still there gradually becomes less pronounced. When a continuous stress level is applied, this condition results in pseudoplastic (shear thinning) behavior, which is frequently accompanied by thixotropy, a progressive and reversible drop in viscosity. It is usual to refer to high strain rates, even with pseudoplastic behavior, as yield stress. In this situation, yield stress is calculated by extrapolating back to zero from the roughly linear curve.

While dispersed suspensions often behave like Newtonian systems, when concentrations are high enough, they can exhibit pseudoplastic behavior with a low yield stress. Thus, concentration and degree of offlocculation both affect yield stress and viscosity. Because crowding limits the capacity of particles to flow, dispersed suspensions exhibit plastic behavior at high concentrations. The yield stress in these suspensions increases with concentration. It can be challenging to distinguish between a dispersed yet highly

concentrated suspension and a flocculated suspension based only on the flow curve because both high concentration and flocculation result in plastic or pseudoplastic behavior.

Equation 20 states that viscosity rises with concentration, despite the fact that the parameters only have physical importance for a dispersed dispersion. As concentration rises, so does the yield stress. A power law is typically used to describe this relationship:

$$\tau_{ys} = \frac{\phi^2}{a^2}\Phi'_{max} \tag{22}$$

where $a^2$ is the greatest interparticle force and $\Phi'_{max}$ is the particle radius [163][164][165][166].

### 3.6. DLVO theory

The DLVO theory (named after Boris Derjaguin, Lev Landau, Evert Verwey, and Theodoor Overbeek) describes the force between charged surfaces interacting through a liquid medium and provides a quantitative explanation for the aggregation and kinetic stability of aqueous dispersions. It combines the electrostatic repulsion caused by the so-called double layer of counterions with the van der Waals attraction. The stability of colloidal dispersions is determined by the DLVO theory, which takes into account the interaction between van der Waals and electrostatic forces. In line with the theory: 1) stable dispersion: Colloidal particles stay distributed in the medium if the repulsive forces (electrostatic and steric) outweigh the attractive forces (van der Waals) and 2) unstable dispersion: Colloidal particles have a

tendency to agglomerate and form bigger clusters or precipitates when repulsive forces are outweighed by attractive forces.

One key idea in colloidal suspensions is the rate at which suspended particles settle in a dispersed phase. One of the first hypotheses, Stokes' law, defines the sedimentation velocity ($u$) of suspended particles as follows:

$$u = \frac{d^2(\rho_s - \rho_f)}{18n} g \tag{23}$$

where g is the gravitational constant, n is the fluid (suspending medium) viscosity, and $\rho_s$ and $\rho_f$ are the particle diameters and solid and fluid densities, respectively.

Electrostatic interactions are caused by charged colloidal particles in an electrolyte solution, and these interactions influence the suspension behavior. Adsorbed ions, surfactants, or dissociated charge groups can all contribute to a particle's charge. Particles have electrostatic potentials that primarily control their colloidal interactions, such as those found in adjuvants containing aluminum. A double layer forms in the solution as a result of the charge on the particles. The osmotic pressure produced by counterions between two particles causes a repulsive force to arise from the overlap of these electrical double layers.

The London–dispersion, Debye, and dipole–dipole forces are among the components of the van der Waals attractive interaction force that cause particles to be attracted to one another. In the colloidal instance, when two particles are near to one another, the electron cloud of the

nearby particle polarizes each of the particles, resulting in attractive attraction that holds the particles together.

The well-known DLVO theory combines attractive London–van der Waals interactions with electrostatic potential owing to repulsive electrostatic double layer to explain particle interactions. The double layer force stabilizes the suspension, whereas the van der Waals force encourages coagulation. According to DLVO theory, Figure 14 shows the electrostatic potential (interaction energy) between two particles as a function of their distance from one another.

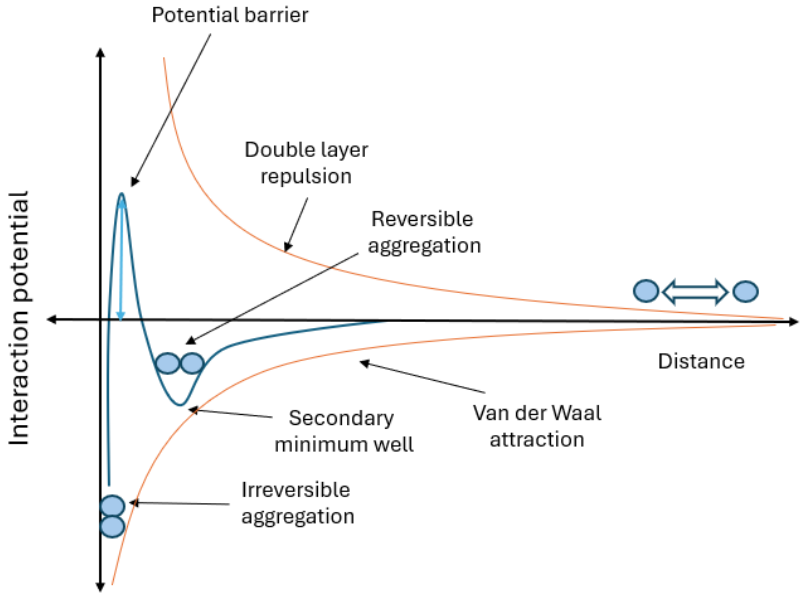


Figure 14. Interparticle repulsion-attraction behaviour of particles in a colloidal dispersion according to DLVO theory. Adapted from [167].

A strong attraction at short distances (primary energy minimum or potential well), an electrostatic repulsion at intermediate distances, and a very weak attraction at long distances

(secondary energy minimum) can all be used to characterize the interaction between two particles. Figure 14 shows that the interaction energy (potential) approaches zero as the distance between two particles increases. But as the particles get closer to one another, they begin to feel attracted to each nother, and DLVO behavior describes their entire interaction.

The secondary minimum potential well in the DLVO curve causes flocculation, or the weak force attraction of particles to one another in a colloidal system, which accounts for the non-monotonic behavior of the curve. Particles can adhere to one another and form aggregates/agglomerations if the interaction energy of this secondary minimum is on the order of the thermal energy ($k_BT$). The rheological suspension behavior, including yield structure and viscoelasticity, is influenced by the aggregated structure. Adhesion is reversible, but particle-to-particle contact is weak at the secondary minimum.

Particles are going to sense a potential energy barrier as they get closer to one another, preventing them from coming into contact and exerting electrostatic force to stabilize the system. The stability of a particular colloidal system is determined by the height of the barrier. The zeta-potential (explained below) is connected to the highest electrostatic repulsion energy. Still, some particles could be able to get through the potential energy barrier and reach the minimum energy potential well if shear is used to provide external energy to the system. It might be difficult to separate particles once they are in the minimal energy well unless a very strong shear energy is used, like sonication, to split the two main particles.

The stability of colloids is strongly dependent on the medium pH. Particles in solution aggregate because the reduction of the charged surface groups reduces the repulsive potential

of interaction at pH values that are close to to the isoelectric point of the nanoparticles. Similarly, the charged surface groups can stabilize the formulation at pH values that are far from the nanoparticle isoelectric point [168][169][170][171][167].

### 3.7. Ball-milling

In the fields of materials science, chemistry, physics, and engineering, ball milling is a frequently utilized method for a variety of tasks, including mechanical alloying, powder metallurgy, and nanoparticle production and to grind materials into fine powders by applying impact, shear, and friction forces to the material using a revolving cylindrical drum full of grinding balls is used. The ball-milling method has a number of benefits, including as simplicity, scalability, and versatility.

For mechanochemical applications wherever there are strict requirements for speed, fineness, purity, and repeatability, planetary ball mills is the best choise. It is easy to reach grind sizes in the low  or even nanoscale range with them, as they grind and combine soft, medium-hard to extremely hard, brittle, and fibrous materials. Each grinding jar in the planetary ball mill is called "planet" and is situated on what is known as the "sun wheel," a circular platform. Every grinding jar revolves on its own axis, but in the opposite direction when the sun wheel turns. The activation of centrifugal and coriolis forces causes the grinding balls to accelerate rapidly.

However, it also has limitations, such as the potential for contamination from the grinding media and equipment wear, which need to be carefully considered and addressed in experimental design and process optimization [172][173][174][175].

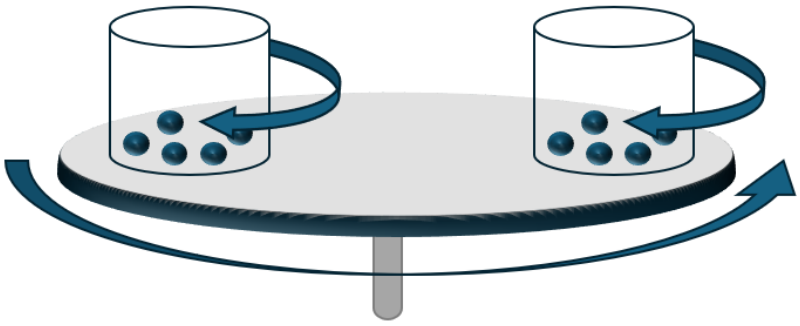

Figure 15. Schematic representation of a planetary ball-milling.

### 3.8. Scanning electron microscope

With a broad variety of magnifications, electron microscopy techniques offer detailed information on shape, structure, and content. They are also quite versatile. An invaluable adjunct to optical microscopy is scanning electron microscopy (SEM), particularly when analyzing the surface characteristics, topography, and texture of powders or solid objects. SEM equipment provide images that are clearly three-dimensional because of their increased depth of focus.

Focusing electrons in a microscope is essential to producing images with them. Multiple electromagnetic lenses are a feature of electron microscopes. In scanning electron

microscopy (SEM), a small patch on the sample's surface that is 50–500 Å in diameter is concentrated by electrons that are accelerated between 5 and 50 keV and released from the electron cannon. The sample is routinely scanned by the electron beam, which has a typical penetration depth of up to 2 μm depending on the electron energies and the sample properties.

An enhanced image of the sample appears on a fluorescent screen as a result of the electrons that flow via a set of lenses, including the objective, intermediate, and projection lenses. You can snap pictures if you'd like. Images are recorded using back-scattered electrons as well as secondary electrons, and equipment combinations are tailored to maximize topographic contrast. Between the lower resolution limit of optical microscopy (about 1 μm) and the maximum feasible working limit of transmission electron microscopy (approximately 0.1 μm), scanning electron microscopy (SEM) spans this magnification range. Nonetheless, SEM can be used in a wider range, from approximately $10^{-2}$ to approximately 2 μm.

Scanning electron microscopy (SEM) is primarily used to examine materials under high magnifications, providing information about their sizes, forms, and compositions as seen from solid surfaces. The data acquired complements optical microscopy results by offering submicron-sized feature details. Furthermore, SEM examination can cover features as large as hundreds of microns [176].

### 3.9. X-ray diffraction

X-ray diffraction (XRD) is a technique that can be used to examine the crystal structure of crystalline materials. It offers comprehensive details about how atoms or molecules are arranged within a material, assisting scientists in determining the chemical composition, examining crystal phases, figuring out crystallographic orientation, and measuring different structural factors.

X-rays are scattered in all directions when they strike a material with a single wavelength that is on the same order of magnitude as the atomic spacing in that material. However, x-rays that strike specific crystallographic planes at specified angles become stronger rather than annihilated. This is because the majority of radiation scattered from one atom cancels out radiation scattered from other atoms. We refer to this phenomena as diffraction. When circumstances meet Bragg's law, the x-rays are diffracted or the beam is amplified:

$$sin\theta = \frac{\lambda}{2d_{hkl}} \tag{24}$$

where $d_{hkl}$ is the interplanar distance between the planes that produce constructive reinforcement of the beam, λ is the wavelength of the x-rays, and θ is half the angle between the diffracted beam and the original beam direction (Figure 16). In order to comply with Bragg's law, a minimum of certain powder particles (crystals or aggregates of crystals) must have their planes (hkl) orientated at the correct θ angle when the material is formed as a fine

powder. Consequently, a diffracted beam is created, which makes an angle of 2θ with the incident beam.

A moving x-ray detector records the 2θ angles at which the beam is diffracted, producing a distinctive diffraction pattern. Knowing the x-rays' wavelength allows us to calculate the interplanar spacings and, ultimately, identify the planes that are causing the diffraction. A high-energy electron beam is used in an XRD device to blast a metal target in order to produce x-rays. Typically, x-rays emitted from copper have a wavelength $\lambda \cong 1.54060$ Å ($K_{\alpha 1}$ line) and are used [177][178].

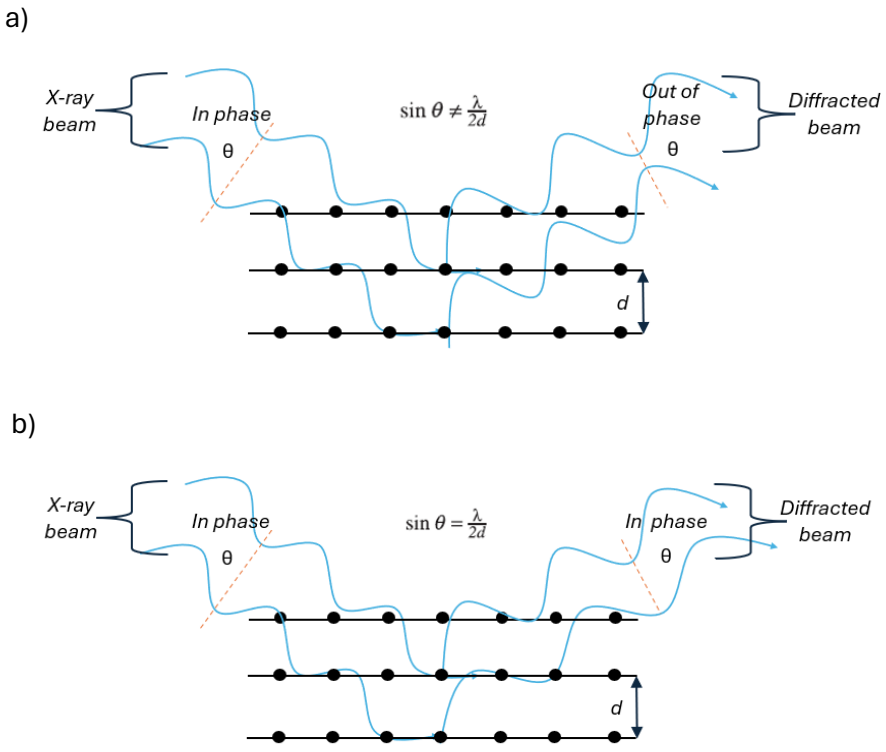


Figure 16. Schematic representation of X-ray diffracted beams a) out phase and b) in phase. Adapted from [178].

### 3.10. Fourier Transform Infrared spectroscopy

FTIR, or Fourier Transform Infrared Spectroscopy, is a flexible analytical method that uses an object's absorption of infrared light to identify and describe both organic and inorganic chemicals. Important details regarding the chemical bonds and functional groups contained in a sample can be obtained by FTIR spectroscopy. It is a quick, non-destructive method that involves little sample preparation and offers insightful information about the molecular makeup and structure of a variety of materials. Since molecular vibrations and symmetry are intimately related, an infrared spectrum of a molecule can often be used to precisely define how it is bonding on surfaces or as a constituent of a solid phase.

The electromagnetic spectrum's infrared region, or $10^{12}$–$10^{14}$ Hz in frequency, is found between 10 and 10,000 $cm^{-1}$. The frequency of molecular vibrations and this frequency overlap. Infrared radiation has the ability to cause a shift to a higher energy level when its frequency matches that of a molecule vibration. It will only cause this transition if it creates a dipole. A molecule's atoms moving without causing a rotational shift in the center of mass is called a genuine molecular vibration. Known as the normal modes are vibrations that adhere to this description.

The normal modes of a nonlinear molecule can result from in-plane or out-of-plane bending, as well as from symmetric or asymmetric stretching. When subjected to infrared radiation, not all of a molecule's normal mode vibrations will become active. Rather, the amount and position of infrared-active peaks in a molecule will depend on its symmetry. Organic

molecules are always moving at room temperature and exhibit a variety of vibrational modes, including stretching, bending, and twisting, as shown in Figure 17.

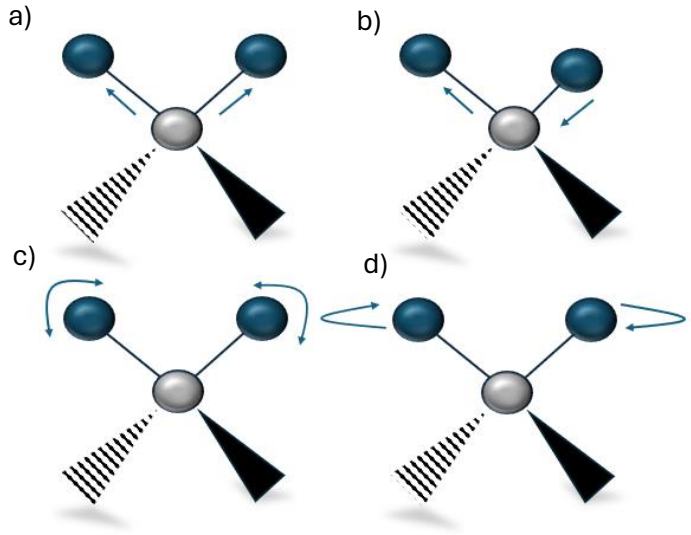


Figure 17. Molecular vibrational modes a) symetric stretching, b) asymetric stretching, c) scissoring (in plane bending) and d) twisting (out of plane bending).

A molecule will absorb infrared light at a frequency that corresponds to one of its bond vibrations when it is subjected to this type of radiation. The bond is able to increase its vibrational amplitude due to the absorbed infrared light, but its vibrational frequency stays constant [179][180].

### 3.11. Ultraviolet-Visible spectroscopy

Optical spectroscopy is based on the Bohr-Einstein frequency relationship:

$$\Delta E = E_2 - E_1 = hv \qquad (25)$$

This connection establishes between the frequency v of electromagnetic radiation and the discrete atomic or molecular energy states $E_i$. Planck's constant, *h*, is the proportionality constant (6.626 x $10^{-34}$ J s). It is appropriate to use the wavenumber v rather than frequency v in spectroscopy. Equation 25 then adopts the following form:

$$\Delta E = E_2 - E_1 = hc\check{\nu} \tag{26}$$

Where:

$$\nu = \frac{c}{\lambda} = c\check{\nu} \tag{27}$$

Thus, particular energy-level variations can be linked to radiation of frequency $\check{\nu}$ or wavenumber *v*, whether it is emitted or absorbed. In terms of absorption spectroscopy in the visible (VIS) and ultraviolet (U-V) regions, the data in Figure 18 can be used to describe this range.

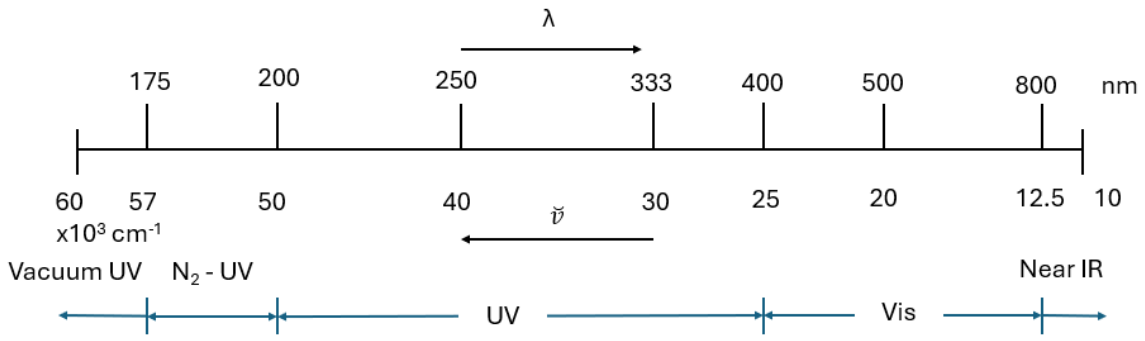


Figure 18. Range of electronic of UV-Vis spectra and its limits.

UV and VIS absorption spectroscopy cover just a relatively small portion of the whole electromagnetic radiation spectrum in terms of frequency or wavenumber. However, because

the energy differences in this range match those of the electronic states of atoms and molecules, it is extremely significant.

The mathematical and physical foundation for light-absorption measurements on gases and solutions in the UV, VIS, and IR regions is the Bouguer-Lambert-Beer law:

:

$$ln\left(\frac{I_0}{I}\right)_{\hat{\nu}} = ln\left(\frac{100}{T(\%)}\right)_{\hat{\nu}} \equiv A_{\hat{\nu}} = \varepsilon_{\hat{\nu}} \cdot c \cdot d \qquad (28)$$

Where:

$A_{\hat{\nu}} = ln\left(\frac{I_0}{I}\right)_{\hat{\nu}}$ is the absorbance

$T_{\hat{\nu}} = \frac{I_0}{I} \cdot 100$ is the transmitance

The dimensions of the molar extinction coefficient, $\varepsilon_{\hat{\nu}}$, are L mol$^{-1}$ cm$^{-1}$. The concentration of the light-absorbing material is denoted by c, the pathlength of the sample in centimeters is represented by d, and the intensity of the monochromatic light entering and exiting the sample is shown by $I_0$ and I, respectively. The substance's molar extinction coefficient, $\varepsilon_{\hat{\nu}}$, is a quantity that is dependent on wavelength λ (nm) and wavenumber (cm$^{-1}$). The idea that the extinction coefficient ε is independent of the concentration of a material at a given wavenumber $\nu$ (wavelength λ) is known as the Bouguer-Lambert-Beer law, which is a limiting law for dilute solutions.

A small amount of the light is lost during measurement in quartz cuvettes (UV-VIS area) or cuvettes made from special optical glass (VIS region) due to reflection at the cuvette surfaces. A reference measurement is made in a cuvette that has the same path length as the substance to be measured, but does not include it, in order to remove this potential source of mistake. Since solutions are used for the majority of UV-VIS spectroscopy, the pure solvent found in the standard cuvette should ideally not absorb in the spectral area being studied [181].

### 3.12. Electrochemical impedance spectroscopy

A powerful analytical method for examining many of the electrical characteristics of materials and their interactions with electrically conducting electrodes is electrochemical impedance spectroscopy, or EIS. It offers key information regarding the events that take place at the interfaces between electrodes and electrolytes, including mass transport phenomena, double-layer capacitance, and charge transfer reactions.

Since EIS is a steady-state method that uses small signal analysis and can measure signal relaxations over a very wide range of applied frequency, from less than 1 mHz up to more than 1 MHz, using commercially available electrochemical working stations, it offers several advantages over the other electrochemical technique.

When we discuss interfaces, we need to visualize an electrochemical cell, in which two metallic electrodes are introduced into an ion-containing electrolyte solution. Ions begin to flow toward the electrode surface as a result, and two things can happen: either the chemical

reaction produces electrical energy, in which case we have a galvanic cell; alternatively, the chemical reaction produces electrical energy, in which case we have an electrolytic cell.

Charges (electrons or ions) are transferred across the electrode-electrolyte interface in an electrolytic cell. Ions from the liquid gathered at the electrode's surface when they are submerged in an electrolyte solution. This results in the formation of an area known as the electrical double layer (DL), also known as the Helmhotlz DL. This region is utilized to visualize the properties at the bulk-liquid phase as well as the ionic environment at a charged surface in a solid-liquid interface. Assumed by the Helmholtz DL was:

- No electron reactions occurred at the the electrode and the solution is composed only of electrolyte.
- Charges will not be uniformly distributed throughout the liquid phase, but will be concentrated near the charged surface a small but finite volume of the liquid phase which is different from the bulk liquid

A diffuse layer is created between these interfaces, where the concentration of ions with opposing charges decreases with increasing distance from the surface. Moreover, this model was further adjusted to account for the radious of ion species in the electrolyte that are unable to approach the surface of the metallic electrode any closer than their ionic radius, explaining a more realistic behavior occurring in a solid-liquid interface. The Stern layer is where ions that are oppositely charged are attached to the metal surface, the Inner Helmholtz Plane (IHP) is where the potential charge decreases linearly, and the Outer Helmholtz Plane (OHP) is the

zone where solvated cations and ions present this exponential decline in opposite charge gradient (Figure 19)

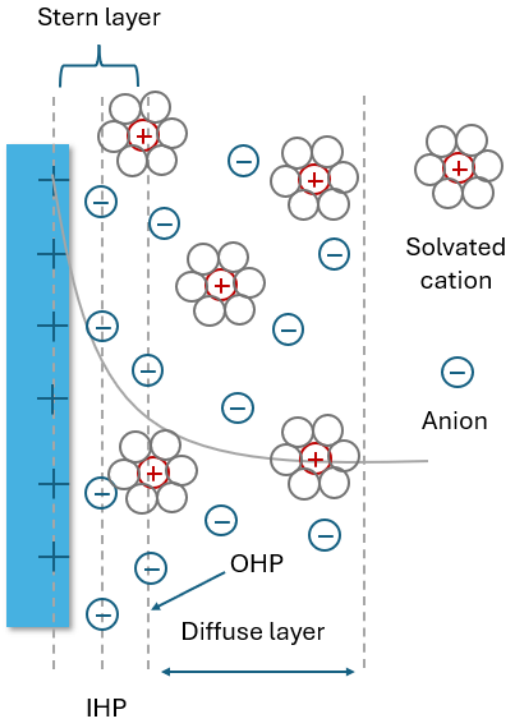


Figure 19. Schematic representation of a charged metalic surface summerged in an ionic electrolyte. Adapted from [182].

We can only measure the open circuit voltage when an electrode is submerged in an electrolyte and is in the equilibrium condition, where there is no net current flow. To study our system, we must apply a small alternating (AC) voltage perturbation wave that is frequency dependent in order to push the system away from equilibrium. This allows us to identify diffusion-limited reactions, distinguish between electrochemical reactions, and gather data on capacitive behavior (charge accumulation at the metallic electrode). A broad Ohm's law representation of this AC approach can be formulated by:

$$V = iZ \tag{29}$$

Z is the impedance, which is defined as any frequency-dependent resistance to the current flow, such as capactiance, resistance, inductance, diffusion, etc., where V is the potential, i is the current.

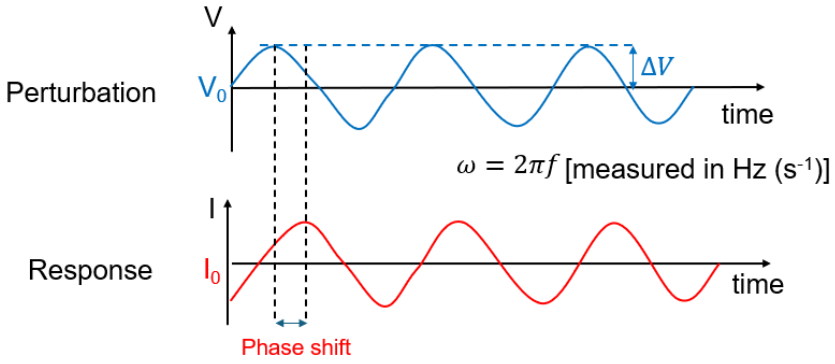


Figure 20. AC small potential perturbation applied and response in current out of phase.

When changing the frequency of the perturbation, a resistance against the current flow in specific circuit element in the system is going to be generated.

The potential applied and the obtained current response sinudoidal signals are both a function of frequency and have a magnitud and phase, the ratio of magnitud of these two waves determine the impedance by a phase difference:

$$V = dVsin(\omega t) \tag{30}$$

$$I = dIsin(\omega t + \phi) \tag{31}$$

Where, V and I is the instantaneous value, dV and dI is the maximum amplitud, t is the time, ϕ is the phase offset between two waves and ω is the angular frequency 2πf. Equations 30 and 31 can be rewrited as:

$$|Z| = \frac{sin(\omega t)}{\sin(\omega t + \phi)} \tag{35}$$

Using Euler's relationship, we obtain for imaginary numbers:

$$Z(\omega) = |Z|[\cos(\phi) + jsin(\phi)] \tag{32}$$

Where j is the square root of -1.

EIS data is typically presented as vectors and a complex quantities, both mathematically equivalents. The vector plot, called Bode plot, is presented by the impedance magnitud and the phase angle and the complex plane, calle Nyquist plot is represented by a real and imaginary part of the impedance (Figure 21)

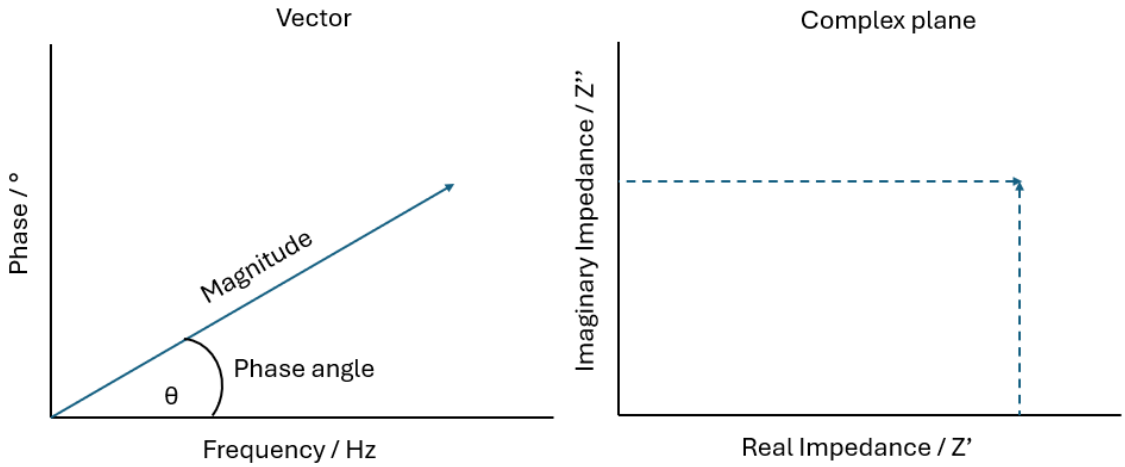


Figure 21. Vector (left) and complex plane (right) plots for EIS data representation.

In the Bode plot we can observe how the magnitud and phase is changing along the frequency perturbation and the Nyquist plot shows how the each part part with its imaginary component changes along the frequency perturbation, starting from hight to low frequencies from left to right.

In EIS one part of the J-V curve is selected and a small enough perturbation applied in order to obtain a linear response of the system that will allow us to get a better insight into the internal proccesses ocurring at different time scales (Figure 22).

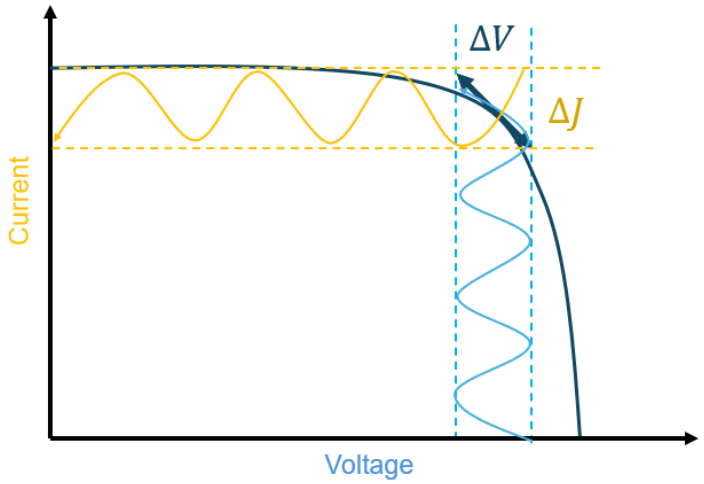


Figure 22. Schematic representation of a small AC potential perturbation and its currect respond in a small area of the I-V curve.

The system is simulated using equivalent circuits in order to examine the resulting spectra. Several elements are used to create a equivalent circuit, in which each element's behavior varies as the frequency changes. Figure 23 illustrates the behavior of the most common circuit elements (capacitance, Warburg impedance element, series resistance, and charge transfer resistance) that are used to characterize the behavior of a DSSC.

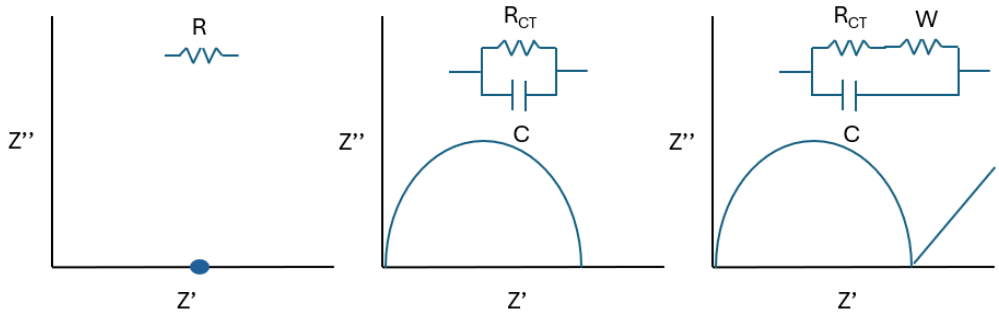


Figure 23. Typical element behaviour in a Nyquist plot. Resistance (left), resistance in parallel with a capacitance (center) and a Warburg resistance witth a series resistance in parallel with a capacitor (right).

Figure 24 (a) depicts the most common equivalent circuit used to analyse the behaviour of a DSSC and the differente circuit elements used (1 - 4). Figure 24 (b) and (c) shows the typical Nyquist and Bode plot obtained using this equivalent circuit and the different zones where each circuit element has an effect.

In the Nyquist plot the frequencies are displayed in the x-axis from high to low from left to right (Figure 24 (b)) At very high frequencies, current will flow through all circuit elements and the $R_s$ value will be where the first semicircle starts on the left (Figure 24 b), (1)). In this model, the resistance of the TCO on the left and other resistances are combined into $R_s$. At the electrolyte/counter electrode interface (Figure 24 a) , (2)), the parallel combination of $R_{ct}$ and $C_{CE}$ is designated to the high frequency semicircle (Figure 24 b), (2)). This small semicircle become smaller when $R_{ct}$ decreases when the counter electrode's catalytic propertie improves. The $TiO_2$/electrolyte interface's charge accumulation and recombination reaction (Figure 24 a), (3)) are related to the intermediate frequency semicircle (Figure 24 b), (3)). As a result, when $R_T$ increases, the middle semicircle may increase (increasing recombination reaction). The Warburg diffusion of the ions in the electrolyte (Figure 24 a), (4)) is responsible for the final low frequency tail (Figure 24 b), (4)) which is often related with mass transport problems in the electrolyte. It is important to note that most of DSSCs do not often display this third semicircle. In the Bode plot the frequencies are desplayed in the x-axis from high to low from right to left (Figure 24, b)). The Bode plot allows a straightforward determination of a system's characteristic frequencies by displaying the peak positions along the x-axis. The electron lifetime in the $TiO_2$ layer is one significant parameter that may be determined from the Bode plot by looking at the location of the mid-frequency

peak (Figure 24 c), (3)). The electron time-life extends and the recombination reaction decreases when the peak's position shifts toward the higher frequency domain [183][184][185].

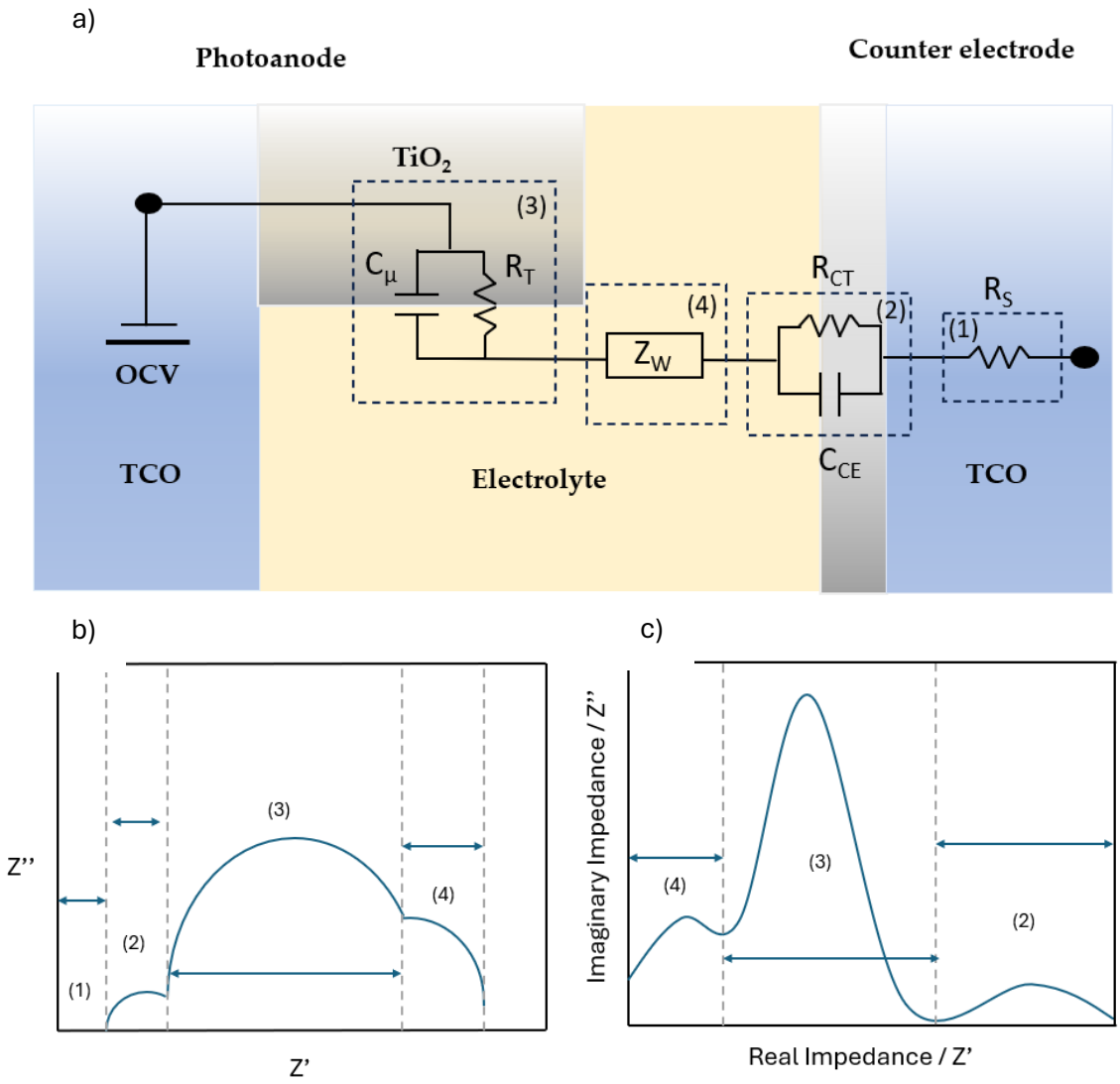


Figure 24. a) Equivalent circuit for a DSSC. Nyquist b) and Bode c) plots showing characteristics signals. Adapted form [183].

# MATERIALS AND METHODS

## 4.1. $TiO_2$ nanoparticle synthesis

In the following, synthesis of three different $TiO_2$ phases is described.

### 4.1.1. Anatase

$TiO_2$ anatase nanoparticles were synthesized through a sol–gel approach followed by a hydrothermal treatment. pH was monitored in key stages of the whole process using a pHmeter (Hanna Instruments HI 2210). In the following, synthesis processes are described:

a) Initially, 4.04 mL of glacial acetic acid (ACS reagent, ≥99.7%, Sigma-Aldrich) was combined with 21.22 mL of titanium (IV) isopropoxide (97%, Sigma-Aldrich), and the mixture was stirred for 15 minutes (pH = 7.2 at 21°C).

b) This solution was then gradually added dropwise to 145 mL of deionized water (DIW) while stirring (pH = 2.8 at 21°C).

c) After an additional hour of stirring, 1.4 mL of nitric acid (ACS reagent, 70%) was introduced as a peptizing agent (pH = 1.22 at 21°C). The sol–gel reaction mixture underwent heating from 25 °C to 80 °C at a rate of 1.5 °C/s, followed by reflux conditions at this temperature for 1 hour and 40 minutes.

d) The resulting transparent blueish dispersion was left to stir overnight. Subsequently, 30 mL of the $TiO_2$ sol–gel precursor solution (pH = 1.08 at 20°C) was placed in a 45 mL Teflon-

lined autoclave (Parr Instruments), and a hydrothermal treatment at 200 °C for 24 hours was conducted in a furnace.

e) The resulting slurry (pH = 3.3 at 21 °C) underwent washing with ethanol, followed by centrifugation at 4500 RPM for 10 minutes (ST8 Benchtop Thermo Scientific Centrifuge, China, Langenselbold, Germany) to eliminate excess organic compounds from the acids used. This washing process was repeated three times until a pH of 7.30 at 26 °C was reached.

### 4.1.2. Rutile

$TiO_2$ rutile nanoparticles were synthesized in a similar way as anatase nanoparticles through sol–gel and a post-hydrothermal treatment. In order to promote the rutile crystalline phase formation the synthesis process was slightly modified as follows:

Step a) and b) remained the same. In step c), 4 mL of nitric acid was used to decrease the pH of the solution (pH = 0.75 at 22.1 °C). In step d), the colloidal solution before being placed in the teflon vessel for the hydrothermal treatment was pH = 0.56 at 22.3 °C. Finally, in step e), the pH of the slurry obtained after the hydrothermal treatment was 3.23 at 18.1 °C. After the washing proccess, pH reached 5.5 at 18.1 °C.

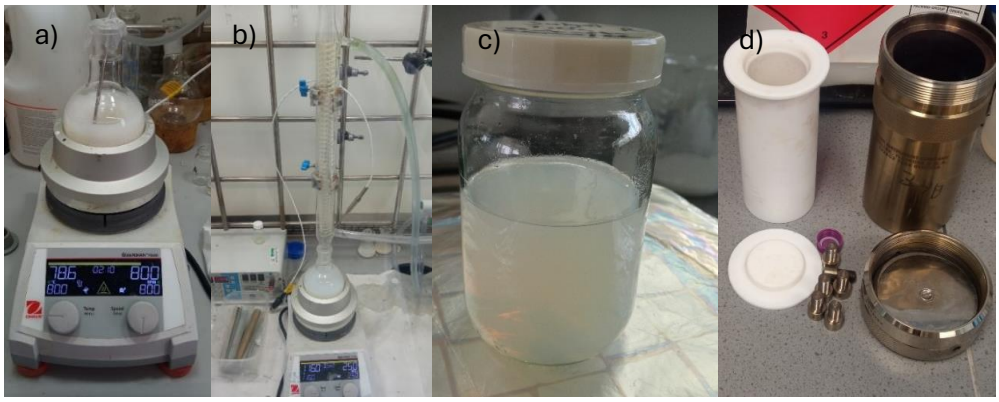


Figure 25. White sol-gel mixture at 80 °C (a) and sol-gel under reflux (b) (step c). Resulting transparent blueish dispresion (d), 200 mL teflon vessel and autoclave digestor for hydrothermal treatment (d) (step d).

### 4.1.3. Brookite

The following describes how amorphous titania was made. A flask holding 105 mL of IPA and 1.14 mL of deionized water (18 MΩ cm) was set up in a salt-ice bath at 0 °C using a magnetic stirrer. 105 mL of IPA and 5 mL of titanium (IV) isopropoxide were combined in a different flask. While stirring and keeping the temperature at 0 °C, the first solution was added to the second solution. In these settings, the combined solution was stored for one hour. After that, the suspension was kept at room temperature for 24 hours while being stirred (ure 5). The suspension solution was dried at room temperature after being filtered three times to get the amorphous titania powder. After that, $TiO_2$ was mixed with a 3 M HCl solution.

$TiO_2$ in the solution reached a final concentration of 0.3 M. The solution was then hydrothermally treated for six hours at 180 °C in an autoclave lined using Teflon. Deionized

water was used to wash and centrifuge the finished product three times. To achieve extremely pure brookite, the liquid supernatant was separated from the precipitated solid residue and dried at 80 °C. The finished product was dried at 80 °C after being repeatedly cleaned with ethanol and deionized water.

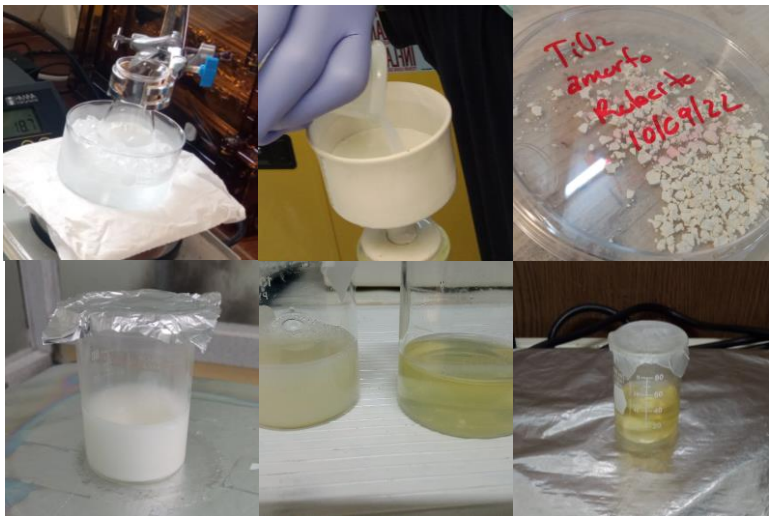

Figure 26. $TiO_2$ brookite phase synthesis process.

### 4.2. $TiO_2$ pastes for low-temperature and flexible DSSC.

In this work, chemically sintered photoelectrodes were prepared for the fabrication of low-temperature and flexible solar cells from the synthesis of $TiO_2$ to the characterization of the final devices. Three pastes (A - C) with different formulations were prepared using $TiO_2$ particles in two crystalline phases, anatase and rutile, water, and $H_2TiF_6$ as a particle interconnection agent. In the first stage, paste A was used to find an optimal formulation for iodide electrolyte that could enhance the performance of low-temperature systems. A paper with these findings was published (**Aviles-Betanzos**, R., Pourjafari, D., Oskam, G. *Energies*,

2023, **16**, 5617). In the second stage, in order to improve the transparency of the films, reduce the film thickness, and enhance particle interconnectivity characteristics, the formulation and processing of three pastes was changed (B – C). In addition, using the best paste formulation, photoelectrodes were prepared using cutting-edge components such as Y123 dye and Cu redox electrolyte and a novel assembly method was used to further improve the efficiency of the low-temperature devices. Fabricated devices were tested with the previously optimized electrolyte in stage one and compared with the copper electrolyte. Photovoltaic characterization of devices were performed under simulated sun and indoor light. Electrochemical impedance spectroscopy measurements were performed to have a better insight into the internal electronic behaviour of these devices. Finally, flexible DSSCs were fabricated using the optimal configuration.

### 4.3. Electrodes preparation

Conductive glass substrates ITO/Glass (8 Ω/sq, 2 × 2 cm, 2.2 mm thick) were employed as the photoanode and counter electrode for stiff devices. Conductive polymer ITO/PEN (≤ 10 Ω/sq, 0.125 mm, Peccell) was employed as the photoanode and counter electrode for flexible devices. Before the cleaning procedure, the glass and PEN substrates for the counter electrodes were pierced to enable electrolyte injection into the devices. On the non-conductive surface, holes were perfored using a tungsten carbide tip that was 0.8 mm thick. Using paste A, two holes were bored in the substrates for the devices. For devices using paste B – C, a different assembly method was used (described in section 4.11.) and 1 hole was drilled in the substrates. For the cleaning process, substrates are enclosed in a Teflon

receptacle. A solution of liquid soap is applied to fully immerse the substrates. Teflon vessel is then immersed in an ultrasonic bath (40 kHz) (Branson 2800 Ultrasonic Cleaner) for 10 minutes. Subsequently, the soap solution is drained, deionized water is introduced, and the substrates are returned to the ultrasonic bath for an additional 10 minutes. Following the water rinse, ethyl alcohol is applied, and the substrates are subjected to another 10 minute ultrasonic treatment. After the removal of ethyl alcohol, isopropyl alcohol is introduced, and the substrates undergo an additional 10 minute immersion in the ultrasonic bath. Finally, the substrates are extracted from the receptacle and dried using a compressed air gun. UV-$O_3$ treatment was performed to all cleaned devices to further increase surface energy previous to the deposition of pastes using a Novascan PSD Series Digital UV Ozone System.


Figure 27. Teflon container for electrode washing (left) and Branson 2800 Ultrasonic Cleaner (center) and Novascan PSD Series Digital UV Ozone System (right) used for the electrode washing.

### 4.4. PEDOT counter electrodes preparation

A solution of 0.1 M sodium dodecyl sulfate (ReagentPlus®, ≥98.5%, Sigma-Aldrich) and 0.01 M EDOT (3,4-ethylenedioxythiophene, 97%, Sigma-Aldrich) in DIW was prepared. Electropolymerization of poly(3,4-ethylenedioxythiophene) (PEDOT) on the conductive

substrates was performed by using a Gamry potentiostat using a two-electrode configuration and applying a stationary voltage of 2.3 V for 120 s. Counter electrodes with an area two times larger than the working electrode were used. The same substrate type (glass or PEN) was used for both as working and counter electrode.

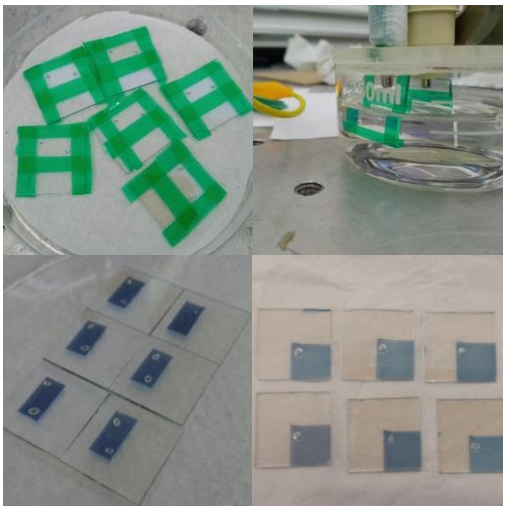

Figure 28. EDOT electropolimerization. a) Masked substrates, b) experimental setup, c) and d) deposited PEDOT on ITO-Glass substrates.

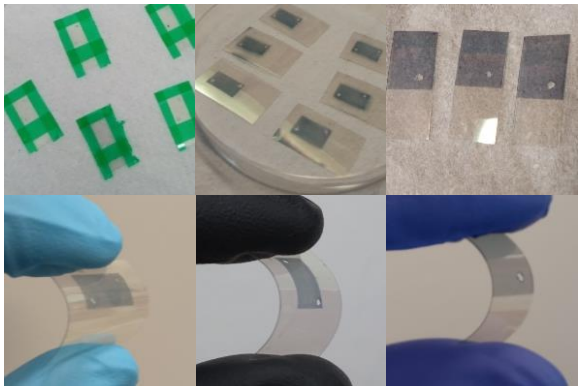

Figure 29. Deposited PEDOT on flexible ITO-PEN substrates using different designs.

### 4.5. Dye baths

Two different dye baths were used in this work. The first dye bath (D1) was prepared using the ruthenium complex di-tetrabutylammonium cis-bis(isothiocyanato)bis(2,2′-bipyridyl-4,4′-dicarboxylato)ruthenium(II) (N719, Ruthenizer 535-bisTBA® from Solaronix, Aubonne, Switzerland). A 0.5 mM solution is prepared in in 1:1 v/v acetronitrile/tert-butyl alcohol (ACS reagent, 99.0%, Sigma-Aldrich). The prepared solution is then subjected to 5-minute soncication to ensure dissolution of the dye molecules in the solution. The second dye bath (D2) was prepared using the organic dye 3-{6-{4-[bis(2',4'-dihexyloxybiphenyl-4-yl)amino-]phenyl}-4,4-dihexyl-cyclopenta-[2,1-b:3,4-b']dithiphene-2-yl}-2-cyanoacrylic acid (DN-F05y (Y123), Dyenamo). 0.1 mM Y123 and 0.2 mM chenodeoxycholic acid (CDCA, Sigma-Aldrich) is disolved in a 1:1 (v:v) acetonitrile:*tert*-butyl alcohol (ASC reagent, ≥99.0%, Sigma-Aldrich) following sonication to ensure dissolution of dye molecules. Subsequently, flasks are covered with aluminum foil and stored in a desiccator.

### 4.6. Electrolyte preparation

Four different redox electrolyte solutions were prepared: (i) ACN:VN; (ii) VA:ACN; (iii) MN; and (iii) Cu. ACN:VN was prepared using 85:15 v/v acetonitrile/valeronitrile (99.5%, Sig-ma-Aldrich) with 0.1 M LiI (99.9% trace metal basis, Sigma-Aldrich), 0.05 M $I_2$ (ACS reagent, ≥99.8%, Sigma-Aldrich), 0.1 M 1,2 -dimethyl-3-propylimidazolium iodide (DMPII, Solaronix), 0.6 M guanidine thiocyanate (≥97% titration, Sigma-Aldrich) and 0.5 M 4,4′-di-tert-butyl-2,2′-dipyridyl (98% Sigma-Aldrich). VA:ACN uses the same compounds as

ACN:VN except these are dissolved in 15:85 v/v acetonitrile/valeronitrile. MN was prepared using 0.1 M $I_2$, 0.1 M LiI, and 0.8 M DMPII dissolved in 3-methoxypropionitrile (≥98.0%, Sigma-Aldrich). For the Cu redox electrolyte a solution 0.6 M 1-Methylbenzimidazole (NMBI, ≥98.0%, Sigma-Aldrich), 0.1 M Bis(trifoluoromethane)sulfonimide lithium salt (LiTFSI, 99.95%, Sigma-Aldrich) in acetronitrile is prepared and stored in the fridge. Following this, a quantity of bis-(4,4',6,6'-tetramethyl-2,2'-bipyridine)copper(I) bis(trifluoromethanesulfonyl)imide ($Cu^{I}(tmby)_2TFSI$, Dyenamo) and bis-(4,4',6,6'-tetramethyl-2,2'-bipyridine)copper(II) bis[bis(trifluoromethanesulfonyl)imide] ($Cu^{II}(tmby)_2(TFSI)_2$, Dyenamo) is weight in order to obtain 0.2 M and 0.06 M, respectively. The previous prepared solution is added to the copper based redox couple and sonicated to ensure complete disolution. All electrolytes were stored in the fridge and sonicated for 15 min previous to be used.

### 4.7. Binder-free aqueous $TiO_2$ pastes

In the following, the formulation of the four pastes used for the low-temprature and flexible DSSCs as well as the deposition and sensitization of films is described.

### 4.8. Paste A

In this section the preparation of paste A is described.

### 4.8.1. Powder cleaning

After the washing method e) applied to the synthesized $TiO_2$ anatase nanoparticles, the resulting viscous compact $TiO_2$ mass was dried at ambient temperature. In order to further purify the $TiO_2$ nanomaterial, two different post-cleaning treatments were employed: (i) a heat treatment at 450 °C for 2 hours, and (ii) UV-$O_3$ treatment for 10 minutes.

### 4.8.2. Paste preparation.

Using the cleaned powder with heat treatment, paste A was prepared as follows: first, 23.25 L hexafluorotitanic acid solution ($H_2TiF_6$, 60 wt.% in $H_2O$, 99.9% trace metals basis, Sigma-Aldrich) was added as an interparticle binding agent to 2.47 mL DIW while stirring, as described by Holliman et al. [102]. Then, 0.75 g of synthesized $TiO_2$ anatase powder was gradually added to this solution, alternating with stirring and ultrasonic bath treatment (Branson 2800, Kukje, USA) in order to break large agglomerates and to assure a well-dispersed solution. A viscous paste was obtained (pH = 2 at 23 °C). The paste was not completely stable since when it was left standing for a day, the material began to settle and it was necessary to apply agitation and sonication before using it.

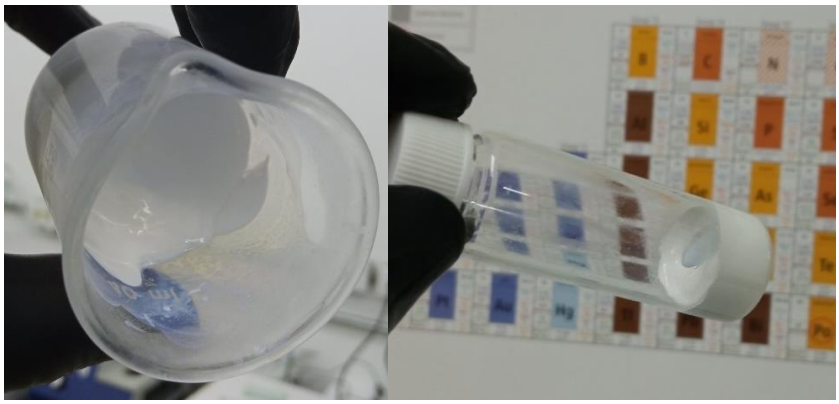

Figure 30. Binder-free aqueous $TiO_2$ paste A

### 4.8.3. Paste deposition and sensitization.

Paste A was deposited by the blading method onto rigid and FPCSs in an active area of the films was 0.5 $cm^2$ using Kapton® tape (30 μm thickness) as a spacer (Figure 31). Films were heated to 120 °C for 15 min to promote interparticle connectivity and adhesion to the substrate. The low-temperature $TiO_2$ films presented strong adhesion to both substrates, and the FPCSs could be bent without detachment of the films. After the low-temperature chemical sintering step, $TiO_2$ films were immersed at 120 °C for 18 hours in D1 dye bath at room temperature. Films were rinsed with acetonitrile to remove dye molecules that are not adsorbed to the $TiO_2$ surface.

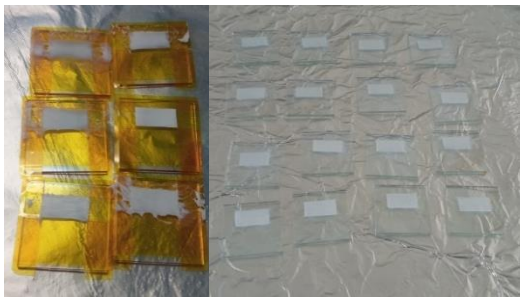

Figure 31. Paste A deposited by blading on ITO-Glass substrates. Paste A deposited on Kapton tape masked substrates (left). Paste A films sintered at 120 °C (right).

Figure 32. Sensitization of paste A films in D1 dye on ITO-Glass substrates using a glass container (left and center). Dye-sensitized paste A films after 18 hours (right).

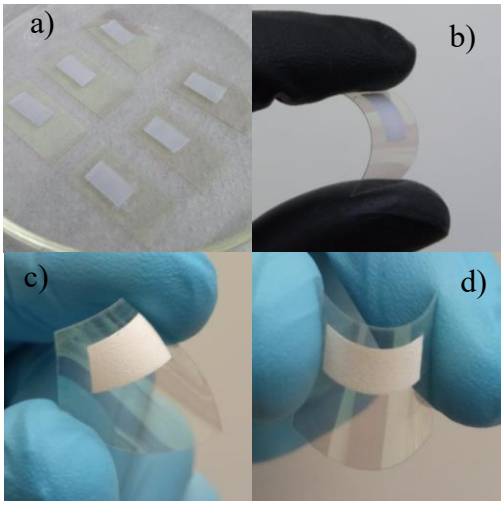


Figure 33. Paste A deposited on flexible ITO-PEN substrates. a) and b) Using a vertical deposition. c) and d) using a horizontal deposition.

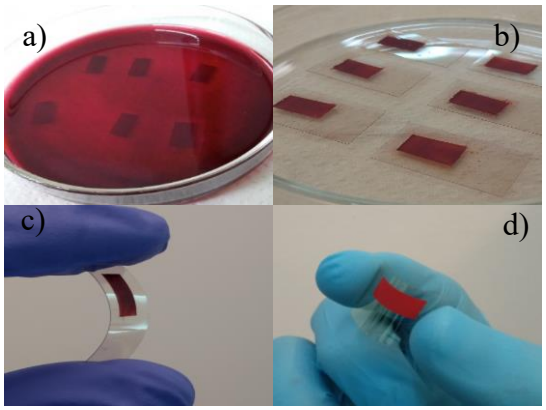


Figure 34. a) Sensitization of paste A films in D1 dye on flexible ITO-PEN substrates using a glass container. b-d) Dye-sensitized paste A films after 18 hours.

### 4.9. Paste B

In this section, the preparation of paste B is described.

#### 4.9.1. Powder cleaning

For powders used in paste B, a slightly different approach for cleaning was used. In order to remove remaining organic compounds on the surface of anatase and rutile powders, two different methods were tested: i) powders were heated at 450 °C for 2 hours prior to the paste preparation as in paste A and ii) UV-$O_3$ treatment using a Novascan PSD Series Digital UV Ozone System at different times instead of using a UV-lamp. The latter was used in order to keep -OH groups on the surface of $TiO_2$ nanoparticles with the aim of obtaining a higher amount of dye molecules adsorbed onto it.

### 4.9.2. Ball milling

To obtain a stable aqueous $TiO_2$ colloidal solution, cleaned powders using both treatments were milled using a Retsch Planetary Ball Mill PM 100. 0.80 g of anatase, 0.20 g of rutile powder were placed in a Retsch 50 mL agate jar with ten 10 mm diameter agate balls (Figure 35). A dry milling was performed setting the program to run for 1 hour at 500 RPM. For the wet mill, 35 mL of DIW was added to the same jar and the program was set to run continuously for 24 hours and 1 hour at 500 RPM for temperature and UV-$O_3$ treated powders, respectively . After leaving the jar to cool down to room temperature, the resultant supernatant white dispersion was carefully transferred to a beaker using a pipette leaving behind, at the bottom fo the jar, the agglomerated particles that could not be broken up (Figure 36).


Figure 35. Retsch Planetary Ball Mill PM 100 (left) and 50 mL agate jars used to process paste B (right).

Figure 36. 50 mL agate jar after wet milling (left). Agglomerated $TiO_2$ nanoparticles left at the bottom of the jar (center). Stable $TiO_2$ anates:rutile (80:20, wt:wt) aqueous solution (right).

### 4.9.3. Paste preparation.

The stable aqueous $TiO_2$ colloidal solution was slowly concentrated to a volume of ~5 mL using a rotary evaporator (~32 wt%). $TiO_2$ interparticle bonding started to form immediately after adding 35 μL of $H_2TiF_6$ under mild stirring (70 RPM). Clumps started to form first at the bottom of the flask, and with careful stirring, a viscous homogenous paste (pH = 2 at 21°C) was finally formed.

Figure 37. Concentration of $TiO_2$ aqueous colloidal solution using a rotary evaporator (left). Viscous paste B (center and right).

### 4.9.4. Paste deposition and sensitization.

For paste B, both heat treated and UV-$O_3$ treated powders, were applied by blading onto rigid substrates using Kapton® tape (30 μm thickness) as a spacer. The active area of the films was 0.45 $cm^2$. After deposition, films underwent 15-minute heating process at 120 °C to enhance interparticle connectivity and substrate adhesion. After this heating process, films showed good adhesion to the ITO-PEN substrates. However, they presented a no entirely transparent appearance which proved that agglomerates were still present in the colloidal solution (Figure 38). Deposited films were sensitized using D1 and D2 baths at 120 °C for 18 and 24 hours at room temperature, respetively, and rinsed with acetonitrile.

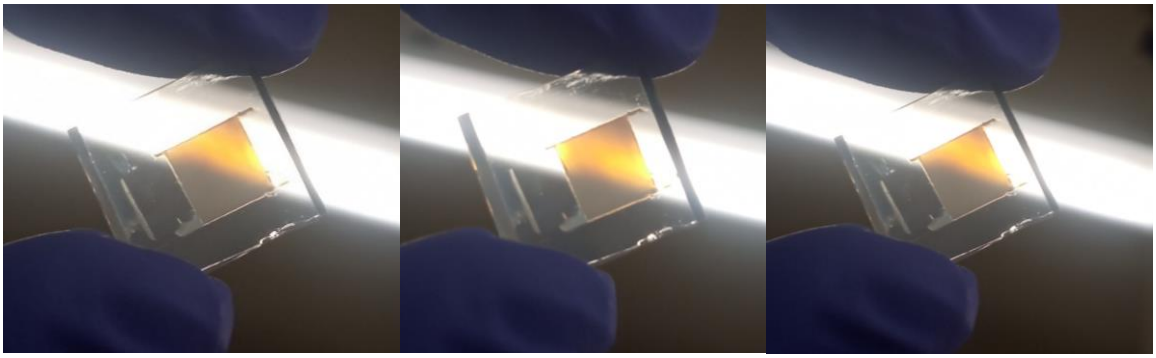

Figure 38. Paste C deposited by blading on ITO-Glass substrates with light in the background at different positions to show the transparency.

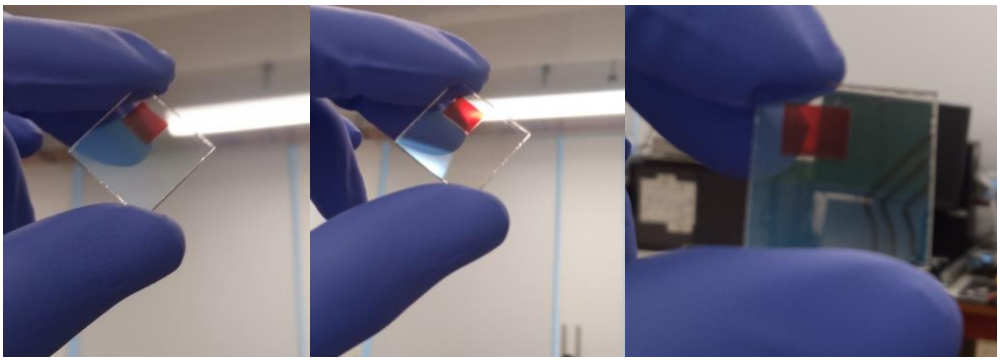

Figure 39. Dye-sensitized paste C films showing transparency with the background at different positions to show the transparency.

## 4.10. Paste C

In this section, the preparation of paste C is described.

### 4.10.1. Preparation, deposition, and sensitization

Paste C is prepared without drying the synthetized $TiO_2$ nanoparticles to powder. After the washing method applied to the synthesized $TiO_2$ (step e in section 4), the resulting viscous compact $TiO_2$ mass is used wet for the paste formulation to ensure a better colloidal dispersion and to obtain less particle agglomeration. To obtain 1 g of dry $TiO_2$ to be used in the paste, an amount of the viscous wet $TiO_2$ colloid is carefully weighed in a small glass container. Then, the ethanol is evaporated placing the glass container in a hot plate at 120 °C. When the solvent is completely evaporated and the container is cooled down at room temperature, the remaining $TiO_2$ powder is again weighed with the same glass container to obtain a dry/wet ratio.

The amount of wet weight needed to obtain 0.75 g of dry $TiO_2$ is then back calculated, 30 mL of DIW is then added to the viscous $TiO_2$ wet mass, left to stir and sonicated until the $TiO_2$ nanoparticles are fully dispersed. The colloidal solution is slowly concentrated to ~4 mL using a rotary evaporator (~32 wt%). After cooling down the solution, 23.25 μL of hexafluorotitanic acid solution is added under slow stirring. The viscous paste formed is slowly stirred to obtain a homogeneous consistency. The paste was deposited by blading on to the subtrates following the same previous procedure. The resulting films showed to be more tranparents compared with films deposited using pastes A and B (Figure 40).

Additionally, in order to further improve interparticle connection another paste is prepared following the same procedure and 0.355 mL of TIIP is added after the addition of $H_2TiF_6$ under mild stirring to obtain a homogeneous viscous paste. To select the best paste to use in low-temperature devices, these 2 pastes were sensitized using the D2 dye bath and dye desorption tests were performed as decribed in section 5.16. According with the results obtained I decided to use TIIP in the formulation of this paste. Paste C was deposited following the same procedure as paste A and B. The deposited films showed higher tranpsarency compared with previous films. Films were immersed at room temperature for 24 hours in D2 dye bath and rinsed with acetonitrile before device fabrication. The performance of these devices were tested using VN:ACN and Cu electrolytes.

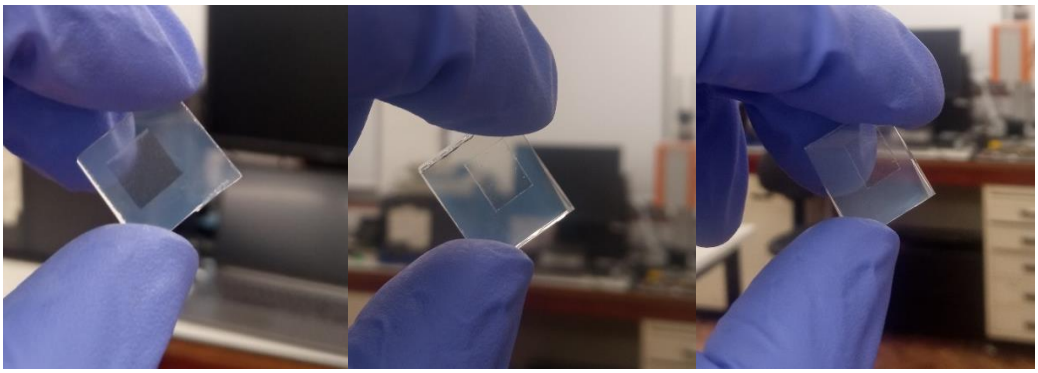

Figure 40. Paste C deposited by blading on ITO-Glass substrates showing improved transparency.

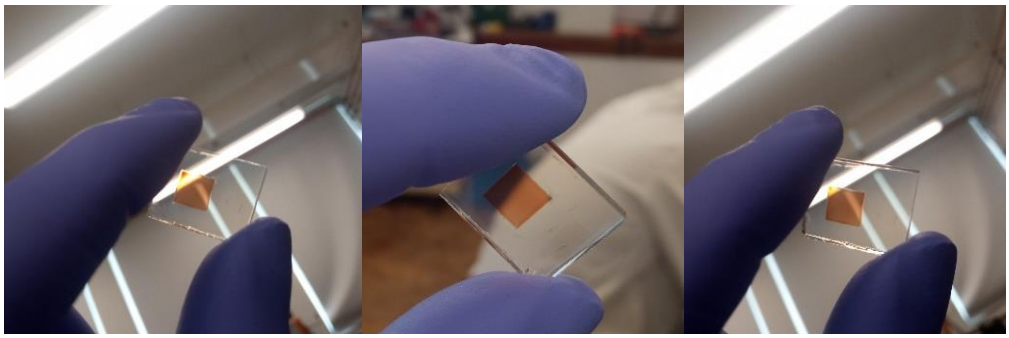

Figure 41. Dye-sensitized paste C films showing improved transparency after sensitization.

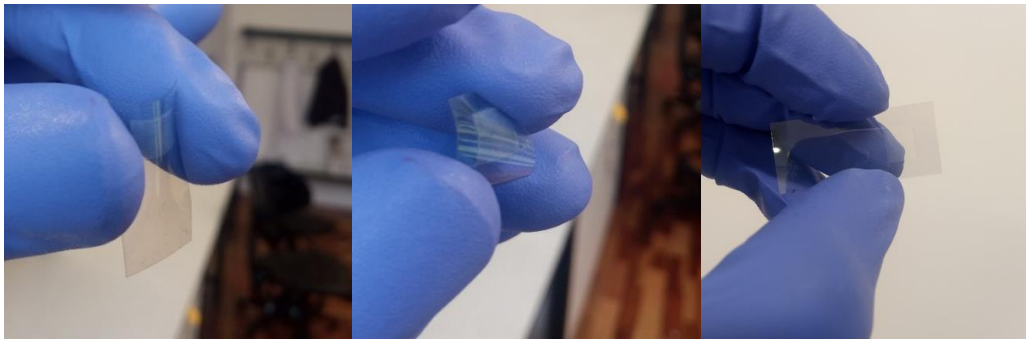

Figure 42. Paste C deposited by blading on flexible ITO-PEN substrates showing improved transparency and adhesion to the substrate after bending.

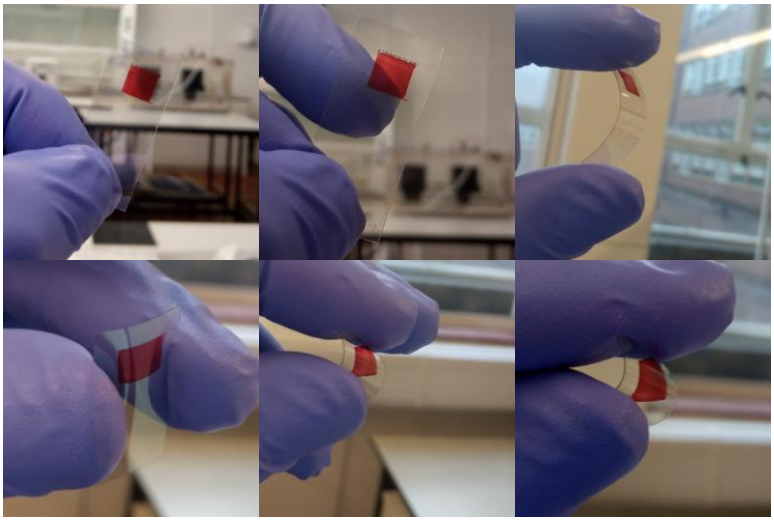

Figure 43. Dye-sensitized paste C films on flexible ITO-PEN susbtrates showing improved transparency and good adhesion after sensitization.

### 4.11. DSSC assembly

In the following, the two different methods employed to assembly devices are described.

#### 4.11.1. Assembly method 1

Devices using paste A were assembled utilizing a UV-curable resin (Threebond® 3035B)(Glue) to attach and seal photo and counter electrode together. The glue is deposited on both rigid and FPCS substrates with the help of an automatic UV-glue three-axis motion dispensing machine AB Glue Dispensing MachineTBS-TC-441. An special syringe is filled with the glue and placed in the dispenser and the container is set to 40 °C to allow the resin

to get a more liquid consistency for an easy and efficient use. First, the counter electrode is placed with the PEDOT layer facing upwards on the dispenser plate and fixed using tape. The dispenser machine is programmed in order to deposit the glue around the PEDOT film (Figure 44). The photo and counter electrodes were subsequently arranged in a sandwich configuration, secured with clamps, and subjected to UV irradiation (UVP UVGL-55 254/365 nm, Analytik Jena) for the curing and sealing of the cells. The redox electrolyte solution was injected through 2 predrilled holes in the counter electrode and sealed using the same glue. FDSSCs using paste A were then assembled based on the optimal configuration identified from rigid devices.


Figure 44. AB Glue Dispensing MachineTBS-TC-441

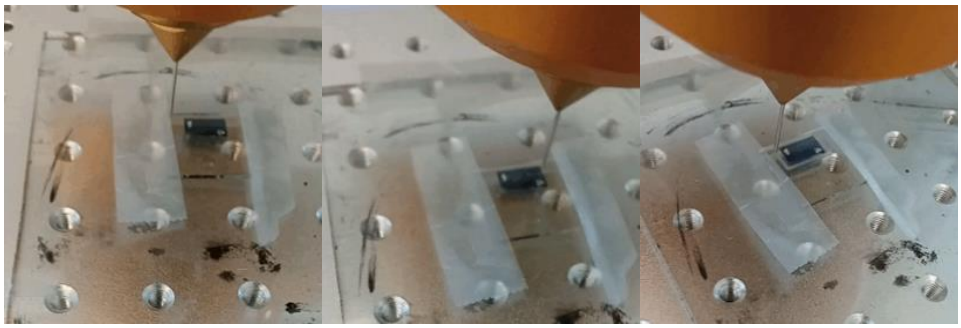

Figure 45. Fixed counter electrode on dispenser plate (left). Glue deposition around the PEDOT film (center and right).

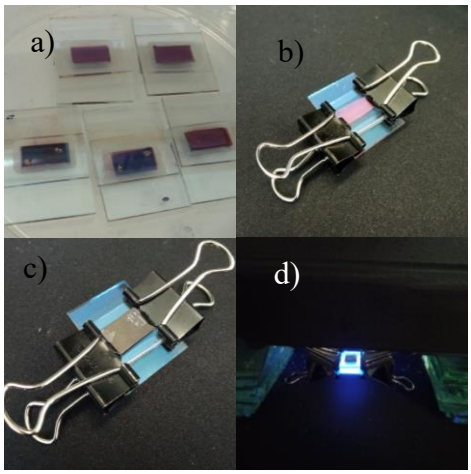


Figure 46. a) Photo and counter electrode placed in a sandwich configuration. b) Clamped photo and counter electrode thogeter. c) Aluminum foil with a black paper envelope placed over the active area to avoid UV-light to damage the dye. d) Device subjected to UV-light to cure the resin.

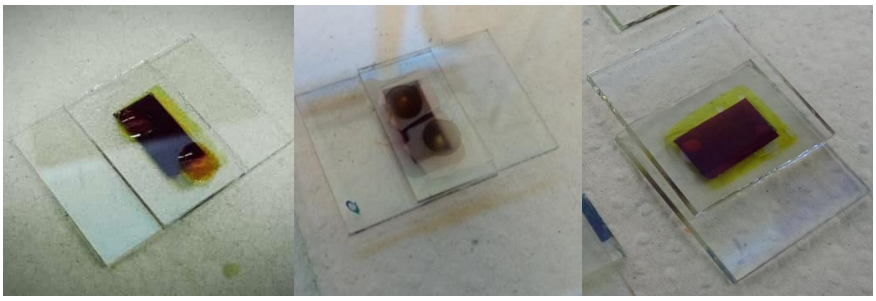

Figure 47. Electrolyte injected trhough the drilled holes (left). Holes sealed with glue after electrolyte injection (center). Sealed DSSC (right).

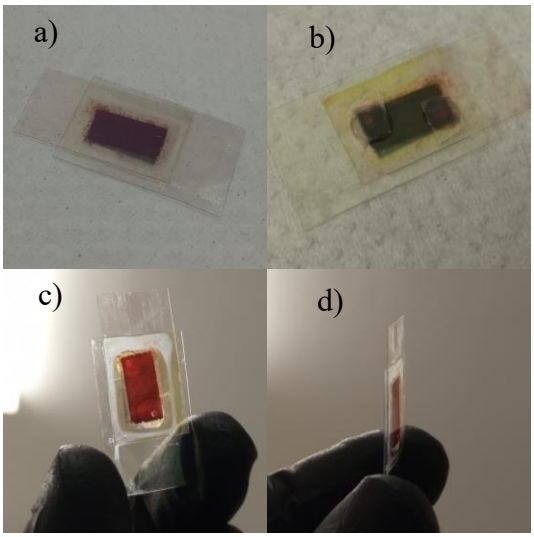


Figure 48. a) Flexible photo and counter electrodes placed in a sandwich configuration b) Electrolyte injected through the drilled holes and holes sealed with glue after electrolyte injection. c) and d) Sealed DSSC.

### 4.11.2. Assembly method 2

This assembly method was used for devices using paste B, C and D. Photoelectrodes were directly placed in contact with counter electrodes while pressed with clamps since, in addition to favorable charge transport characteristics, PEDOT provides selective extraction of p-type carriers, allowing for the direct contact of the counter electrode and the $TiO_2$ layer. For rigid

devices, glue in assembly method 1 was used. By minimizing the distance between electrodes it is possible to increases the device efficiency by increasing electron collection efficiency [186]. For flexible devices, an special UV-glue for plastics (Permabond UV639) was used to allow adherence and flexibility between plastic substrates. These glues were carefully applied on the edges around the electrodes leaving a small space opposite to the pre-drilled hole on the counter electrode (scheme or photos). This small gap allows for a better electrolyte injection and a homogeneous film wetting. The glue was cured using a 365 nm UV gun Thorlabs – CS Curing LED System 2010 for 5 seconds. The redox electrolytes for this devices were injected carefully throught this hole avoiding it to leak from the space left. Both, the hole and gap were then filled with glue and cured with the UV gun.


Figure 49. Thorlabs – CS Curing LED System 2010 (left). Permabond UV639 light curing adhesive (center). Threebond 3035B glue (right).

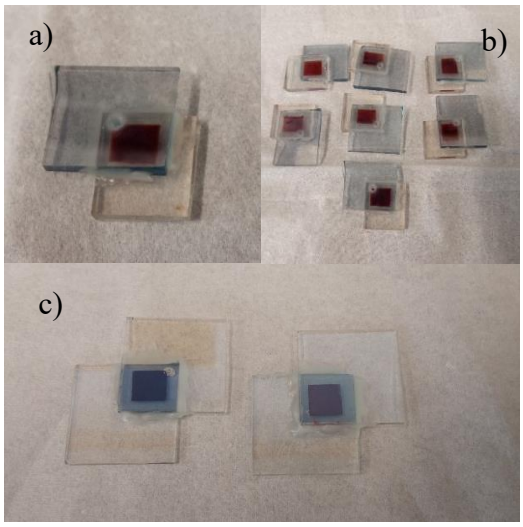


Figure 50. Assembled rigid devices using method 2. a) Closer look of cell assembled. b) Assembled DSSCs. c) Front and Back of assembled DSSC.

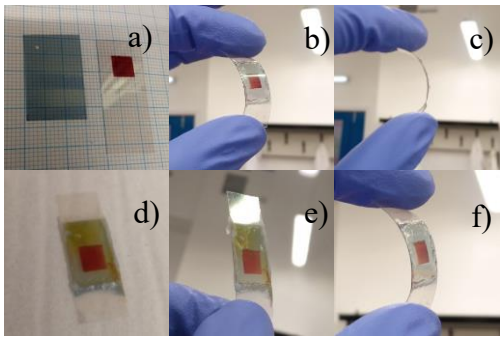


Figure 51. Assembled flexible devices using method 2. a) Flexible PEDOT counter electrode and flexible photo electrode. b) and c) Assembled device showing flexibility. d) and e) Injected electrolyte in flexible DSSC. f) Flexible DSSCs after electrolyte injection.

### 4.12. $TiO_2$ pastes for high performance DSSC.

In this section, the preparation of high-performance devices utilizing synthesized anatase and brookite powders is described.

### 4.12.1. Photo electrodes preparation

In this section, the procedure for the preparation of electrodes of high-performance DSSC Is described.

### 4.12.2. Washing

Flourine-dope doped tin oxide (FTO) with a sheet resistance of 10 Ω $sq^{-1}$ was used for the fabrication of high performance DSSCs. To prepare the photo electrodes, substrates were cut in 3 x 10 $cm^2$ bars. Then, they were washed using the same cleaning proccedure as section 4. Once the substrates are dried, they are immediately subjected to a UV-$O_3$ treatment for 30 minutes to further clean and increase FTO surface energy.

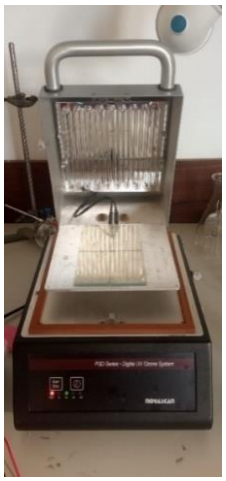

Figure 52. FTOs under 20 min UV-$O_3$ treatment.

### 4.12.3. Blocking layer

The blocking layer solution is prepared by mixing 9 mL of 2-propanol (anhydrous, 99.5%, Sigma-Aldrich), 0.6 mL of titanium diisopropoxide bis(acetylacetone) (Sigma-Aldrich) and 0.4 mL of acetyl acetone (Sigma-Aldrich) in a glove box under nitrogen and stored at 5°C.

Cleaned FTOs are then placed on a hot plate and the temperature is slowly increased until 450 °C is reached: 3 mL of this blocking layer solution is then sprayed onto 8 FTO slides by while the temperature is maintained at 450 °C until the solution is finished. Finally, the substrates are left 30 minutes at 450 °C.

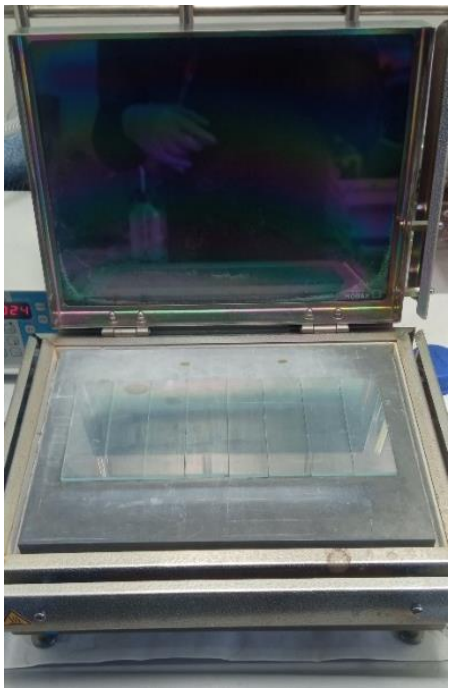

Figure 53. Spray pyrolysis deposition of blocking layer on FTOs.

### 4.12.4. High-temperature pastes

Two different methodologies were tested using anatase for the paste preparation to obtain high performance devices. The first paste, A-Synth, was prepared using anatase nanoparticles without drying to powder after the synthesis process and the second paste, A-Bmill, was prepared using dried powder and subsequent ballmilling process. In the following the procedure is described.

#### 4.12.4.1. A-Synth paste

Step 1) After the washing method (step e, Anatase synthesis section 4.1.) the dry/wet weight ratio techniqe is used (From paste C, section 4.19) in order to obtain 0.5g of $TiO_2$ in 10 mL of EtOH and left to stirr.

Step 2) In a separate 20 mL beaker, 0.15 g of ethyl cellulose (EC) is added in 10 mL of EtHO at 40 °C while stirring and once is fully dispersed, 4.1 g of α-terpineol is added and left to stirr. An ultrasound probe is used to further disperse the materials in the solution. This is done by applying 3 min of sonication and 3 min of stirring on a stirrging plate three times. After this, the solution is concentrated using a rotary evaporator to obtain a viscous paste.

#### 4.12.4.2. A-Bmill paste

This paste was prepared by dry ball-milling 1 g of $TiO_2$ powder in in a Retsch 50 mL agate jar with ten 10 mm diameter agate balls for 1 hour at 500 RPM. The wet milling was performed by adding 25 mL of EtOH, the program was set to run for 1 hour at 500 RPM and the jar was left to sabilize for 1 day. Then, the stable solution was carefully removed as in Paste B – Ball milling (section 4.16) leaving agglomarates particles at the bottom of the jar. These agglomarates are then dried and weighed in order to obtain the $TiO_2$ concentration in solution. 0.5 g of $TiO_2$ agglomerates were weighed. Ethanol from the solution is then slowly evaporated using a rotary evaporator in order to obtain a volume of 10 mL. From this point onwards, step 2) of A-Synth paste is followed to obtain a viscous paste.

#### 4.12.4.3. Brookite paste

This paste was prepared using $TiO_2$ brookite dry powders following the same methodology as A-Bmill paste.

Figure 54. Preparation process of high temperature pastes for DSSC.

### 4.12.5. Paste deposition and sintering

All high temperature pastes and commercial 30NR-D paste were deposited onto the blocking layer by manual screen-printing using a customized screen (Figure 55). Once a 4 μm film thickness is approximately obtained for the active layer, substrates were placed onto a hot plate at 120 °C in order to evaporate the excess of solvent in the pastes. Then a scattering layer is deposited on top of the active layer using a commercial WER2-0 paste to obtain additional 4 μm, for a total of 8 μm of film thickness and the solvent is again evaporated at 120 °C.


Figure 55. Manual screen-printing for the high-temperature pastes deposition (left) and solvent drying on a hot plate at 120 °C (right).

Then, sintering process is carried out. This is done by placing the FTOs on a hot plate and subject them to a temperature ramp from 25 °C to 500 °C, as depicted in Figure 56.

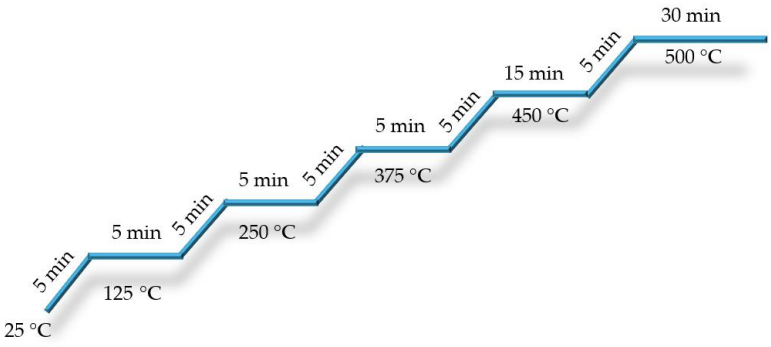


Figure 56. Temperature ramp for the sintering process.

After cooling down, substrates are immersed in a 13 mM aqueous $TiCl_4$ solution and this container is placed in a furnace oven at 70 °C for 30 minutes. Then, the substrates are thoroughly rinsed with DIW and dried using an air gun. The 3 x 10 $cm^2$ FTO slides are then carefully cut to 1.5 x 1.43 $cm^2$ individual cells and again cleaned using the air gun to remove possible undesired small pieces of glass on the top of the films. Finally, these cells are placed on a hot plate and subjected to a second sintering process using the same ramp as before.

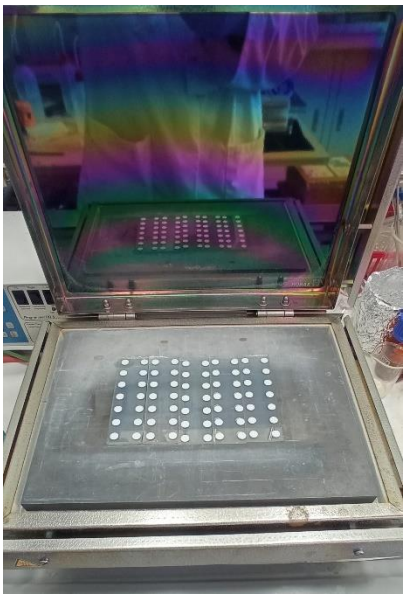

*Figure 57. Films sintering on a hot plate.*

### 4.12.6. Dye-sensitization

Cell were immersed in D2 dye at 150 °C  in a room temperature bath for film sensitization and left there for 24 hours. After this time, the cells are thoroughly rinsed using acetonitrile and dried using an air gun.

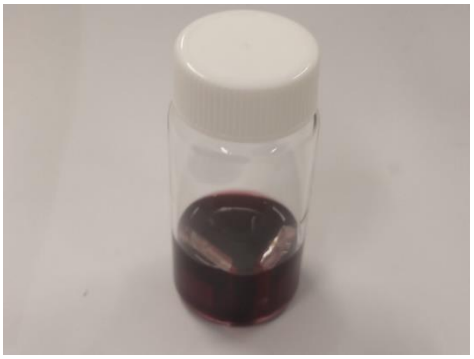

*Figure 58. Dye-sensitization of high-temperature films.*

### 4.12.7. Counter electrode preparation

Counter electrodes for the high-performance DSSC follow a similar procedure for the preparation with the difference in the type of substrate used, the size of them and the experimental parameters. For the counter electrodes, same solution as the one used for low-temperature devices was utilized. Electropolymerization of poly(3,4-ethylenedioxythiophene) (PEDOT) on the conductive substrates was performed by using a Gamry potentiostat using a two-electrode configuration and applying a fixed current of 13 mA for 25 s. Perforated 6.8 x 5.5 $cm^2$ FTOs with a sheet resistance of 7 Ω $sq^{-1}$ were used as the working electrode and a 16.5 x 10 $cm^2$ 7 Ω $sq^{-1}$ FTO was used as the counter electrode. After the PEDOT deposition, counter electrodes were thoroughly rinsed with EtOH and dried using an air gun. Finally, 6.8 x 5.5 $cm^2$ FTOs were carefully cut in 1.7 x 1.85 $cm^2$ individual cells and cleaned again with an air gun.

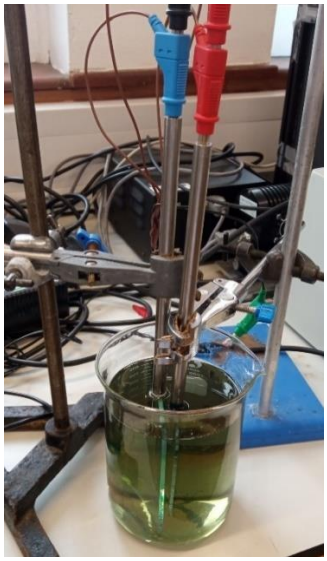

Figure 59. PEDOT deposition on FTOs.

### 4.12.8. Cell assembly

The assembly method used for this devices is the same as described in assembly method 2 using Threebond 3035 glue as the UV-curable resin to attach photo and counter electrodes. The electrolyte injected in these cells was the Cu electrolyte. Finally, a layer of tin is soldered to the conductive area on the cathode and anode to improve electrical contact of devices.

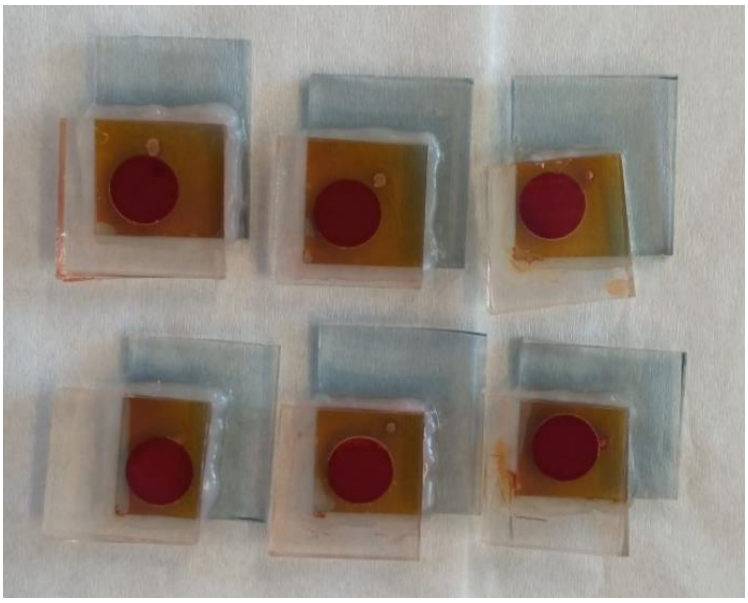

Figure 60. High-performance DSSCs.

# RESULTS

## 5. $TiO_2$ structural characterization

In this section, the structural characterizations of the three crystalline phases of $TiO_2$ are described.

### 5.1. $TiO_2$ powder X-ray diffraction.

A Bruker D8 ADVANCE X-ray diffractometer was utilized to analyze the structural properties of the prepared $TiO_2$ nanomaterials in 3 different phases (anatase, rutile and brookite). As depicted in Figure 61, the XRD peaks of the synthesized $TiO_2$ align with the characteristic features of the anatase phase (tetragonal, JCPDS # 21-1272, $a = b = 3.78$ Å, $c = 9.51$ Å, $\alpha = \beta = \gamma = 90°$) at 2θ values of 25.37°, 37.89°, 48.12°, and 55.06°, which are ascribed to (101), (004), (200), and (105) Miller indices, respectively. Rutile phase (tetragonal, JPCDS # 87-0710, $a = b = 4.58$ Å, $c = 2.95$ Å, $\alpha = \beta = \gamma = 90°$) major diffraction peaks at 2θ values of 27.3°, 36.1°, 41.2° and 54.1° are ascribed to (110), (101), (111), and (211) Miller indices, respectively. Brookite is characterized by a (121) peak at 30.80°, which is not found for either anatase or rutile (orthorombic, JCPDS # 29-1360, $a = 9.09$ Å , $b = 5.39$ Å). The two other main peaks, the (120) peak at 25.33° and the (111) peak at 25.68°, overlap because of the nanoparticulate character of the powder, resulting in peak broadening. In addition, these peaks are at essentially the same angle as the main anatase (101) peak at 25.28°. The determination of the crystallite size (d) from the $TiO_2$ anatase diffractogram was carried out using equation 33 of the Debye–Scherrer method.

$$d = \frac{k\lambda}{\beta cos\theta} \tag{33}$$

where λ is the wavelength of the X-ray (1.5406 Å), β is the full width at half-maximum (FWHM) of the diffraction peak, θ is the diffraction angle, and k is a constant. A particle size of 21 nm was obtained using the peak at 48° of anatase powder and an average of 45 nm using the peak at 32° for brookite powder. Rutile size was measured using SEM micrographs.

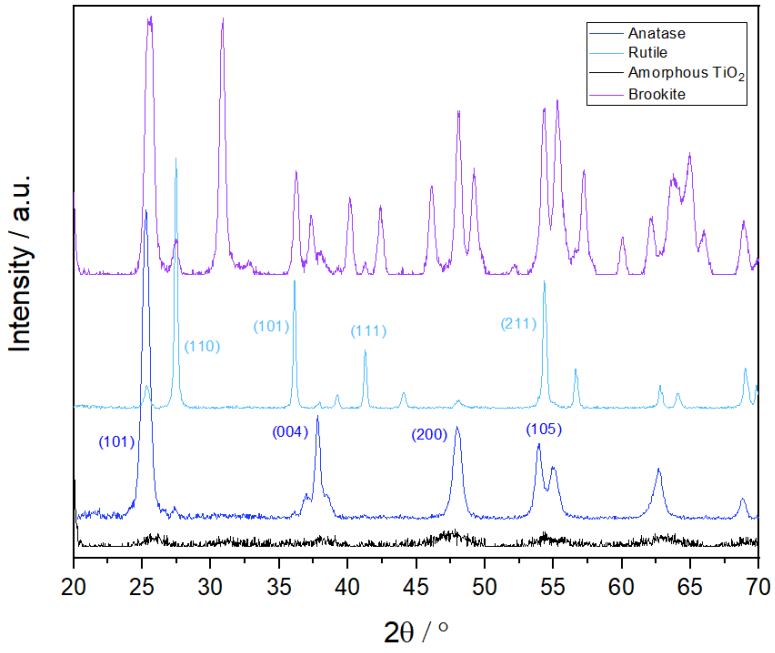


Figure 61. XRD diffraction pattern of synthesized $TiO_2$ powder showing characteristic anatase and rutile peaks in agreement with JCPDS # 21-1272 and # 87-0710 cards.

## 5.2. Fourier-Transform Infrared Spectroscopy

A light yellowish powder was obtained after fine grinding of the $TiO_2$ anatase and rutile nanoparticles in a mortar (Figure 65, a)). This is indicative that some organic compounds may still be present.

Two different treatments were used to try to remove the highest amount of undesired organic compounds and to try to retain as many -OH groups as possible on the surface, responsible for anchoring the dye molecules. The two treatments consisted of UV-$O_3$ exposure of the powders for different durations and a thermal treatment at 500 °C.

The analysis of molecular absorption and identification of functional groups on the synthesized $TiO_2$ surface were conducted using an Agilent Cary 630 FTIR spectrometer. In Figure 62 (green), the FTIR spectrum of commercial P25 $TiO_2$ without further modification exhibits a typical absorption band at 450–615 $cm^{-1}$, indicative of Ti-O metal oxide bonding. A consistent functional group is observed across all samples at 3000–3600 $cm^{-1}$, attributed to the presence of hydroxyl moieties (O-H). Additionally, the absorption band at 1620 $cm^{-1}$ corresponds to the bending vibration of Ti-OH bonds.

Figure 62 (black) displays the FTIR spectrum of synthesized air dried $TiO_2$ anatase nanoparticles without post-cleaning treatment. Absorption bands between 1300 and 2150 $cm^{-1}$ suggest the presence of organic material on the $TiO_2$ nanoparticle surface indicating an incomplete reaction during the sol–gel process, where nitrogen from nitric acid remains

attached to the particle surface post-cleaning. Bands at 1450 and 1530 $cm^{-1}$ are associated with the symmetric and asymmetric stretching of carboxylate groups (-COOH), respectively.

In the case of the thermal treatment, for all 3 crystalline phases, it can be observed that practically all signals disappear. This means that the thermal treatment is capable of completely eliminating organic components on the surface. However, the presence of -OH groups on the surface is also diminished, which could potentially have a negative effect on dye molecule adsorption.

For the UV-$O_3$ treatment, a Novascan PSD Series Digital UV Ozone System was used. The powders of amorphous, anatase, and rutile $TiO_2$ were subjected to different exposure times: 2, 3.5, and 5.5 hours. Brookite powders were subjected to 5.5 hours of exposure. As can be observed in the anatase spectrum, as the time increases, the signals of organic compounds on the surface begin to decrease until a clean surface is finally obtained. In the case of rutile, the same occurs, but additionally, it can be observed that -OH groups also begin to form on the surface, indicating that the treatment is capable of creating bonds on this crystalline phase. In the case of brookite, a decrease in organic compounds is not observed, but an increase in -OH groups on the surface can be observed.

In the Figure 65 b) to d), the yellowish color of the synthesized anatase particles after air drying following powder washing can be observed, as well as how the color changes to white after both temperature and UV-$O_3$ treatments.

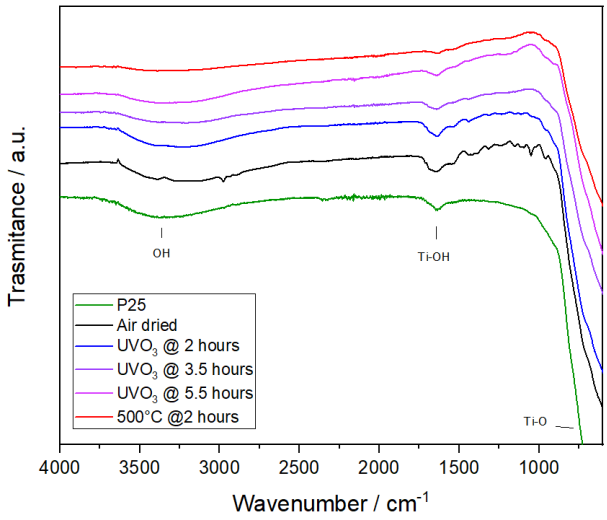


Figure 62. FTIR spectra of commercial P25 (green), synthesized $TiO_2$ anatase powder after air drying (black), synthesized $TiO_2$ anatase powder after 2 hours (blue), 3.5 hours (purple), 5.5 hours (pink) of UV-$O_3$ treatment and synthesized $TiO_2$ anatase powder after heat treatment (red).

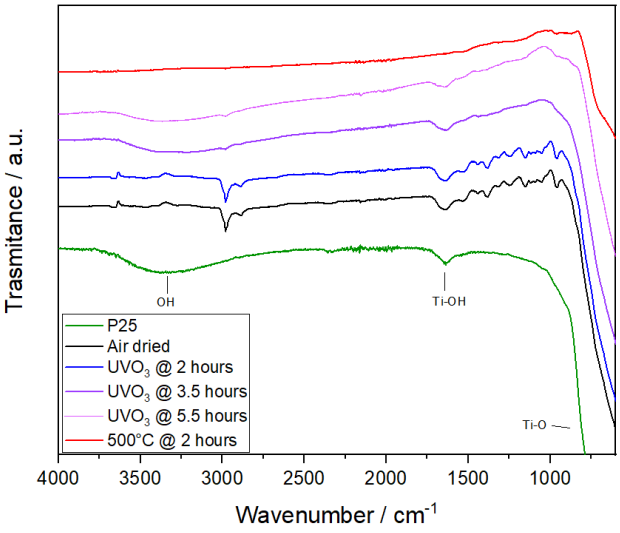


Figure 63. FT-IR spectra of commercial P25 (green), synthesized $TiO_2$ rutile powder after air drying (black), synthesized $TiO_2$ rutile powder after 2 hours (blue), 3.5 hours (purple), 5.5 hours (pink) of UV-$O_3$ treatment and synthesized $TiO_2$ anatase powder after heat treatment (red).

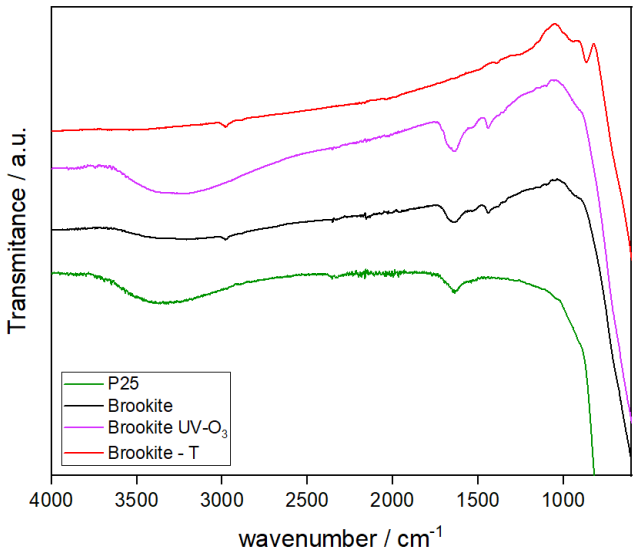


Figure 64. FT-IR spectra of commercial P25 (green), synthesized $TiO_2$ brookite powder after air drying (black), after UV-$O_3$ treatment (pink) and after heat treatment (red).

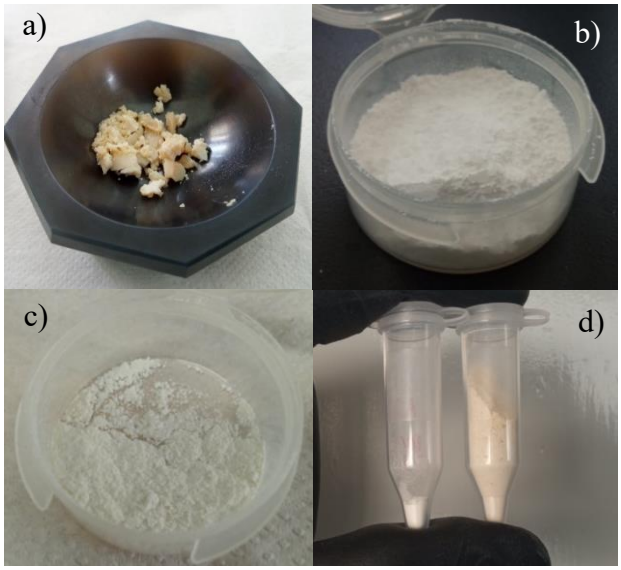


Figure 65. a) Yellowish $TiO_2$ anatase powder after air drying. b) white $TiO_2$ anatase powder after heat treatment. c) white $TiO_2$ anatase powder after UV treatment. d) Color comparison between $TiO_2$ anatase powder after heat treatment (white, left) and before (yellowish, right).

### 5.3. Scanning electron micrographs of synthesized $TiO_2$ powders

To observe and evaluate the morphology of the 3 crystalline phases of $TiO_2$ nanoparticles and a JEOL JSM-7600F field emission scanning electron microscope was used at CINVESTAV-Merida. Numerous micrographs of $TiO_2$ powders acquired from diverse locations allowing for a precise estimation of particle size. Subsequently, statistical analysis was conducted employing captured micrographs and the ImageJ processing program to ascertain the average particle size.

#### 5.3.1. Anatase

Figure 66 show the morphological characteristics of the anatase powders, where a typical spherical shape can be observed. It can be seen that the particle size is distributed in a range between 14 and 30 nm, and that some small particle agglomerates can also be observed, which may have a size of up to 50 nm. In Figure 66 e), it can be observed that upon drying the powder, massive particle agglomerates of around 1.4 μm are also formed.

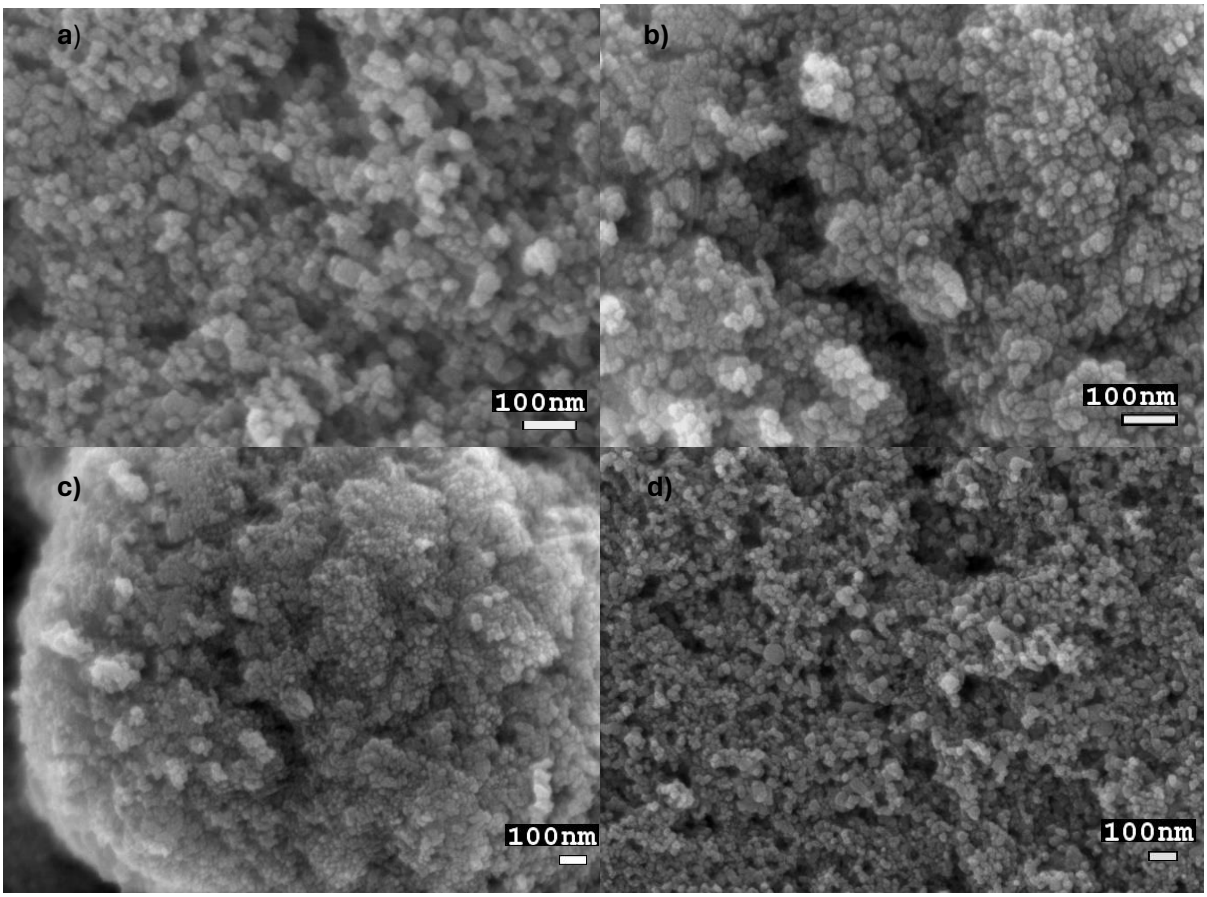


Figure 66. SEM image of anatase powder at 10 KV and a) and b) 100,000 X and c) and d) 50,000 X.

### 5.3.2. Rutile

The Figure 67 and 50 show the morphological characteristics of the rutile powders, where a typical elongated shape can be observed. According to these images, it can be estimated that the average size of these particles is 200 x 80 nm. Similar to anatase, the rutile powder also forms massive agglomerates upon drying (Figure 67, d) and e)).

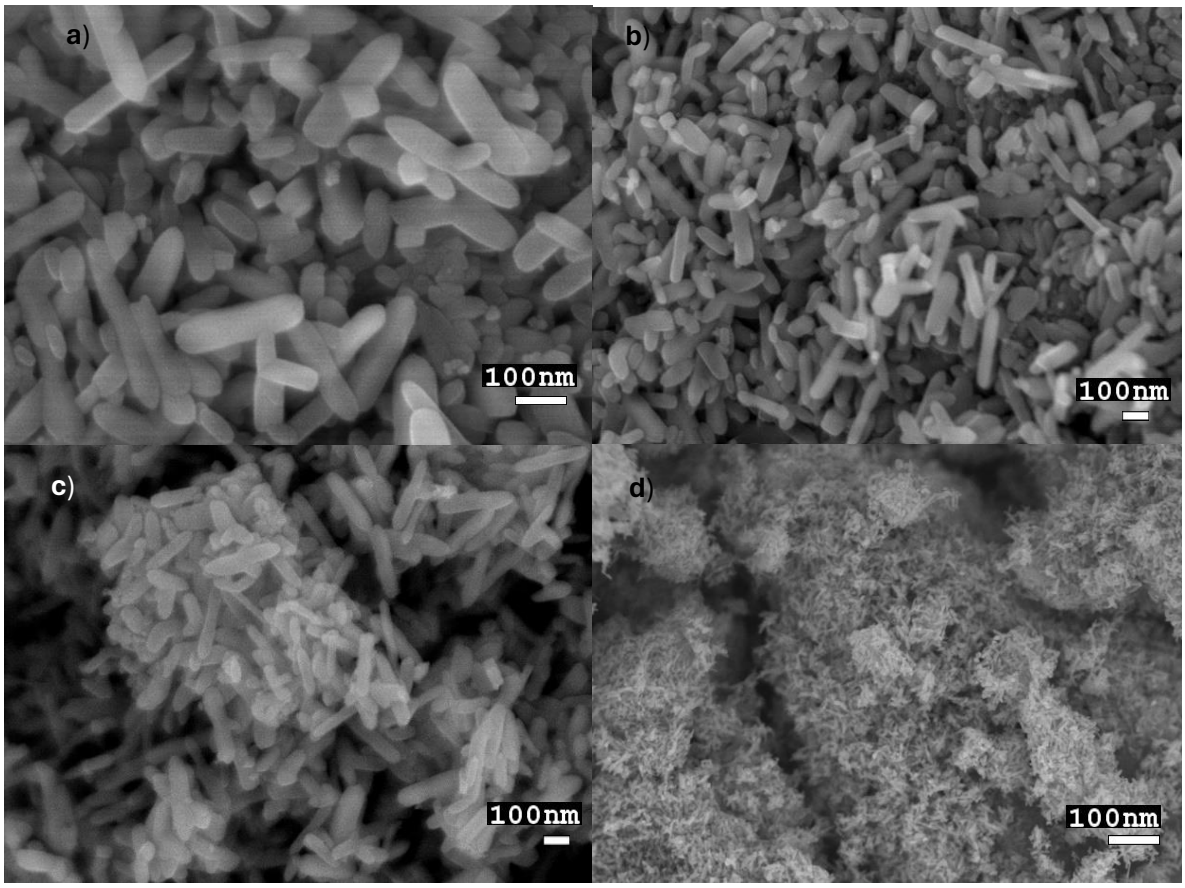


Figure 67. SEM image of rutile powder at 10 KV and a) 100,000 X, b) and c) 50,000 X and d) 10,000 X.

### 5.3.3. Brookite

Figure 68 show the morphological characteristics of the brookite powders, where a shape that is not entirely spherical, as presented by the crystalline phase anatase, can be observed. These exhibit a morphology resembling a slightly elongated cube, and the particle size presents a distribution ranging between 30 and 60 nm. Additionally, particle agglomerates of approximately 200 nm can be observed. Furthermore, similar to the previous crystalline

phases, it can be observed that upon drying the powder, massive agglomerates of approximately 1.6 μm are also formed.

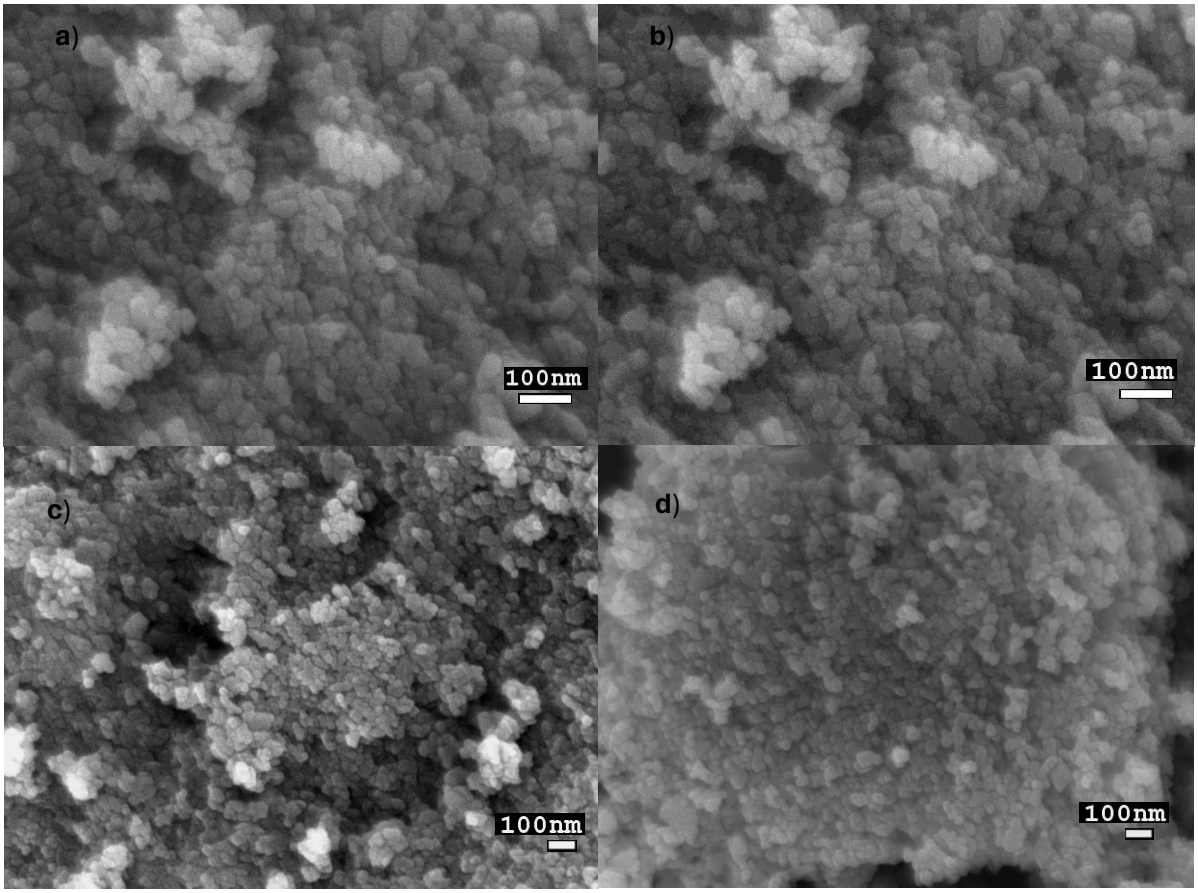


Figure 68. SEM image of brookite powder at 10 KV at a) and b) 100,000 X and c) and d) 50,000 X.

### 5.3.4. Anatase:Rutile mixture

In Figure 69, SEM images of a mixture of anatase and rutile powders in a ratio of 80:20, respectively, used for low-temperature pastes, are shown. Elongated shapes corresponding to the rutile crystalline phase can be observed. Similarly, large agglomerates can also be seen.

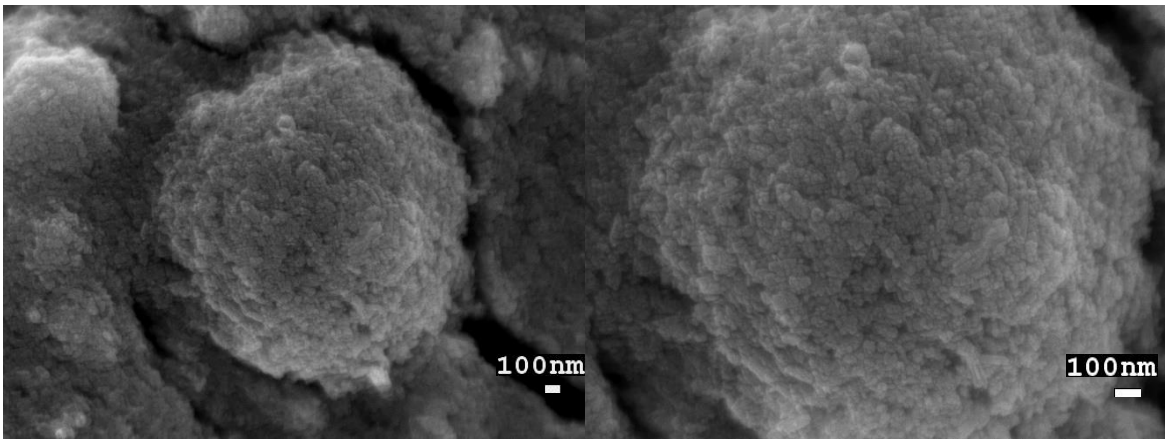


Figure 69. SEM image of mixed antase:rutile powders at 10 KV and 30,000 X (left) and 50,000 X (right).

### 5.4. Low-temperature DSSCs

In this section, the characterizaion of the films deposited using pastes A-C and the PV characterization of rigid and flexible DSSCs are described.

#### 5.4.1. Scanning electron microscopy of films.

Morphology and thickness of films deposited using paste A were taken using a JEOL JSM-7600F field emission scanning electron microscope at CINVESTAV-Merida and films deposited using paste B and C were taken using a JEOL-JSM-5610LV scanning electron microscope at Newcastle University. Numerous micrographs of the topography and cross-

section of these films were acquired from diverse locations. Allowing for a precise estimation of film thickness.

#### 5.4.1.1. Paste A film.

For devices fabricated with paste A, Figure 70 depicts the nanostructured, mesoporous $TiO_2$ films fabricated on ITO-Glass through the low-temperature treatment. The closely spaced particles suggest effective interparticle bonding. However, it can be observed in Figure 70 a) and b) that there are massive agglomerates of around 5 μm on the surface. The surface is not entirely homogeneous; it can be seen that the agglomerates cause irregularities on the surface, resulting in micro-cracks. Furthermore, in Figure 70 c) and d), with a more distant view, macro-cracks and massive agglomerates can be observed. It can also be seen in Figure 70 d), how the action of the applied temperature is too aggressive, causing water evaporation and potentially leading to crater formations.

In Figure 71 It can be observed that the thickness of the film is not uniform across all areas, as there are variations ranging from 6.4 to 9 μm. Inside the film, the presence of these large agglomerates can be observed, producing large volumes of pores and reducing the effective surface area of the film fFigure 71 d)). Due to this increased pore volume, large areas of the film are not in contact with the ITO conductor surface, further compromising electronic transport. It can even be observed that there are cracks extending from the surface to the ITO film.

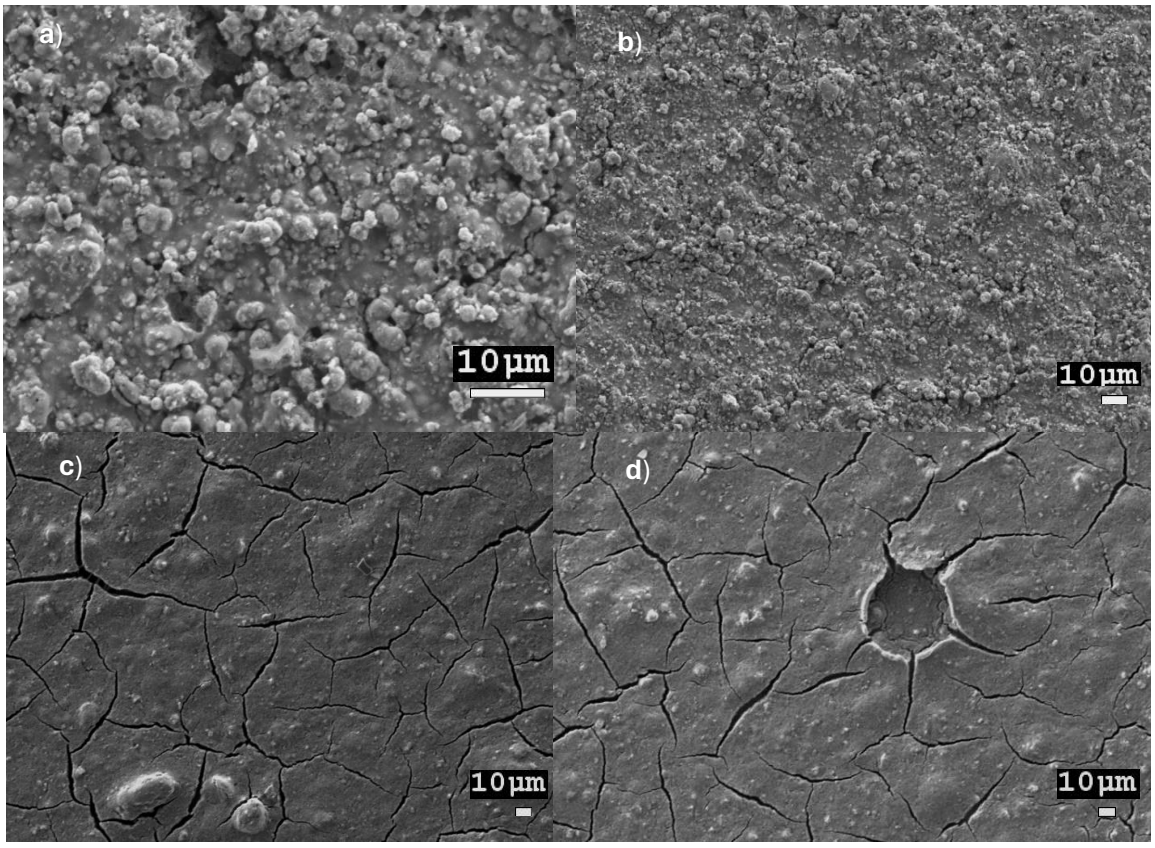


Figure 70. SEM image of paste A film non-uniform topography on ITO-Glass at 10 KV and a) 1,500 X, b) 500 X and c) and d) 300 X.

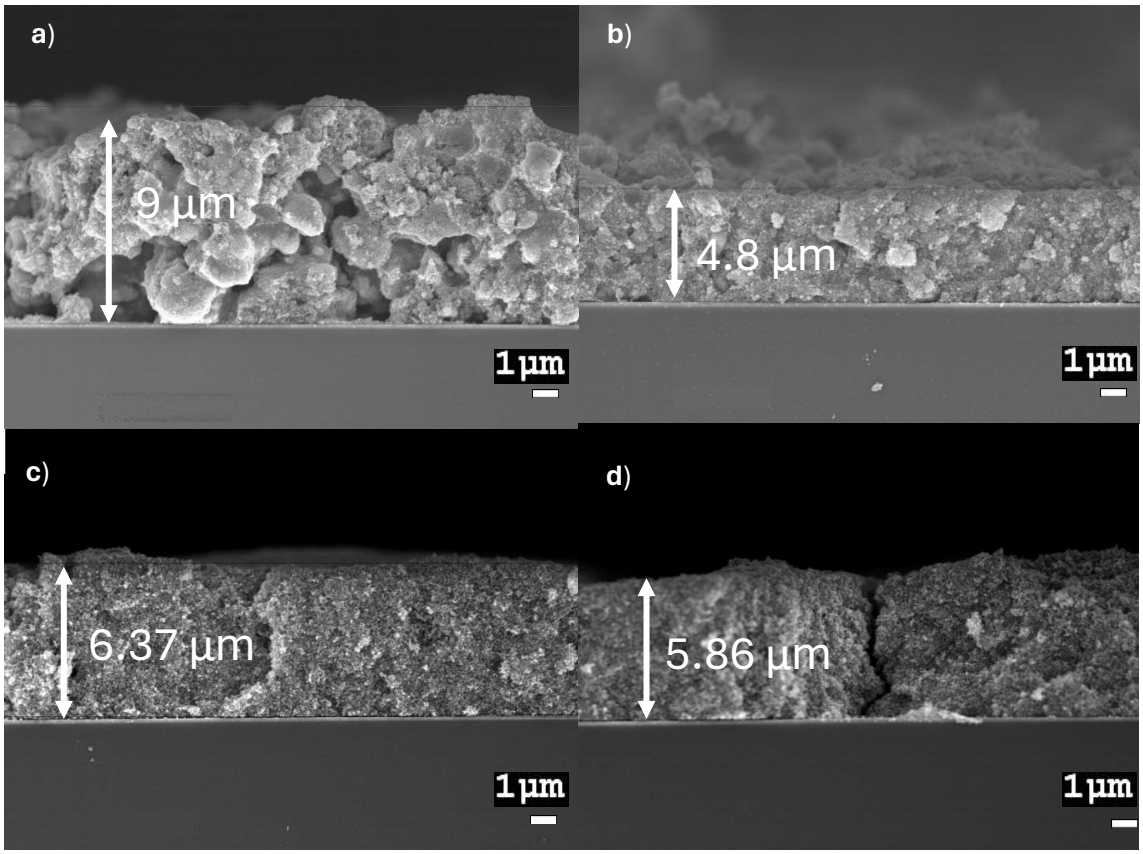


Figure 71. SEM image of paste A film cross-section on ITO-Glass at 10 KV and 5,000 X of a) of 9 µm showing large agglomerates, b) 4.8 µm, c) 6.37 µm and d) 5.86 µm showing a large crack.

**5.4.1.2. Paste B film.**

For devices fabricated with paste B (ball-milled anatase:rutile, 80:20, w:w, powders after airdrying and UV-$O_3$ treatment) Figure 72 depicts the nanostructured, mesoporous $TiO_2$ films fabricated on ITO-Glass through the low-temperature treatment using the ball milling method to break the agglomerates in the paste. In this case, it can be observed in Figure 72 d), that the film is more homogeneous than the film of paste A, as there is a lower amount of

irregularity on the surface. Some micro-cracks are still visible, however, in fewer quantities than those found in film A. Although the quantity and size of agglomerates are smaller compared to paste A, they can still be observed. In Figure 72 a), the distribution of macro-cracks appears to be similar to those found in the paste A film but the surface is less rough.

Figure 72 d), shows a wide view of the deposited film where it can be observed that with this paste, a more homogeneous film was obtained throughout the deposition. It is observed that the thickness of the film was 6.26 μm. Despite reducing the amount of large agglomerates in this paste, it can be seen that macro-cracks persisting from the surface of the film to the surface of the ITO are still present.

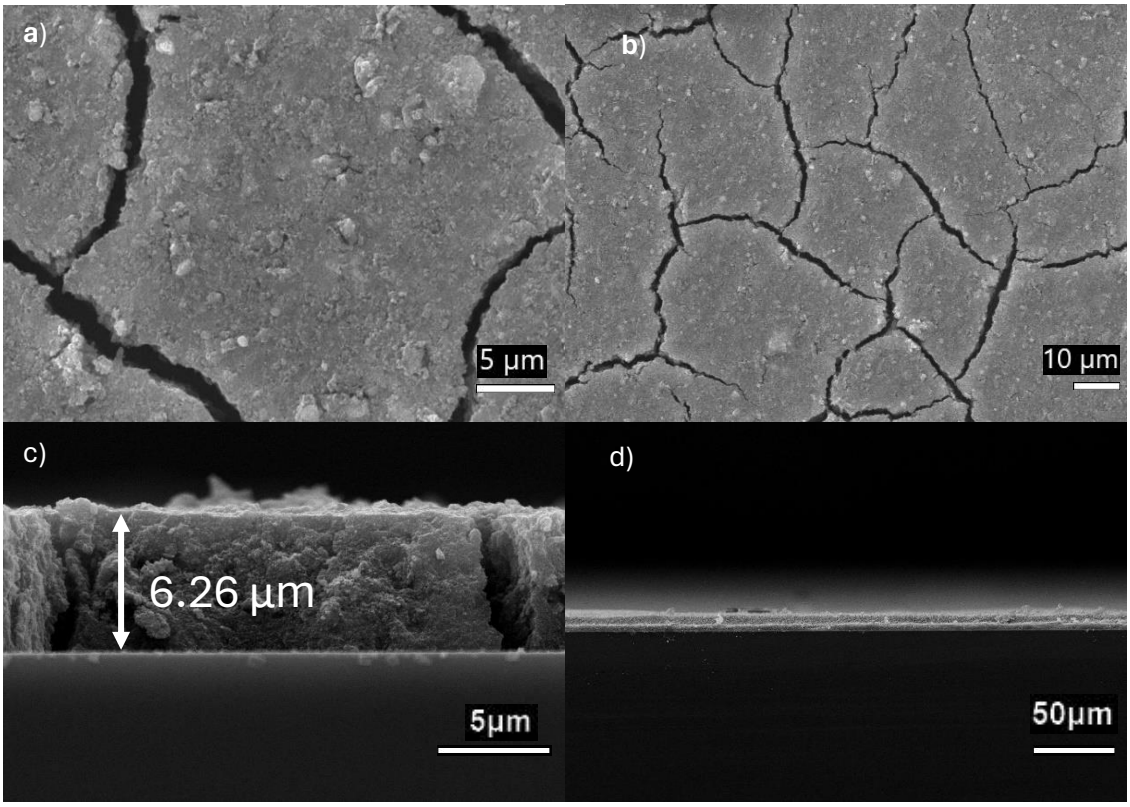


Figure 72. SEM image of paste B film topography on ITO-Glass at 20 KV and a) 3,500 X, b) 1,000 X showing macroscopic cracks and some agglomerates, c) 5,000 X and d) 350 X show a cross-section on ITO-Glass showing a more compact and homogeneous film.

### 5.4.1.3. Paste C film

For devices fabricated with paste C (prepared using the $TiO_2$ anatase and rutile particles directly after the synthesis washing process) on ITO-Glass Figure 73 a), depicts the nanostructured, mesoporous $TiO_2$ films fabricated using $TiO_2$ from synthesis. It can be observed that in this case, the deposited film is homogeneous and practically free of agglomerates compared to pastes A and B, and the presence of micro-cracks is negligible. In Figure 73 b), it can be seen that the distribution of macro-cracks is significantly reduced.

In Figure 73 c) amd d), it can be observed that the deposition is homogeneous along the ITO, demonstrating a thickness between 1.6 – 1.7 µm. In this case, the disappearance of macro-cracks from the surface of the films upon contact with ITO can be observed. It can also be seen that the film is much more compact than the one produced with pastes A and B.

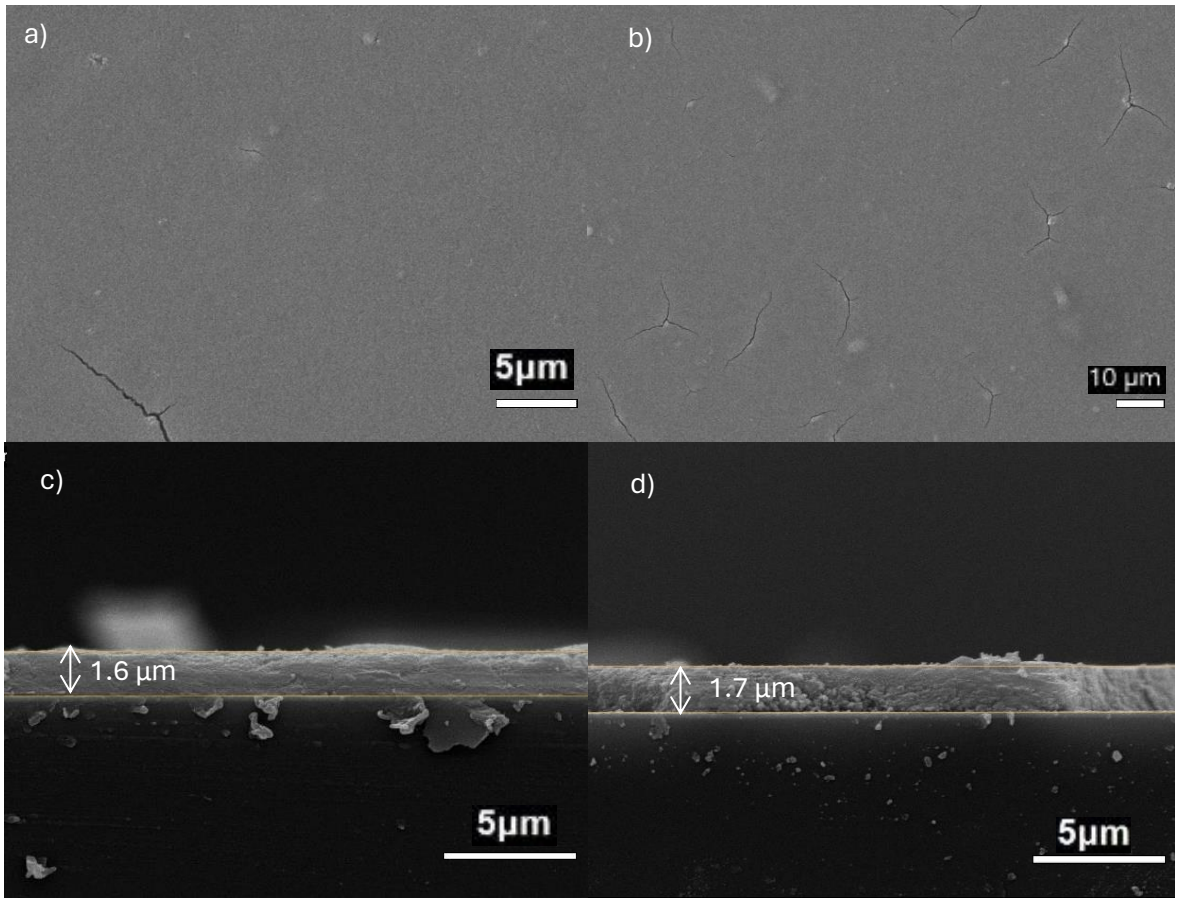


Figure 73. SEM image of paste C film topography on ITO-Glass at 20 KV and a) 3,500 X, b) 1,000 X, c) and d) 5,000 X

### 5.4.2. Counter electrodes

Figure 74 presents SEM images of the ITO-Glass counter electrodes catalyzed through electropolymerized PEDOT. The deposition process leads to the formation of a granular structure, significantly increasing the surface roughness and consequently fostering improved electrocatalytic performance. In Figure 74 a) to c), it can be observed how the deposition of PEDOT is homogeneous as no areas without deposition are visible. Figure 74 d) confirms an average thickness of around 80 nm.

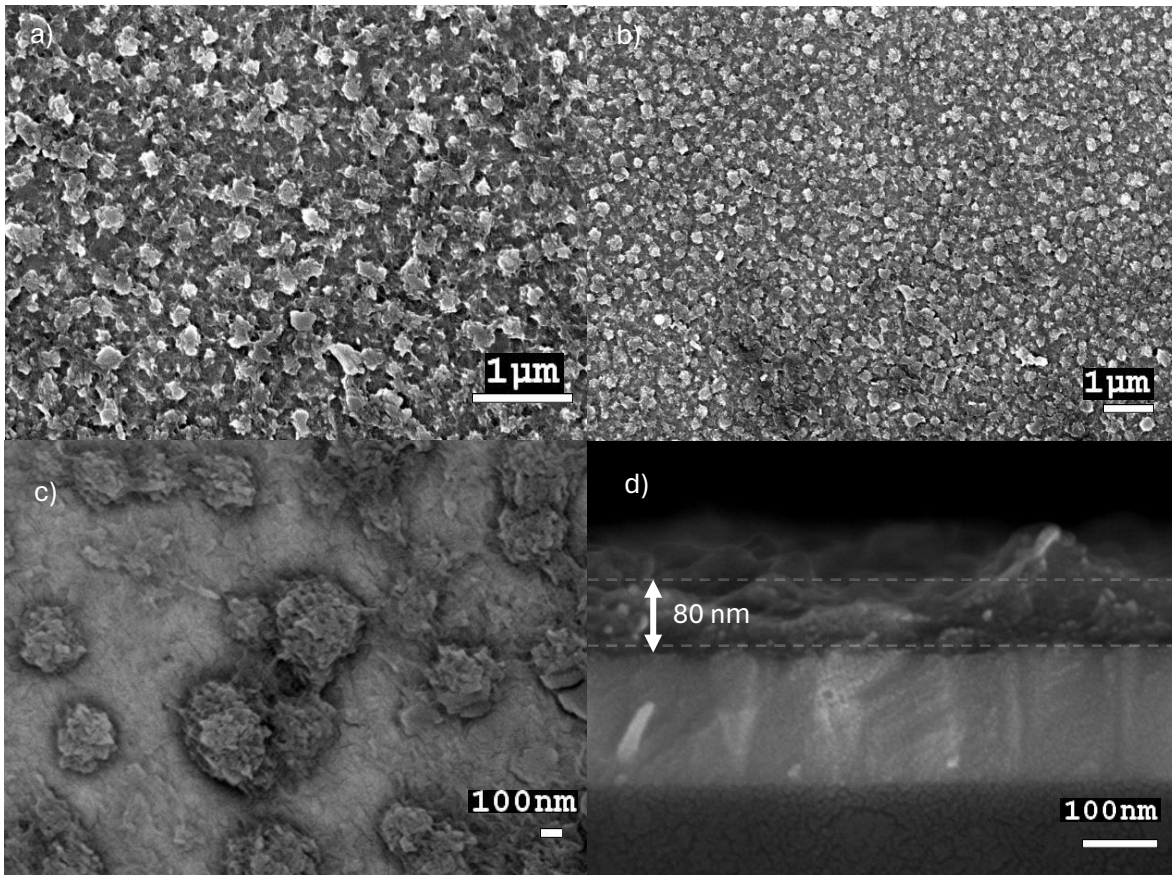


Figure 74. SEM image of PEDOT film topography on ITO-Glass at 5 KV and a) 20,000 X, b) 10,000 X, c) 40,000 X and d) 150,000 X.

### 5.4.3. Rheological measurements of paste C

Paste C underwent rheological testing using a rheometer at 25°C. Figure 75 shows the behavior of paste C compared to commercial paste 30NR-D. It can be observed how the viscosity of paste C and the commercial paste vary as a function of shear stress. The behavior of paste C is typical of a non-Newtonian fluid as viscosity changes with increasing shear

stress. Both pastes exhibit pseudoplastic behavior in which viscosity decreases as shear stress increases.

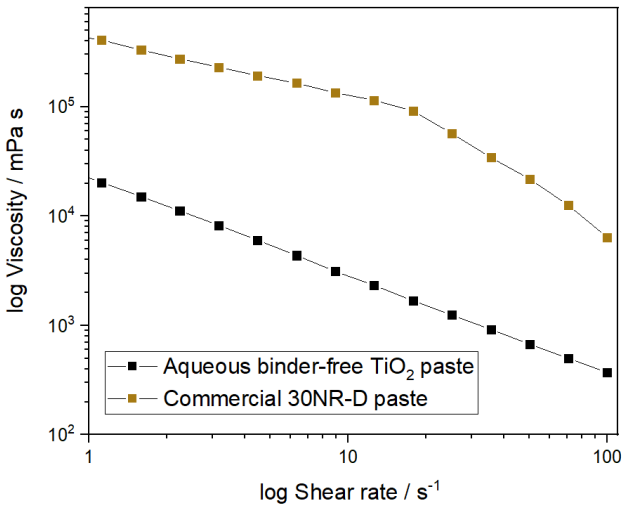


Figure 75. Viscosity behaviour of paste C (yellow) and commercial 30NR-D paste (black) at 25 °C.

### 5.4.4. UV-Vis spectroscopy

Transmittance tests were conducted on films made with pastes A, B, and C deposited on ITO-Glass using an Agilent 8453 UV-Vis equipment. In Figure 76, the transmittance on ITO-Glass substrates without film deposition (black line), with a film deposited from paste A (green line), paste B (red line), and paste C (blue line) is observed. It can be seen that the transmittance of ITO-Glass is approximately 85% in the 600 to 800 nm region, while in the 370 to 550 nm region, it has an absorption peak with transmittance reaching a minimum of approximately 80% around 480 nm and begins to decrease from 370 nm to reach a transmittance of 0% below 300 nm.

In the case of paste A, it can be observed that the transmittance is low, ranging from 37% at 800 nm to 18% at 410 nm, and then dropping to 0% below 400 nm. For paste B, it is noted that the transmittance is higher compared to paste A, starting just above 50% at 800 nm and decreasing to a value of 45% at 410 nm before dropping to 0% below 400 nm. Paste C demonstrates the highest transmittance of the three pastes, starting with a value of 77% at 800 nm and beginning to decrease below 500 nm to reach a value of 70% at 400 nm and subsequently dropping to 0% below 400 nm. In Figure 77, the visual difference between the transparency of the film deposited with paste A (left) and paste C (right) against a black background can be observed.

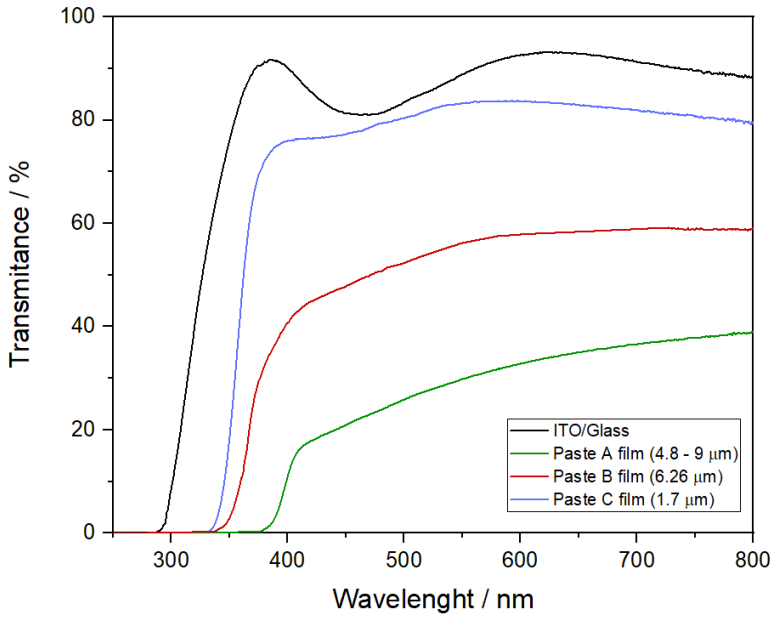


Figure 76. Transmitance sprectra of bare ITO glass (black) and films on ITO-Gass; Paste A film (green), paste B film (red) and paste C film (blue).

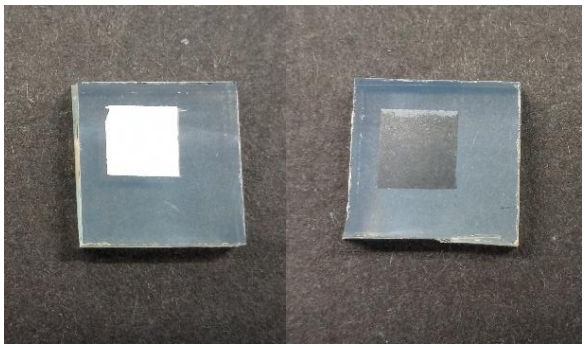

Figure 77. Visual transparency comparison between paste C film (left, 6.4 to 9 μm film thickness) and paste A (right, 1.6 – 1.7 μm film thickness) deposited on ITO-Glass.

### 5.4.5. Dye desorption

The desorption tests of Y123 dye on films deposited with paste C were conducted as follows: a) Small drops of Tetrabutylammonium hydroxide (0.1 M in methanol, Sigma Aldrich) were placed over the sensitized film. b) Then, the film with the base drop was rinsed using 3 mL of dichloromethane (DCM) (99.8% HPLC grade, Sigma-Aldrich), and the solvent was recovered in a 5 mL glass container. This method was performed on films prepared using paste C with and without the addition of TIIP to observe the effect of this solution on sensitization. The recovered solutions were analyzed using a UV-Vis Agilent 8453 with 3 mL of DMC as a blank solution. In Figure 78, the absorbance of the dye desorbed on these films is presented. We can observe how the dye loading in the films with TIIP is higher than in those without it. Based on these results, I decided to use the paste with TIIP to fabricate devices.

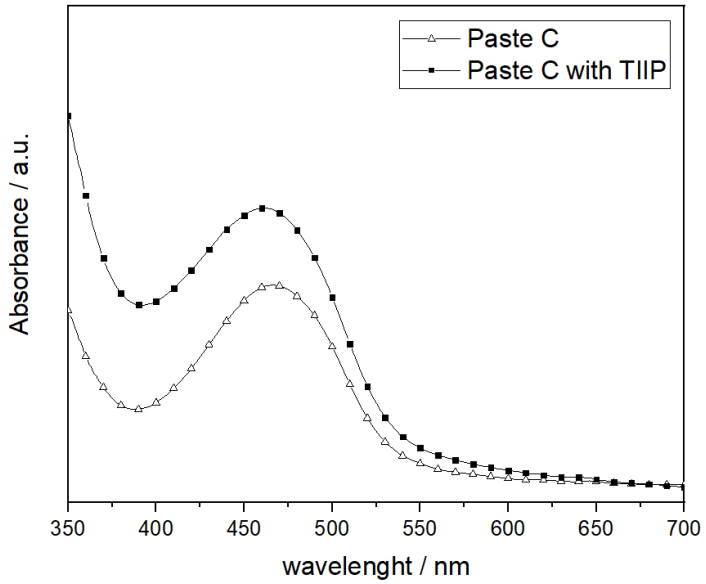


Figure 78. Y123 dye-sensitized paste C film (cwhite triangles) and paste D films (black squares) adsorption spectra. Spectra from Paste C with TIIP was displaced downwards to match Paste C at 700 nm for a more accurate comparison.

### 5.4.6. PV characterization and J-V curves for rigid and F-DSSC fabricated with paste A

These devices were fabricated using paste A, which is the paste prepared using air dried $TiO_2$ anatase nanoparticles with a UV-$O_3$ powder cleaning treatment. Assembly method 1 was sued as the low-temperature fabrication method for these devices. For measurements under 1-sun illumination, a 450 W ozone-free Xe lamp (Oriel) equipped with a 10 cm water filter and an AM 1.5G optical filter was utilized. Low light intensity measurements at 1000 lux (5600 K) were conducted using a Getlabs (Mexico) LED-based indoor lighting simulator. Photovoltaic (PV) parameters of devices constructed on ITO-coated glass employing

ACN:VN, VN:ACN, and MN electrolyte configurations are presented in Table 3 to 5, respectively. Each configuration produced five devices, designated as 1 to 5.

The devices made using ACN:VN-coated glass with ITO coating showed the highest FF and $V_{OC}$, measuring 0.59 and 0.76 V, respectively (Device 2 in Table 3). On the other hand, VN:ACN had the greatest $J_{SC}$, measuring 6.94 mA $cm^{-2}$ (Device 3 in Table 4). VN:ACN devices registered the highest power conversion efficiency at 2.62% (Device 3 in Table 4). This arrangement was used to fabricate FDSSCs due to its higher efficiency.

PV parameters, for five FDSSCs labeled as 1 to 5, manufactured on ITO-coated PEN with the optimal configuration, are detailed in Table 6. The most efficient device in this set exhibited a $J_{SC}$ of 2.81 mA $cm^{-2}$, $V_{OC}$ of 0.66 V, and FF of 0.52, resulting in an efficiency of 1% (Device 2 in Table 6). Table 6 provides a comparative analysis of the average and SD values for all devices measured under 1-sun conditions.

Table 3. Current density vs. voltage (J–V) data for DSSC devices fabricated on ITO-coated glass using ACN:VN (85:15 acetonitrile/valeronitrile) electrolyte configuration under 100 mW $cm^{-2}$.

| **ACN:VN Device** | **$V_{OC}$/V** | **$J_{SC}$/mA $cm^{-2}$** | **FF** | **η/%** |
|---|---|---|---|---|
| **1** | 0.76 | 4.30 | 0.59 | 1.94 |
| **2** | 0.76 | 4.36 | 0.59 | 1.97 |
| **3** | 0.69 | 2.92 | 0.54 | 1.10 |
| **4** | 0.76 | 4.23 | 0.59 | 1.92 |
| **5** | 0.70 | 3.45 | 0.58 | 1.71 |
| **Average ± SD** | 0.73 ± 0.02 | 3.85 ± 0.28 | 0.58 ± 0.02 | 1.73 ± 0.16 |

Table 4. Current density vs. voltage (J–V) data for DSSC devices fabricated on ITO-coated glass using VN:ACN (85:15 valeronitrile/acetonitrile) electrolyte configuration under 100 mW $cm^{-2}$.

| VN:ACN Device | $V_{OC}$/V | $J_{SC}$/mA $cm^{-2}$ | FF | η/% |
|---|---|---|---|---|
| **1** | 0.69 | 6.82 | 0.54 | 2.05 |
| **2** | 0.73 | 6.89 | 0.51 | 2.59 |
| **3** | 0.71 | 6.94 | 0.51 | 2.62 |
| **4** | 0.73 | 6.82 | 0.51 | 2.58 |
| **5** | 0.72 | 6.92 | 0.51 | 2.61 |
| **Average ± SD** | 0.72 ± 0.01 | 6.60 ± 0.29 | 0.52 ± 0.01 | 2.49 ± 0.11 |

Table 5. Current density vs. voltage (J–V) data for DSSC devices fabricated on ITO-coated glass using MN (3-methoxypropionitrile) electrolyte configuration under 100 mW $cm^{-2}$.

| MN Devices | $V_{OC}$/V | $J_{SC}$/mA $cm^{-2}$ | FF | η/% |
|---|---|---|---|---|
| **1** | 0.55 | 5.56 | 0.58 | 1.78 |
| **2** | 0.55 | 5.60 | 0.57 | 1.78 |
| **3** | 0.55 | 5.64 | 0.57 | 1.79 |
| **4** | 0.56 | 3.02 | 0.60 | 1.03 |
| **5** | 0.55 | 5.57 | 0.58 | 1.78 |
| **Average ± SD** | 0.55 ± 0.01 | 5.08 ± 0.51 | 0.58 ± 0.01 | 1.63 ± 0.15 |

Table 6. Current density vs. voltage (J–V) data for DSSC devices fabricated on ITO-coated PEN using ACN:VN (85:15 acetonitrile/valeronitrile) electrolyte configuration under 100 mW $cm^{-2}$.

| F-DSSC | $V_{OC}$/V | $J_{SC}$/mA $cm^{-2}$ | FF | η/% |
|---|---|---|---|---|
| **1** | 0.65 | 3.13 | 0.37 | 0.77 |
| **2** | 0.66 | 2.81 | 0.52 | 1.00 |
| **3** | 0.67 | 2.45 | 0.59 | 0.98 |
| **4** | 0.66 | 2.42 | 0.60 | 0.97 |
| **5** | 0.67 | 2.47 | 0.59 | 0.99 |
| **Average ± SD** | 0.67 ± 0.01 | 2.73 ± 0.11 | 0.54 ± 0.43 | 0.97 ± 0.05 |

Table 7. Current density vs. voltage (J–V) average ± SD data for DSSC devices using three different electrolytes configurations under 100 mW $cm^{-2}$. ACN:VN corresponds to devices using 85:15 acetonitrile/valeronitrile, VN:ACN to devices using 15:85 acetonitrile/valeronitrile, and MN to devices using 3-methoxypropionitrile. F-DSSC devices are fabricated using 15:85 acetonitrile/valeronitrile.

| Device | $V_{OC}$/V | $J_{SC}$/mA $cm^{-2}$ | FF | η/% |
|---|---|---|---|---|
| **ACN:VN** [a] | 0.73 ± 0.02 | 3.85 ± 0.28 | 0.58 ± 0.02 | 1.73 ± 0.16 |
| **VN:ACN** [a] | 0.72 ± 0.01 | 6.60 ± 0.29 | 0.52 ± 0.01 | 2.49 ± 0.11 |
| **MN** [a] | 0.55 ± 0.01 | 5.08 ± 0.51 | 0.58 ± 0.01 | 1.63 ± 0.15 |
| **F-DSSC** [b] | 0.67 ± 0.01 | 2.73 ± 0.11 | 0.54 ± 0.43 | 0.97 ± 0.05 |

[a] Rigid devices on ITO-coated glass. [b] Flexible devices on ITO-coated PEN.

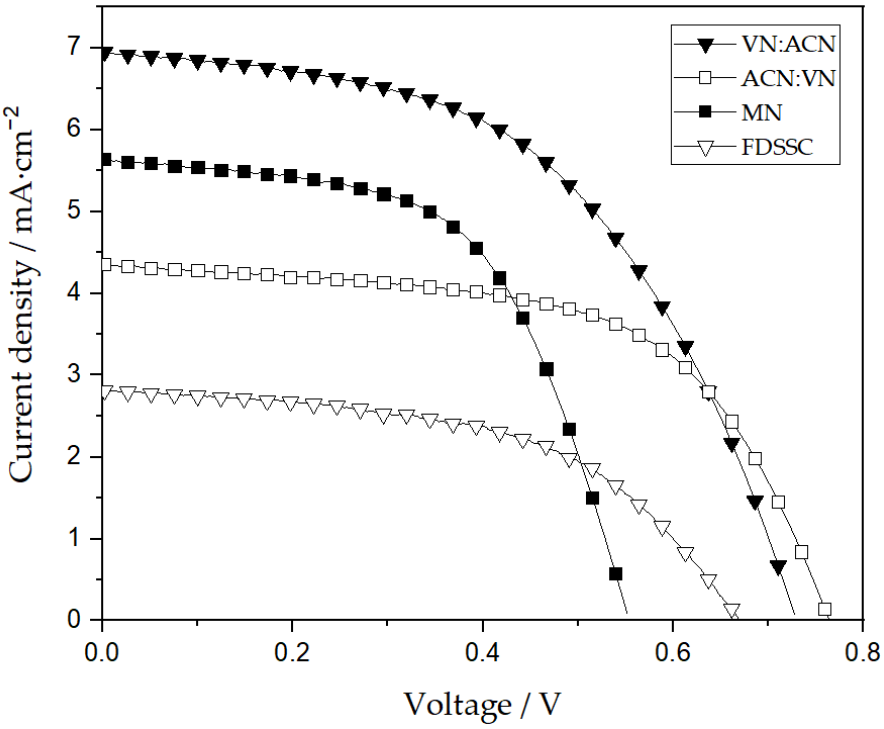


Figure 79. J–V curves of the best devices for each batch of the low-temperature DSSC-fabricated measured under 1 sun, i.e., Device 2 for ACN:VN, Device 3 for VN:ACN, Device 3 for MN, and Device 2 for F-DSSC.

### 5.4.7. Indoor Measurements paste A

PV parameters and the average ± SD of devices measured under 1000 lux LED (5600 K) using the ACN:VN electrolyte configuration fabricated on ITO-coated glass and ITO-coated PEN are shown in Table 8 and 9, respectively. Five devices were tested in each setup, named 1 to 5. Under low-light intensity, the best device fabricated on ITO-coated glass with the optimal configuration showed a $V_{OC}$ of 0.55 V, $J_{SC}$ of 35.40 µA cm$^{-2}$, an FF of 0.44, and a maximum power output (MPO) of 8.76 µW cm$^{-2}$ (Device 5 in Table 8). The best device fabricated on ITO-coated PEN obtained a $V_{OC}$ of 0.47, $J_{SC}$ of 17.11 µA cm$^{-2}$, FF of 0.47, and

a maximum power output of 4.26 μW $cm^{-2}$ (Device 2 in Table 9). Table 10 shows the average ± SD comparison of devices measured under low-light conditions.

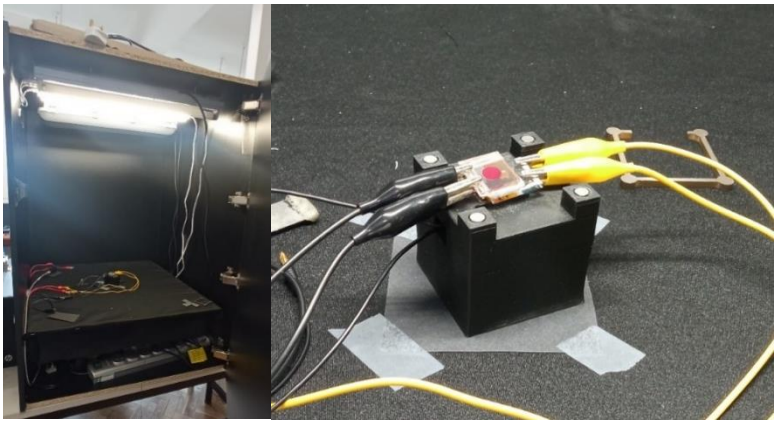

Figure 80. Indoor setup for low-light conditions measurements (left) and DSSC measurement (right).

Table 8. Current density vs. voltage (J–V) data for DSSC devices fabricated on ITO-coated glass using ACN:VN (85:15 acetonitrile/valeronitrile) electrolyte configuration under a 1000 lux LED (5600 K).

| **DSSC** | **$V_{OC}$/V** | **$J_{sc}$ /μA $cm^{-2}$** | **FF** | **MPO/μW $cm^{-2}$** |
|---|---|---|---|---|
| **1** | 0.52 | 35.60 | 0.46 | 8.66 |
| **2** | 0.52 | 34.42 | 0.47 | 8.51 |
| **3** | 0.52 | 35.69 | 0.46 | 8.66 |
| **4** | 0.54 | 32.42 | 0.45 | 8.02 |
| **5** | 0.55 | 35.40 | 0.44 | 8.76 |
| **Average ± SD** | 0.53 ± 0.01 | 34.70 ± 0.61 | 0.45 ± 0.01 | 8.52 ± 0.13 |

Table 9. Current density vs. voltage (J–V) data for DSSC devices fabricated on ITO-coated PEN using ACN:VN (85:15 acetonitrile/valeronitrile) electrolyte configuration under a 1000 lux LED (5600 K).

| F-DSSC | $V_{OC}$/V | $J_{sc}$ /µA cm$^{-2}$ | FF | MPO/µW cm$^{-2}$ |
|---|---|---|---|---|
| **1** | 0.47 | 18.27 | 0.46 | 4.02 |
| **2** | 0.47 | 17.11 | 0.47 | 4.26 |
| **3** | 0.44 | 17.59 | 0.47 | 3.76 |
| **4** | 0.46 | 15.17 | 0.52 | 3.71 |
| **5** | 0.46 | 15.24 | 0.45 | 3.21 |
| **Average ± SD** | 0.46 ± 0.01 | 16.67 ± 0.63 | 0.47 ± 0.01 | 3.80 ± 0.17 |

Table 10. Current density voltage (J–V) average ± SD data for rigid and F-DSSC devices using ACN:VN (85:15 acetonitrile/valeronitrile) measured under a 1000 lux LED, 5600 K.

| Device | $V_{OC}$/V | $J_{sc}$ /µA cm$^{-2}$ | FF | MPO/µW cm$^{-2}$ |
|---|---|---|---|---|
| **ITO-coated Glass** | 0.53 ± 0.01 | 34.70 ± 0.61 | 0.45 ± 0.01 | 8.52 ± 0.13 |
| **ITO-coated PEN** | 0.46 ± 0.01 | 16.67 ± 0.63 | 0.47 ± 0.01 | 3.80 ± 0.17 |

Figure 81 shows the J–V curves under 1000 lux illumination of the best devices for the DSSCs fabricated using low-temperature processing on ITO/glass and ITO/PEN, i.e., Device 5 and Device 2, respectively. From Table 8 to 10 and Figure 81, it can be seen that, similarly to results obtained under 1 sun illumination, the performance of DSSCs based on ITO/glass is generally better than for ITO/PEN substrates depending on various factors. In general, higher optical transparency, less surface roughness, and better thermal and mechanical stability are the main reasons for the better performance of DSSCs based on ITO/glass compared to those on ITO/PET.

Higher optical transparency allows a greater amount of light to reach the active layer of the DSSC, enhancing light absorption and hence cell efficiency. A smoother surface of ITO/glass substrates promotes better adhesion of subsequent layers, such as the compact and mesoporous titania layers and, hence, photoactive dye and electrolyte, resulting in improved charge transport and reduced charge recombination within the cell. In addition, ITO/glass substrates are more resistant to thermal expansion and contraction, minimizing the potential for cracks.

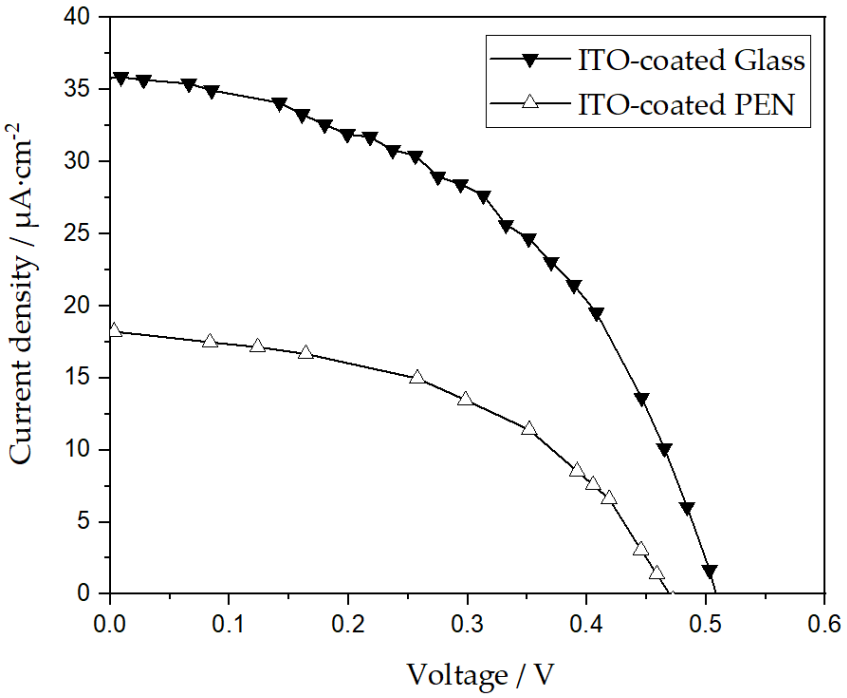


Figure 81. J–V curves of the best low-temperature DSSC fabricated measured under low-light in-tensity (1000 lux LED (5600 K) on both ITO-coated glass and PEN substrates using a mixture of 15:85 valeronitrile/acetonitrile as solvent, i.e., Device 5 and Device 2, respectively.

### 5.4.8. PV characterization and J-V curves for rigid and F-DSSC fabricated with paste B

Devices were fabricated using UV-$O_3$ treated powders, Y123 dye and VN:AC electrolyte since it was found to be work better with low-temperature films. In Figure 83, JV curves measured of ITO-Glass devices fabricated using copper electrolyte are shown.

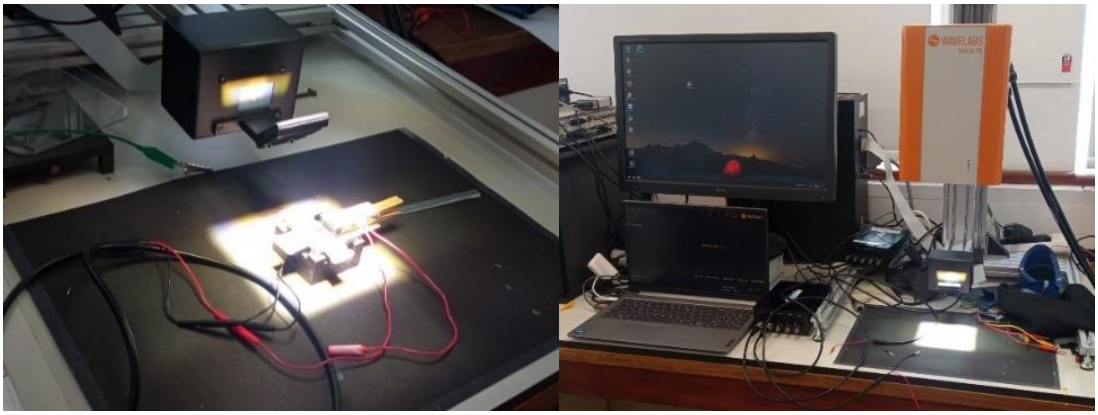

Figure 82. Waves lab solar simulator.

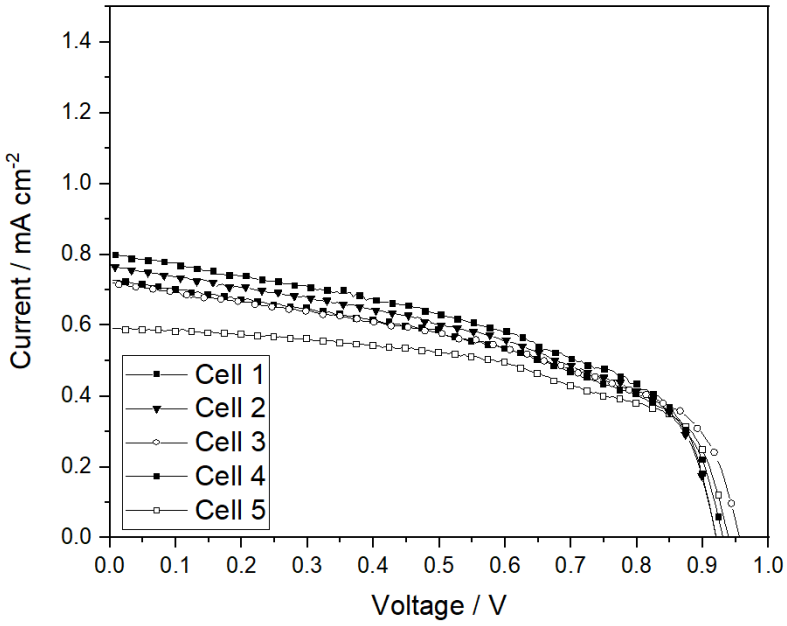


Figure 83. J–V curves at one sun of the low-temperature DSSC-fabricated using paste B prepared with UV-$O_3$ treated powder, Y123 dye and Copper electrolyte.

Table 11. Current density vs. voltage (J–V) data under 1 sun for DSSC devices fabricated on ITO-Glass using paste B prepared with UV-$O_3$ treated powder, Y123 dye and Copper electrolyte.

| **Paste B UV-$O_3$ treated Y123/Cu** | **$V_{OC}$/V** | **$J_{SC}$/mA cm$^{-2}$** | **FF** | **η/%** |
|---|---|---|---|---|
| **1** | 0.94 | 0.59 | 0.55 | 0.30 |
| **2** | 0.93 | 0.73 | 0.48 | 0.33 |
| **3** | 0.94 | 0.89 | 0.72 | 0.61 |
| **4** | 0.94 | 0.91 | 0.71 | 0.61 |
| **5** | 0.94 | 0.91 | 0.70 | 0.60 |

In Figure 84, JV curves measured of ITO-Glass devices fabricated using VN:AC electrolyte are shown.

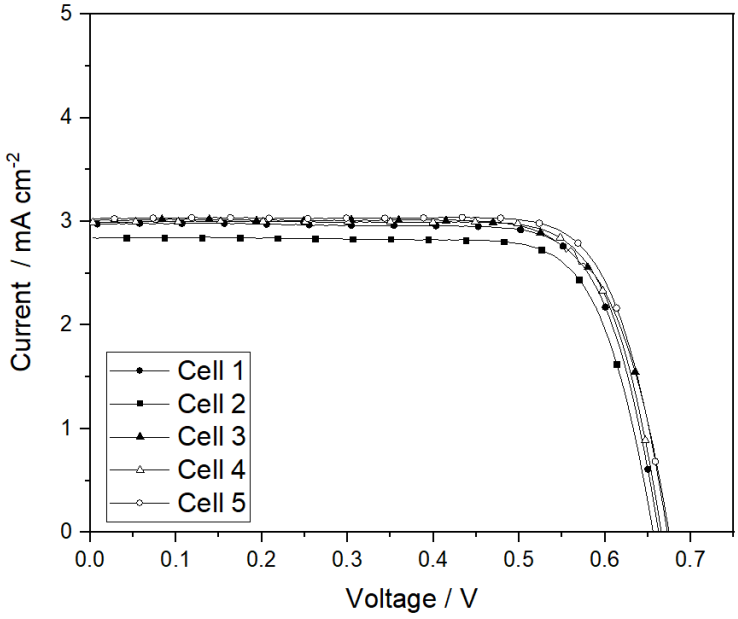

Figure 84. J–V curves at one sun of the low-temperature DSSC-fabricated using paste B prepred with UV-$O_3$ treaed powder, Y123 dye and Iodide electrolyte.

Table 12. Current density vs. voltage (J–V) data under 1 sun for DSSC devices fabricated on ITO-Glass using paste B prepared with UV-$O_3$ treated powder, Y123 dye and Iodide electrolyte.

| **Paste B UV-$O_3$ treated Y123/Iodide** | **$V_{OC}$/V** | **$J_{SC}$/mA cm$^{-2}$** | **FF** | **η/%** |
|---|---|---|---|---|
| **1** | 0.67 | 2.82 | 0.77 | 1.46 |
| **2** | 0.66 | 2.84 | 0.77 | 1.47 |
| **3** | 0.67 | 2.98 | 0.75 | 1.52 |
| **4** | 0.68 | 3.00 | 0.75 | 1.57 |
| **5** | 0.68 | 3.00 | 0.77 | 1.58 |

### 5.4.9. PV characterization and J-V curves for rigid and F-DSSC fabricated with paste C

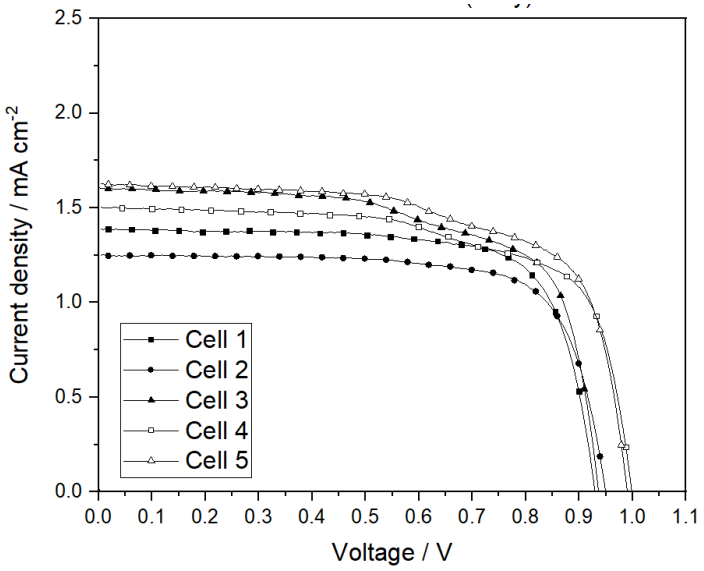

Figure 85. J–V curves at one sun of the low-temperature DSSC-fabricated using paste C, Y123 dye and Copper electrolyte.

Table 13. Current density vs. voltage (J–V) data under 1 sun for DSSC devices fabricated on ITO-Glass using paste C, Y123 dye and Copper electrolyte.

| **Paste C - Y123/Cu** | **$V_{OC}$/V** | **$J_{SC}$/mA cm$^{-2}$** | **FF** | **η/%** |
|---|---|---|---|---|
| **1** | 0.95 | 1.38 | 0.72 | 0.95 |
| **2** | 0.95 | 1.24 | 0.74 | 0.87 |
| **3** | 0.93 | 1.59 | 0.66 | 1.00 |
| **4** | 0.99 | 1.50 | 0.67 | 1.00 |
| **5** | 0.98 | 1.62 | 0.66 | 1.07 |

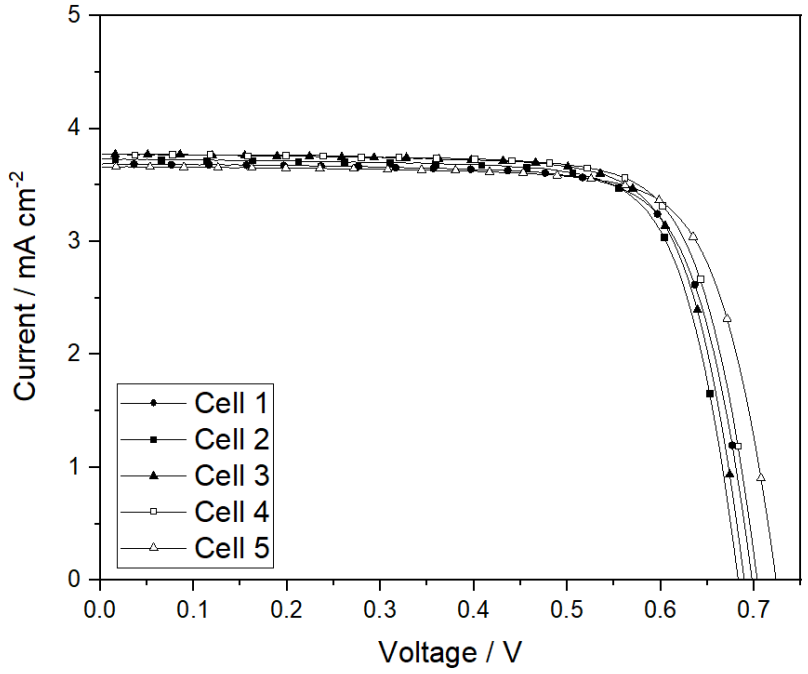


Figure 86. J–V curves at one sun of the low-temperature DSSC-fabricated using paste C, Y123 dye and Iodide electrolyte.

Table 14. Current density vs. voltage (J–V) data under 1 sun for DSSC devices fabricated on ITO-Glass using paste C, Y123 dye and Iodide electrolyte.

| **Paste C - Y123/Iodide** | **$V_{OC}$/V** | **$J_{SC}$/mA cm$^{-2}$** | **FF** | **η/%** |
|---|---|---|---|---|
| **1** | 0.69 | 3.68 | 0.76 | 1.95 |
| **2** | 0.68 | 3.42 | 0.75 | 1.93 |
| **3** | 0.68 | 3.77 | 0.76 | 1.97 |
| **4** | 0.69 | 3.77 | 0.76 | 2.00 |
| **5** | 0.72 | 3.66 | 0.75 | 2.00 |

Flexible devices were then fabricated using paste C, Y123 dye and VN:AC electrolyte since this configuration showed to work better for this new low-temperature set. In Figure 87, JV curves measured of flexible ITO-PEN devices fabricated using VN:AC electrolyte are shown.

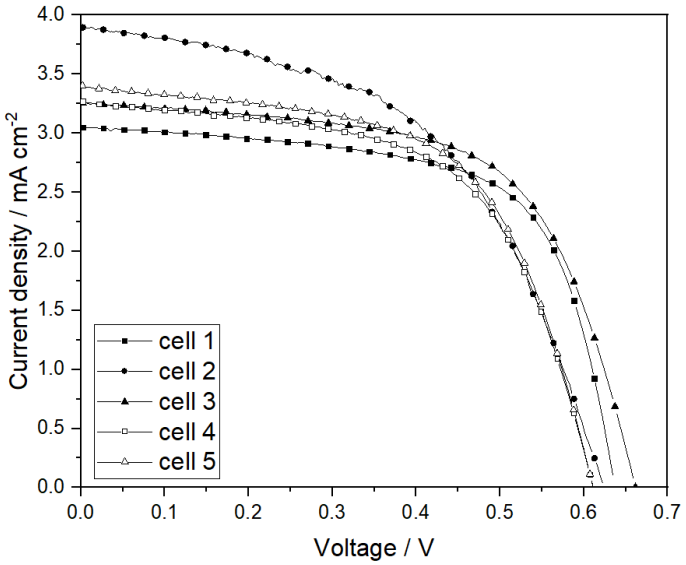

Figure 87. J–V curves under 1 sun of the low-temperature F-DSSC-fabricated using paste C, Y123 dye and Iodide electrolyte.

Table 15. Current density vs. voltage (J–V) data under 1 sun for FDSSC devices fabricated on ITO-PEN using paste D, Y123 dye and Iodide electrolyte.

| **Paste C - Y123/Cu** | **$V_{OC}$/V** | **$J_{SC}$/mA cm$^{-2}$** | **FF** | **η/%** |
|---|---|---|---|---|
| **1** | 0.63 | 3.04 | 0.65 | 1.27 |
| **2** | 0.62 | 3.89 | 0.52 | 1.25 |
| **3** | 0.66 | 3.25 | 0.62 | 1.33 |
| **4** | 0.61 | 3.26 | 0.59 | 1.18 |
| **5** | 0.61 | 3.39 | 0.59 | 1.23 |

### 5.4.10. Indoor measurements paste C

The previous devices fabricated were tested under indoor low-light conditions. In Figure 88, JV curve of ITO-Glass devices using paste C, Y123 dye and VN:CAN electrolyte under simulated indoor light is shown.

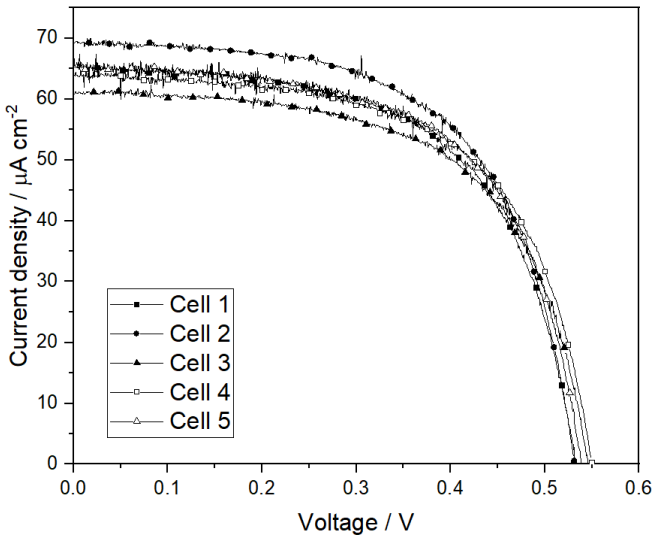

Figure 88. J–V curves of the low-temperature DSSC fabricated ITO-glass using paste D, Y123 dye and Iodide electrolyte measured under low-intensity (1000 lux white OSRAM lamp (5600 K)) with an irradiance of 310 μW/ $cm^{-2}$, scan rate (V/s): 0.008.

Table 16. Current density vs. voltage (J–V) data under indoor light (1000 lux) for DSSC devices fabricated on ITO-Glass using paste D, Y123 dye and Iodide electrolyte.

| **Paste D - Y123/Iodide** | **$V_{OC}$/V** | **$J_{SC}$/μA $cm^{-2}$** | **FF** | **MPO/μW $cm^{-2}$** | **η/%** |
|---|---|---|---|---|---|
| **1** | 0.53 | 65.17 | 0.60 | 21.11 | 6.80 |
| **2** | 0.53 | 65.16 | 0.60 | 21.16 | 6.82 |
| **3** | 0.53 | 61.50 | 0.61 | 20.25 | 6.52 |
| **4** | 0.54 | 64.14 | 0.62 | 21.40 | 6.89 |
| **5** | 0.54 | 66.06 | 0.60 | 21.36 | 6.87 |

In Figure 89, JV curve of ITO-Glass devices using paste C, Y123 dye and copper electrolyte under simulated indoor light is shown.

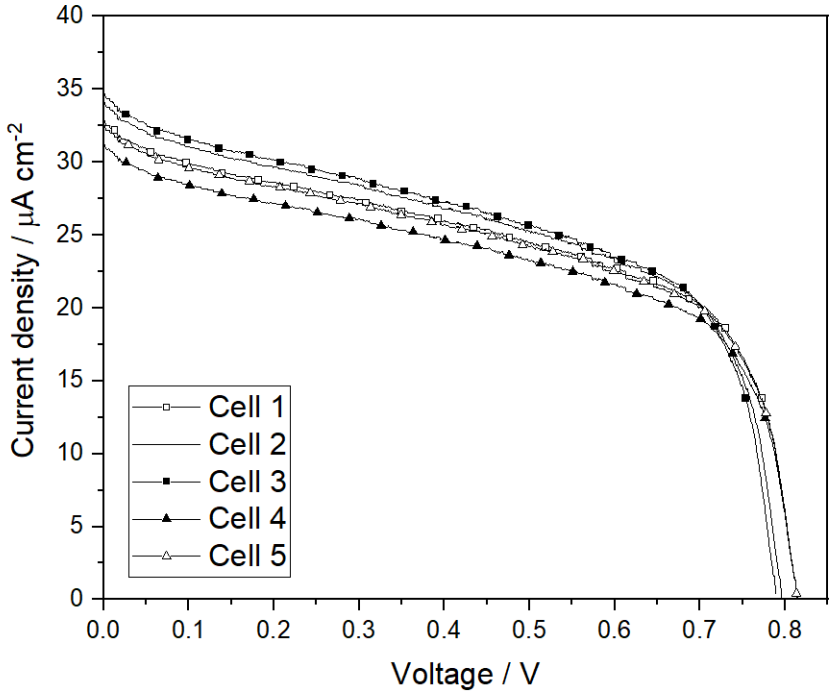

Figure 89. J–V curves of the low-temperature DSSC fabricated ITO-glass using paste D, Y123 dye and copper electrolyte measured under low-intensity (1000 lux white OSRAM lamp (5600 K)) with an irradiance of 301 μW/ $cm^{-2}$, Scan Rate (V/s): 0.008.

Table 17. Current density vs. voltage (J–V) data under indoor light (1000 lux) for DSSC devices fabricated on ITO-Glass using paste D, Y123 dye and Copper electrolyte.

| **Paste D - Y123/Cu** | **$V_{OC}$/V** | **$J_{SC}$/μA $cm^{-2}$** | **FF** | **MPO/μW $cm^{-2}$** | **η/%** |
|---|---|---|---|---|---|
| **1** | 0.81 | 32.61 | 0.53 | 14.23 | 4.73 |
| **2** | 0.79 | 33.94 | 0.54 | 14.46 | 4.80 |
| **3** | 0.78 | 32.67 | 0.51 | 13.80 | 4.58 |
| **4** | 0.81 | 31.03 | 0.52 | 13.52 | 4.49 |
| **5** | 0.81 | 32.34 | 0.53 | 14.16 | 4.70 |

In Figure 90, JV curve of flexible ITO-PEN devices using paste C, Y123 dye and Iodide electrolyte under simulated indoor light is shown.

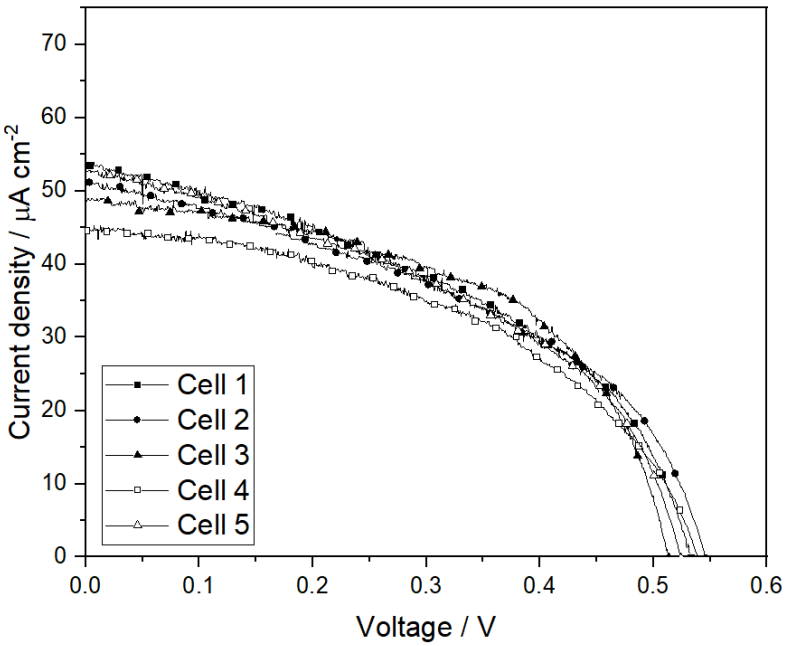

Figure 90. J–V curves of the low-temperature FDSSC using paste D, Y123 dye and Iodide electrolyte measured under low-intensity (1000 lux white OSRAM lamp (5600 K)) with an irradiance of 310 μW/ $cm^{-2}$, Scan Rate (V/s): 0.008.

Table 18. Current density vs. voltage (J–V) data under indoor light (1000 lux) for FDSSC devices fabricated on ITO-PEN using paste D, Y123 dye and Iodide electrolyte.

| **Flexible Paste C - Y123/Cu** | **$V_{OC}$/V** | **$J_{SC}$/μA $cm^{-2}$** | **FF** | **MPO/μW $cm^{-2}$** | **η/%** |
|---|---|---|---|---|---|
| **1** | 0.53 | 54.14 | 0.43 | 12.41 | 4.11 |
| **2** | 0.54 | 51.5 | 0.43 | 12.14 | 4.03 |
| **3** | 0.51 | 49.20 | 0.52 | 13.32 | 4.42 |
| **4** | 0.54 | 43.66 | 0.48 | 11.48 | 3.80 |
| **5** | 0.52 | 53.00 | 0.43 | 12.03 | 3.98 |

### 5.4.11. Electrochemical Impedance Spectroscopy

To gain a better understanding of the internal behaviour of this innovative low-temperature system, Electrochemical impedance spectroscopy (EIS) measurements were conducted to compare the effect of the electrolyte on the system. Impedance measurements were performed by subjecting the cells to 1 sun and using an AutoLab potentiostat to apply different voltages, passing through the cells' maximum power point voltage, and perturbing it at various frequencies. The BODE and NYQUIST plots of both systems at different voltages are presented below. The impedance measurements were carried out using the best cell from each series.

### 5.4.12. Low temperature Y123 / Cu devices

In Figure 91 it can be seen how as the voltage decreases the imaginary component of the resistance increases. Figure 91 d), shows a closer view of the Nyquist plot to observe the behavior of the impedance at the highest cell voltage. In this figure it can be observed the first semicircle corresponding to the charge transfer in the counter electrode at high frequencies. At mid-frequencies, a larger semicircle can be observed corresponding to the electronic transfer between the electrons in the conduction band of $TiO_2$ and the electrolyte, i.e. electronic recombination. It can be seen that a third semicircle becomes evident for the lower frequencies with greater presence than the second evidencing electrolyte mass transport problems.

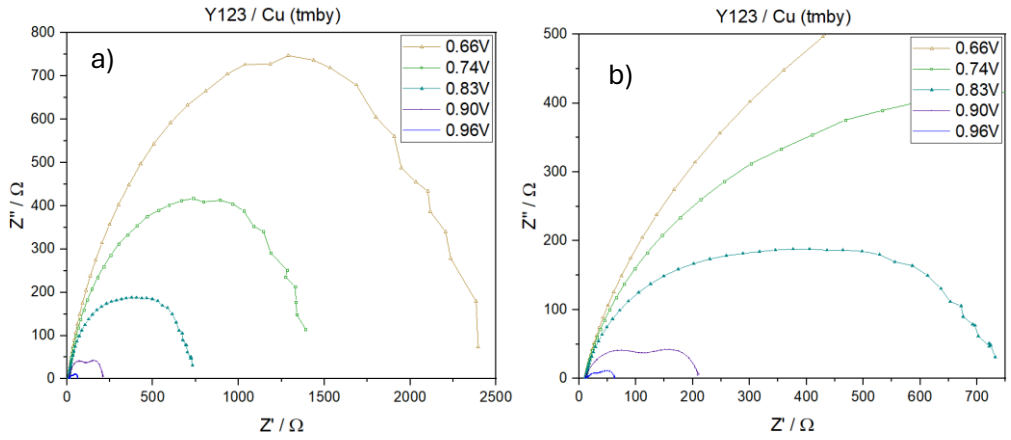

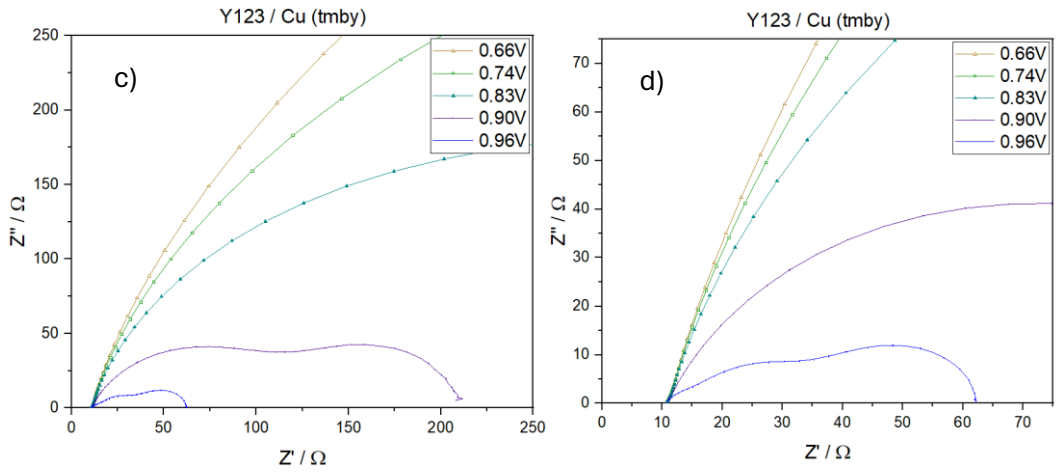


Figure 91. Electrochemical impedance spetra of low-temperature DSSC fabricated using paste C, Y123 dye and copper electrolyte. a) wide view of measurements using different voltages. b – d) Zoom in of spectra for a better look.

In Figure 92, it can be observed that as the voltage increases and the frequency decreases, the phase begins to exhibit a second peak.

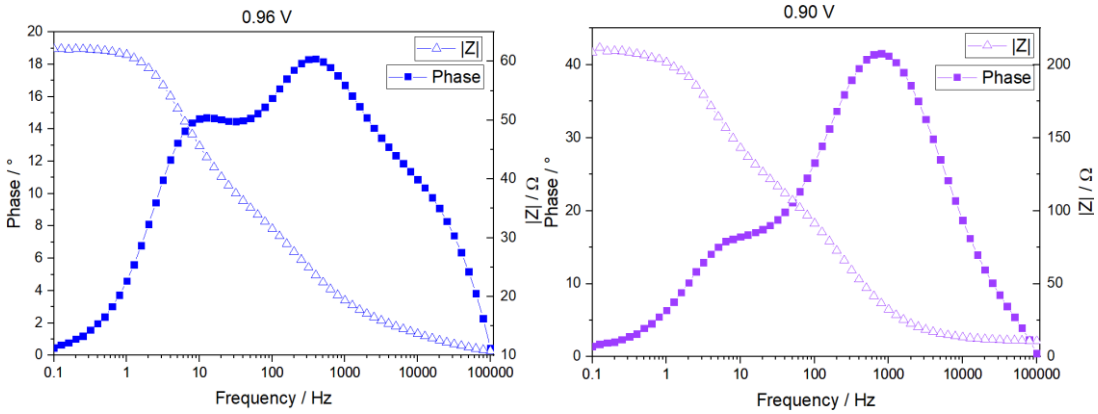

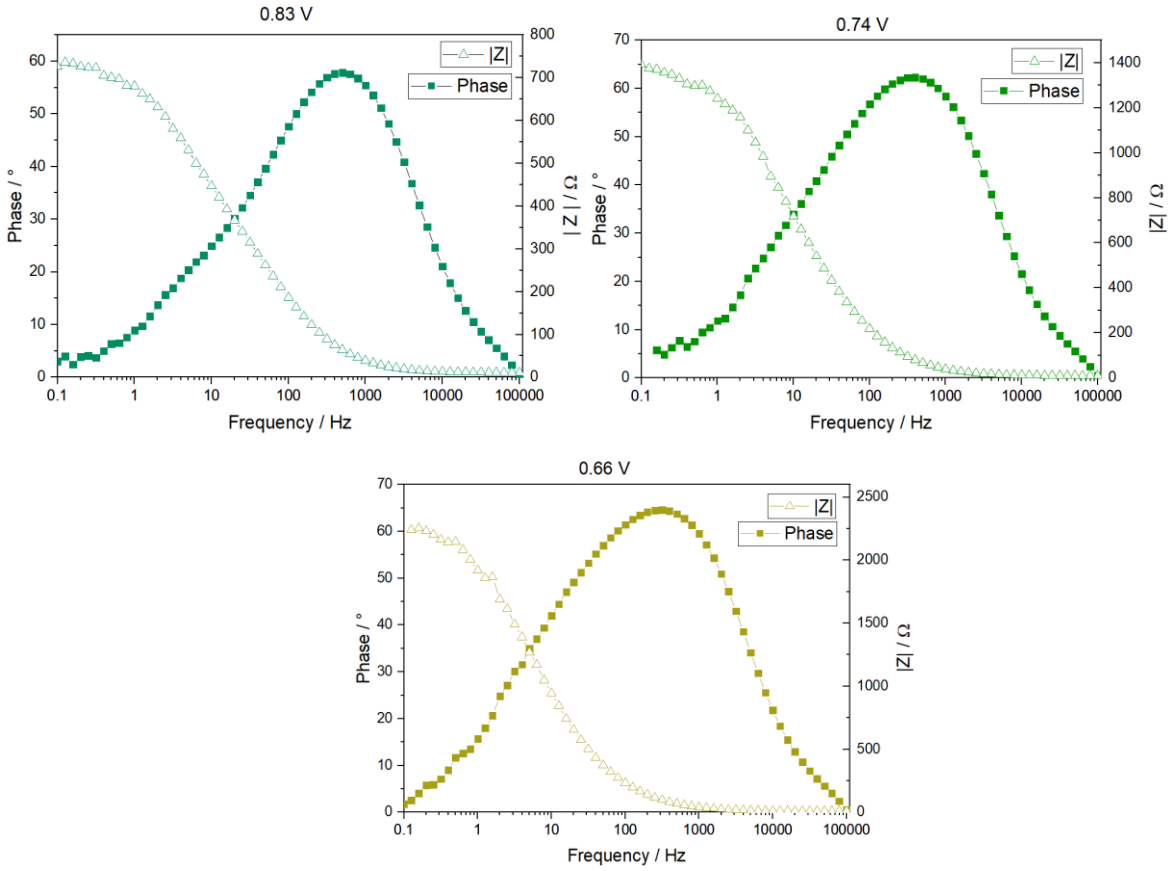


Figure 92. Bode plot of low-temperature DSSC fabricated using paste C, Y123 dye and copper electrolyte at 0.66 V (blue), 0.74 V (purple), 0.83 V (turquoise), 0.90 V (green), and 0.96 V (yellow)

### 5.4.13. Low temperature Y123 / Iodide devices

In Figure 93, it can be observed that as the voltage decreases, the imaginary component of resistance increases. Figure 93 d), shows a closer view of the Nyquist plot to observe the impedance behavior at the highest cell voltage. In this figure, the first semicircle corresponding to charge transfer at the counter electrode at high frequencies can be observed. At intermediate frequencies, a larger semicircle corresponding to electronic transfer between

the conduction band electrons of $TiO_2$ and the electrolyte is visible. It can be observed that a third semicircle becomes evident for lower frequencies with less prominence than the second one compared to the Y123/Copper devices showing that in this case the electronic recombination in the $TiO_2$ and the electrolyte is stronger factor affecting the performance of this devices.

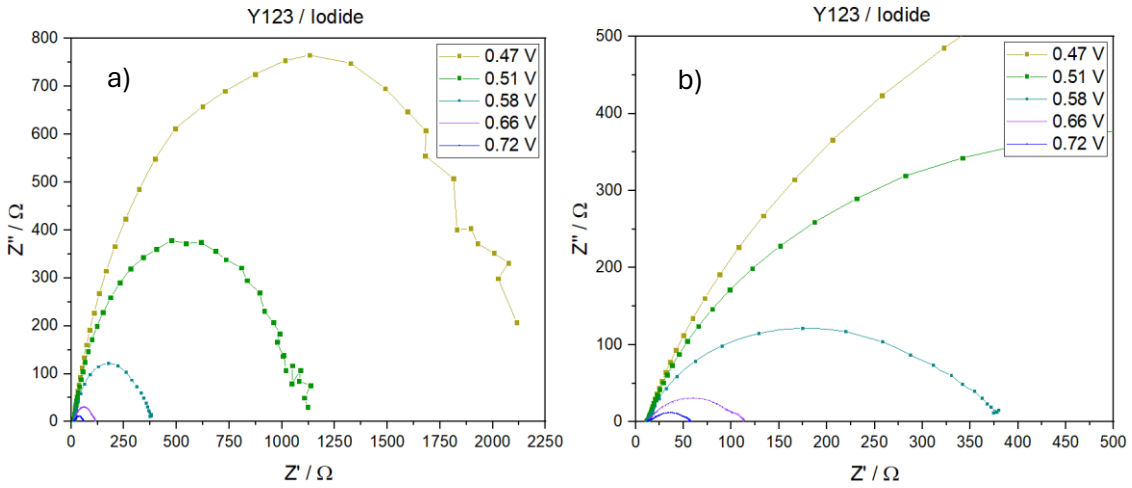

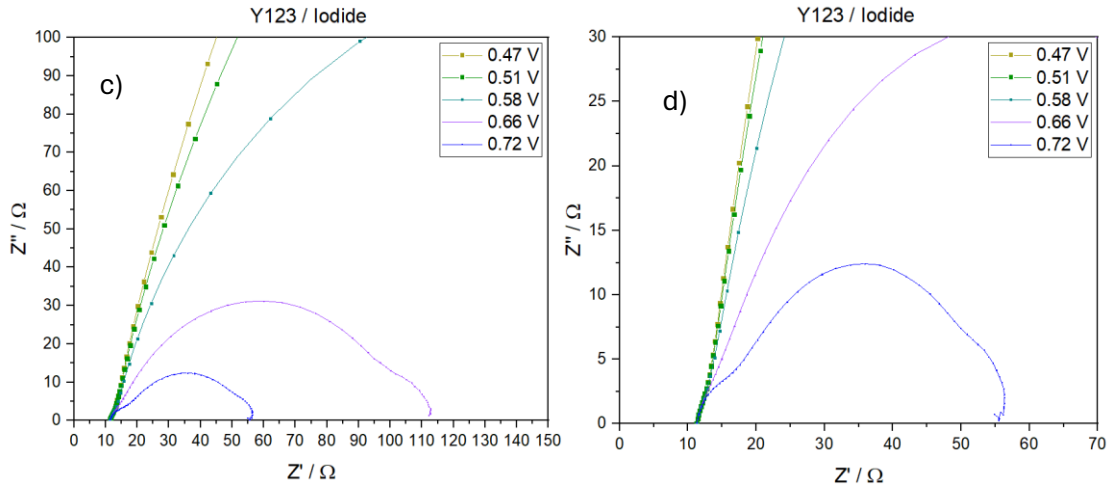


Figure 93. Electrochemical impedance spetra of low-temperature DSSC fabricated using paste C, Y123 dye and Iodide electrolyte. a) wide view of measurements using different voltages. b – d) Zoom in of spectra for a better look.

In the Figure 93, it can be observed that as the voltage increases and the frequency decreases, the phase begins to show a second valley.

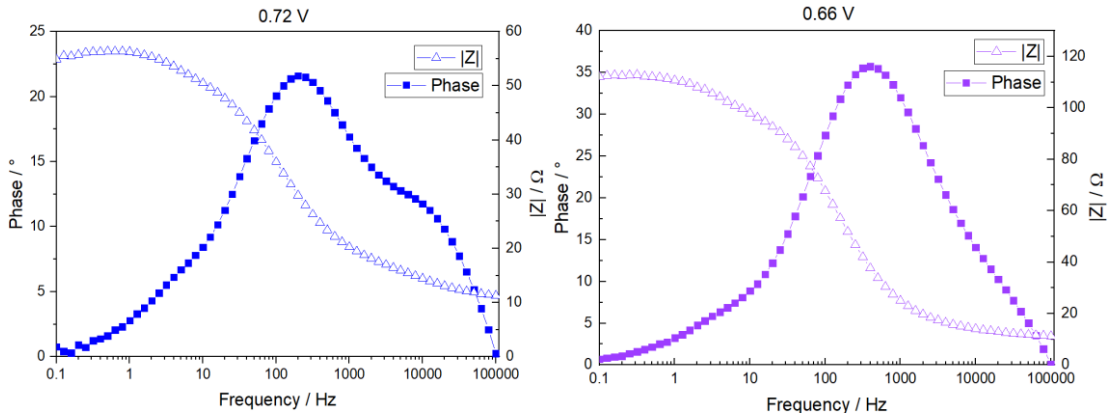

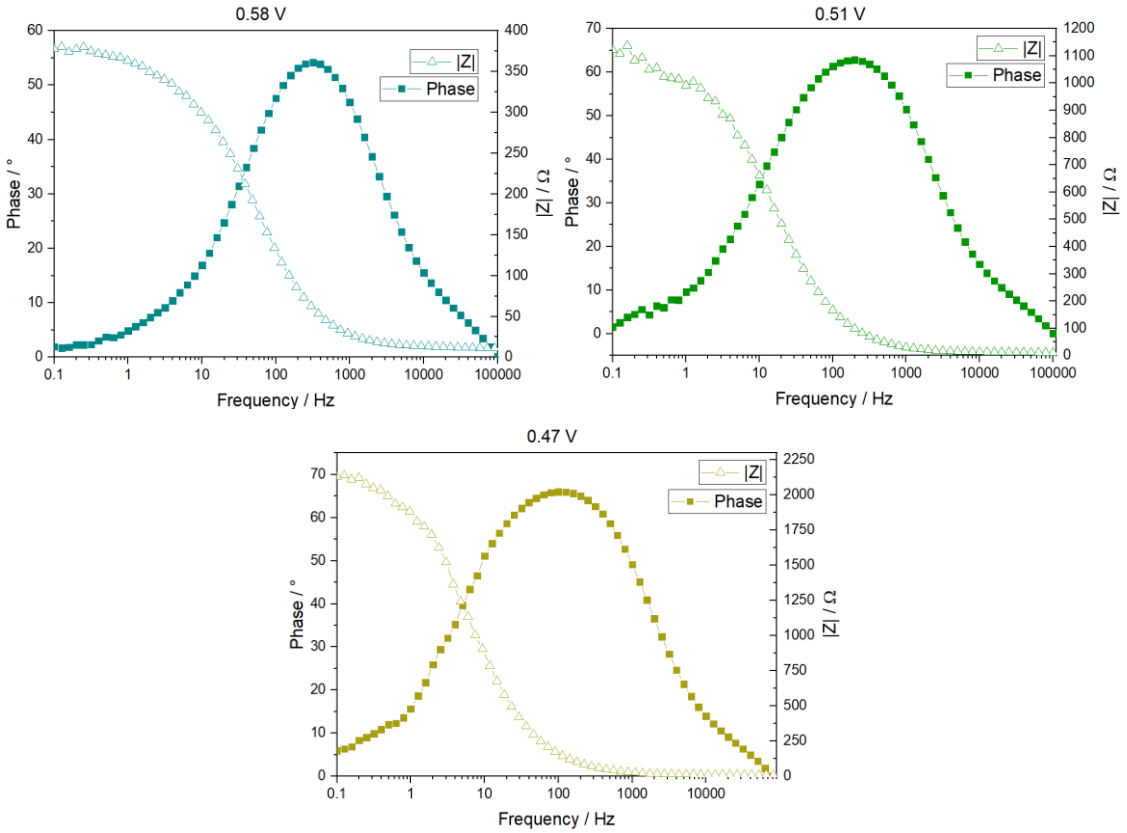


Figure 94. Bode plot of low-temperature DSSC fabricated using paste C, Y123 dye and iodide electrolyte at 0.72 V (blue), 0.66 V (purple), 0.58 V (turquoise), 0.51 V (green), and 0.47 V (yellow)

## 5.5. High-temperature DSSCs

In this section, the results obtained using synthesized particles of anatase and brookite for high-performance cells are presented.

### 5.5.1. Scanning electron microscopy.

In this section, SEM images of the films prepared with commercial 30NR-D, WER02, anatase and brookite pastes are shown.

#### 5.5.1.1. Reference cells

For the reference cells, it can be observed in Figure 95 that the deposition of the active film, using the commercial 30NR-D paste, achieved a thickness of 4.2 μm. Above, it can be seen that the dispersion film deposited onto the active layer, using the commercial WER20 paste, achieved a thickness of 5.4 μm, giving it a total thickness of 9.6 μm.

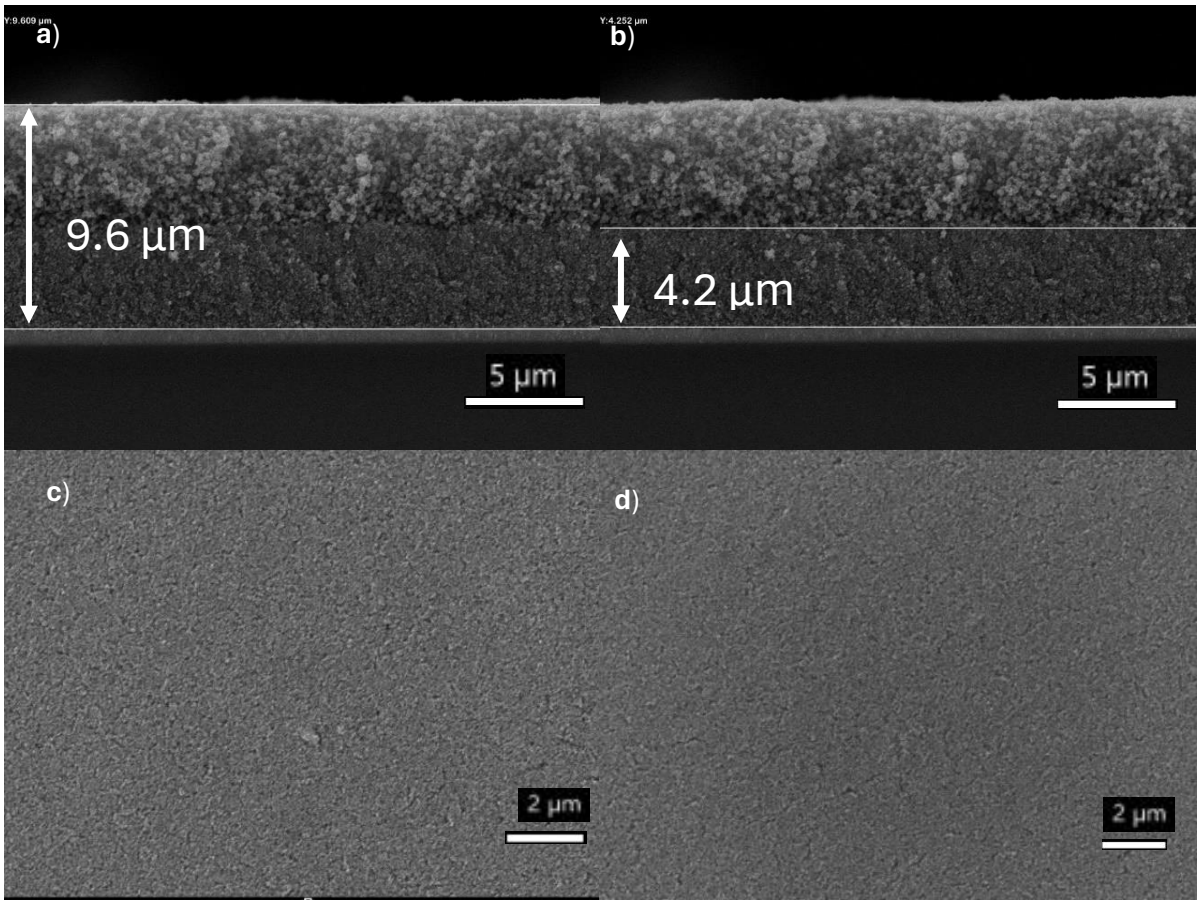


Figure 95. Film thickness of reference cells using commerical 30NR-D paste on FTO-Glass at 20 KV and 5,000 X showing a total tchickness of a) 9.6 µm, b) active layer of 4.2 µm, c) and d) morphology of the active layer of the reference cells without scattering layer.

**5.5.1.2.. Anatase cells**

For cells fabricated with synthesized anatase particles, it can be observed in Figure 96 a) and b), that the deposition of the active film achieved a thickness of 4 µm. Above, it can be seen that the dispersion film deposited onto the active layer, using the commercial WER20 paste, achieved a thickness of 4.4 µm, giving it a total thickness of 8.8 µm. Figure 96 c) and d),

shows the topography of the deposited film using antase nanoparticles, it can be obsverved an irregular surface with some particle agglomerations.

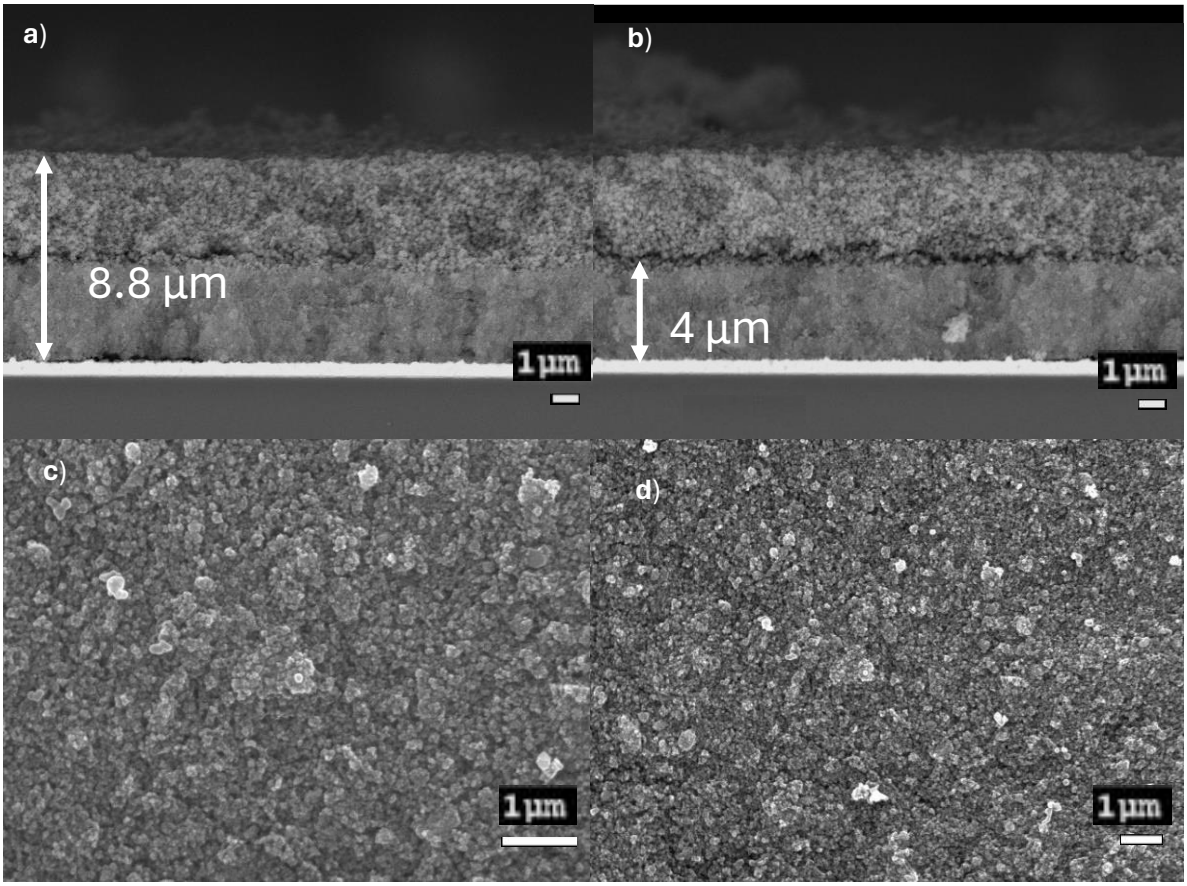


Figure 96. Film thickness of anatase cells on FTO-Glass at 15 KV and a) 5,000 X showing the total thickness of 8.8 µm, b) 5,000 X showing the thickness of the active layer of 4 µm and topography of anatase cells without the scattering layer at c) 15,000 X and d) 8,000 X.

#### 5.5.1.3. Brookite cells

For cells fabricated with synthesized brookite particles, it can be observed that the deposition of the active film exhibited a very irregular surface achieving variable thicknesses ranging

from 7.5 to 4.2 μm (Figure 97, a)) and 2.5 to 5.5 μm (Figure 97, b)). Above this layer, it can be seen that the dispersion film deposited onto the active layer, using the commercial WER02 paste, achieved a variable thickness, giving it a total thickness of 10 μm.

Figure 97 c) and d), shows the topography of the deposited brookite films without scattering layer where it can be obsverved massive  particle agglomerations and large pores.

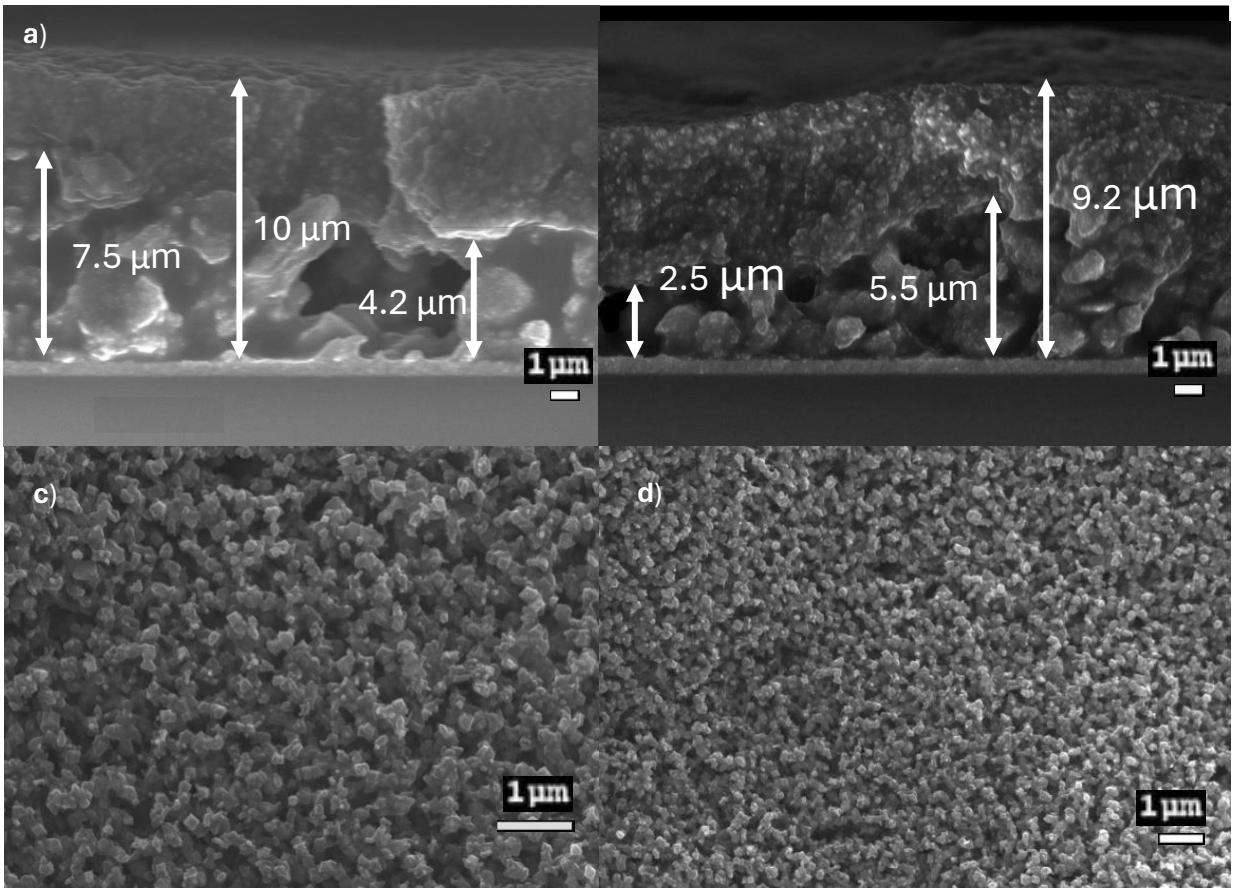


Figure 97. Film thickness of brookite cells on FTO-Glass at 15 KV and a) and b) 5,000 X showing an irregular active layer thickness ranging from 2.5 to 7.5 μm, and total thickness around 10 μm, and the topography of brookite cells without the scattering layer at c) 15,000 X and d) 8,000 X showing large agglomerates.

### 5.5.2. Rheology measurements

The high-temperature pastes were subjected to rheological tests using a rheometer at 25°C. Figure 98 shows the behavior of the pastes compared to the commercial pastes 30NR-D and WER20. It can be observed how the viscosity of the pastes varies as a function of shear stress. The behavior of the pastes is typical of a non-Newtonian fluid as viscosity changes with increasing shear stress. Both pastes exhibit pseudoplastic behavior in which viscosity decreases as shear stress increases. However the viscosity of anatase and brookite paste needs to be improved in order to increase the viscosity to produce a more homogenoues films.

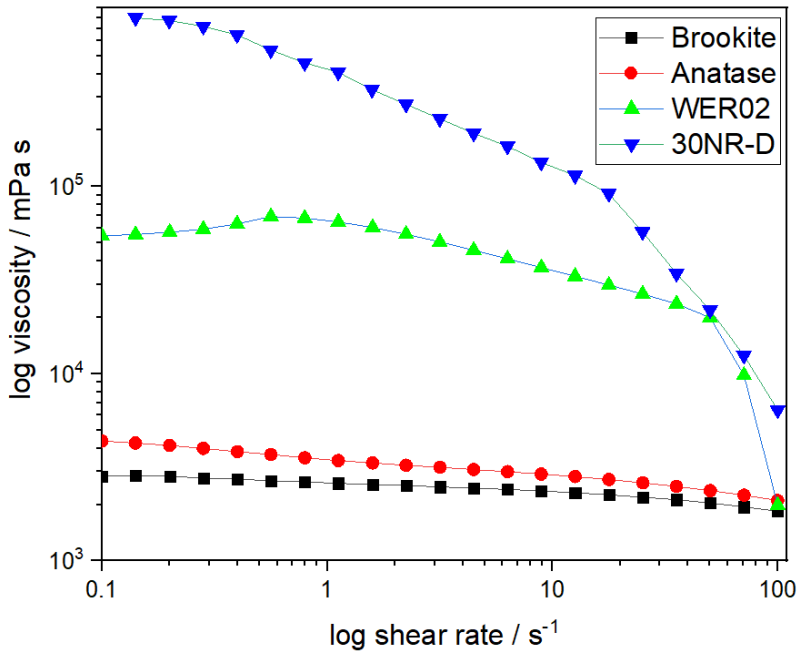


Figure 98. Viscosity behaviour of commercial 30NR-D paste (blue), WER20 (green), anatase paste (red) and brookite paste (black) at 25 °C.

### 5.5.3. Dye desorption

The desorption tests of Y123 dye were conducted following the same methodology as for the low-temperature pastes. The Figure 99 shows that the highest dye adsorption on the surface of the active layer was obtained by the synthesized anatase paste, while the commercial paste has slightly better adsorption. The brookite paste exhibited the lowest dye adsorption compared to the other pastes.

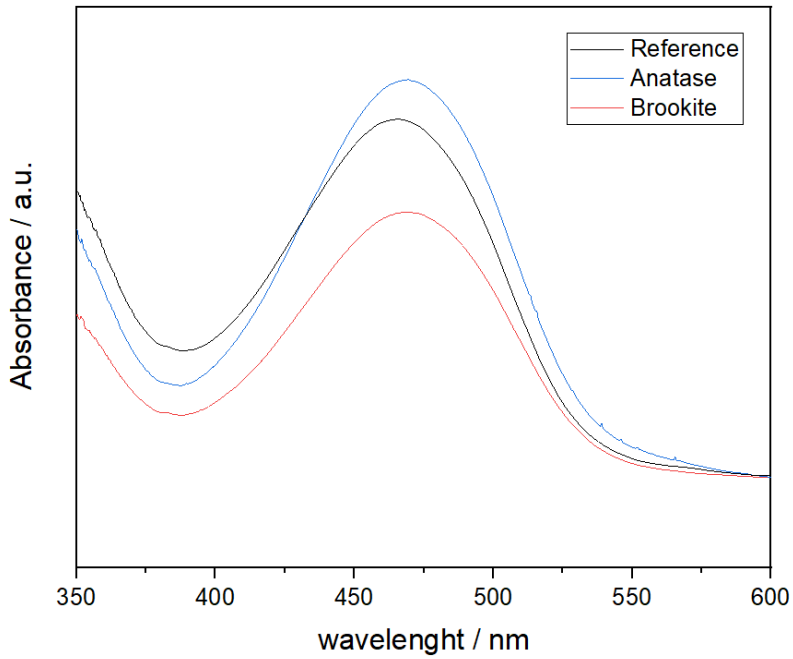


Figure 99. UV-Vis spectroscopy of desorbed dye from films. Commercial 30NR-D active layer (black), synnthesized anatase active layer (Blue) and synnthesized brookite active layer (red). Spectra from brookite was displaced upwards to match reference and anatese spectra at 600 nm for a more accurate comparison.

### 5.5.4. High-performance DSSCs PV characterization

The cells manufactured with these high-temperature pastes were characterized under sunlight. Below are the results.

#### 5.5.4.1. Reference cells

Figure 100 shows the JV curves of the reference cells using the commercial pastes 30NR-D, WER02, Y123 dye, and copper electrolyte.

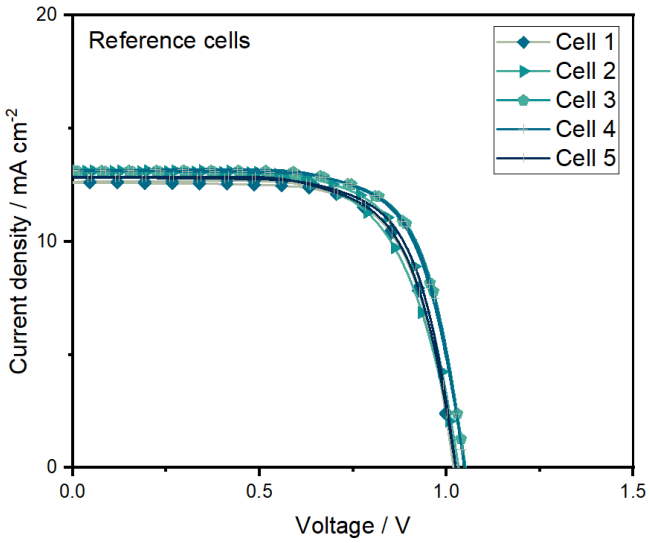


Figure 100. JV curves of reference cells

Table 19. Current density vs. voltage (J–V) data under 1 sun for DSSCs reference cells.

| Reference cells | $V_{OC}$/V | $J_{SC}$/mA cm$^{-2}$ | FF | η/% |
|---|---|---|---|---|
| **1** | 1.053 | 13.19 | 70.8 | 9.8 |
| **2** | 1.051 | 13.16 | 70.7 | 9.8 |
| **3** | 0.988 | 13.61 | 70.6 | 9.5 |
| **4** | 0.968 | 14.16 | 69.1 | 9.5 |
| **5** | 0.994 | 13.62 | 69 | 9.3 |

### 5.5.4.2. Anatase cells A-Synth paste

Figure 101 shows the JV curves of the cells fabricated with synthesized anatase particles, which were used in the paste directly from the commercial synthesis WER02 as a dispersion layer, Y123 dye, and copper electrolyte.

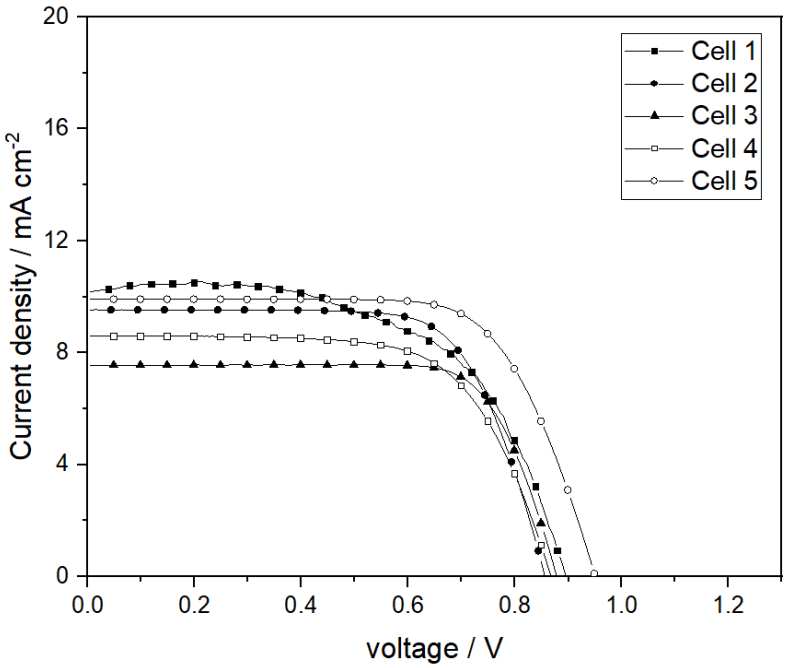


Figure 101. JV curves of anatase cells fabricated with A-Synth paste

Table 20. Current density vs. voltage (J–V) data under 1 sun for DSSCs anatase directly de from the syntesis.

| A-Synth paste | $V_{OC}$/V | $J_{SC}$/mA cm$^{-2}$ | FF | η/% |
|---|---|---|---|---|
| **1** | 0.896 | 10.17 | 59.8 | 5.45 |
| **2** | 0.856 | 9.53 | 70.6 | 5.76 |
| **3** | 0.878 | 7.55 | 75.2 | 4.98 |
| **4** | 0.867 | 8.595 | 66.3 | 4.94 |
| **5** | 0.950 | 9.91 | 70 | 6.58 |

### 5.5.4.3. Anatase cells A-Bmill paste

Figure 102 shows the JV curves of the cells fabricated with synthesized anatase particles that were ground prior to paste preparation. The cells use the commercial paste WER02 as a dispersion layer, Y123 dye, and copper electrolyte.

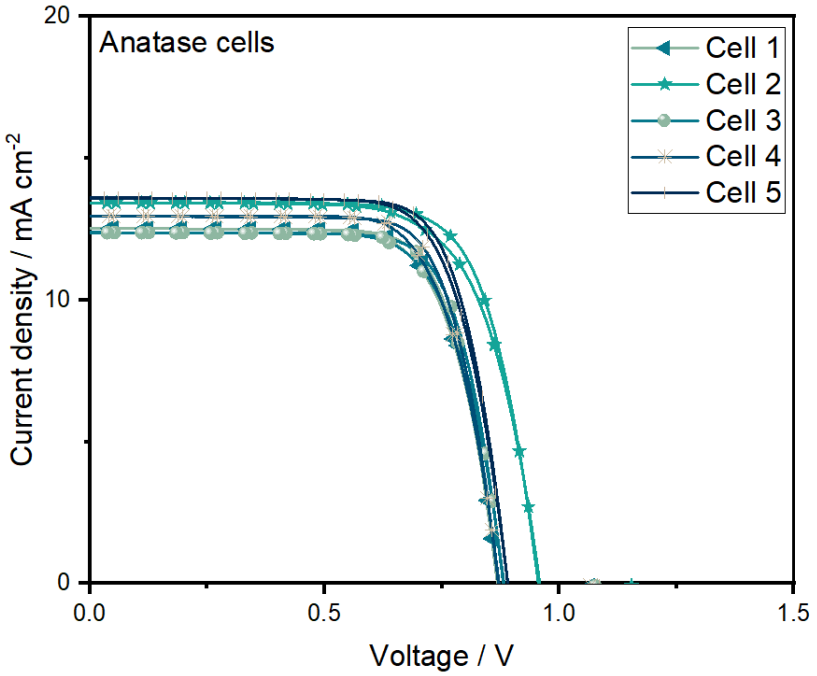


Figure 102. JV curves of ball milled anatase cells

Table 21. Current density vs. voltage (J–V) data under 1 sun for DSSCs ballmilled anatase cells.

| A-Bmill paste | Voc/V | Jsc/mA cm$^{-2}$ | FF | η/% |
|---|---|---|---|---|
| **1** | 0.937 | 13.90 | 73.8 | 9.61 |
| **2** | 0.954 | 13.50 | 73.5 | 9.46 |
| **3** | 0.889 | 12.44 | 75.1 | 9.13 |
| **4** | 0.869 | 13.02 | 75.2 | 8.50 |
| **5** | 0.880 | 12.44 | 74.9 | 8.20 |

### 5.5.4.4. Brookite cells

Figure 103 shows the JV curves of ,cells fabricated using brookite nanoparticles, WER02, Y123 dye, and copper electrolyte.

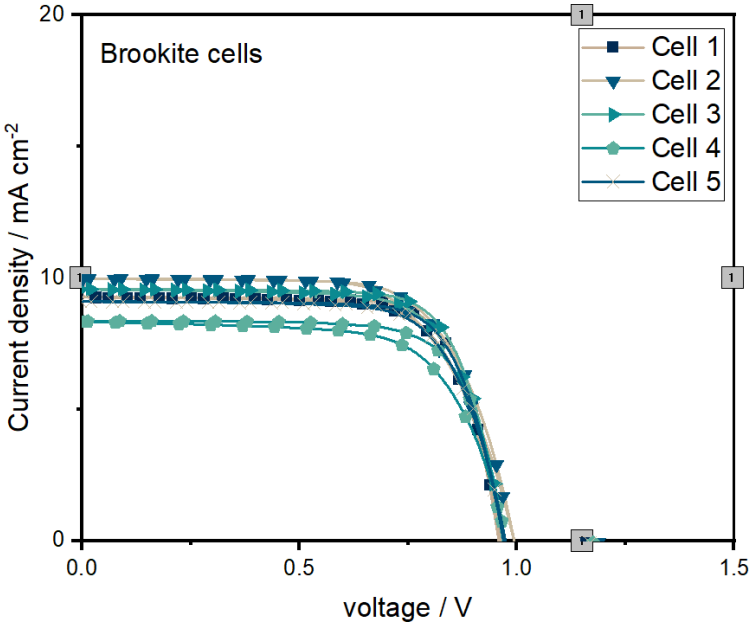


Figure 103. JV curves of ball milled brookite cells

Table 22. Current density vs. voltage (J–V) data under 1 sun for DSSCs ballmilled brookite cells.

| Brookite cells | Voc/V | Jsc/mA cm$^{-2}$ | FF | η/% |
|---|---|---|---|---|
| **1** | 0.967 | 9.61 | 74.6 | 6.93 |
| **2** | 0.992 | 10.00 | 69.3 | 6.88 |
| **3** | 0.931 | 9.31 | 75.1 | 6.69 |
| **4** | 0.968 | 9.14 | 74.6 | 6.60 |
| **5** | 0.899 | 9.42 | 75.2 | 6.37 |

# DISCUSSION

## 6. $TiO_2$ Synthesis

The UV-$O_3$ powder cleaning method proved to be effective in removing organic compounds that still remain on the surface of $TiO_2$ after synthesis. Additionally, it was able to increase the density of -OH groups on the surface of the rutile and anatase crystalline phases, showing its great potential to enhance the current density of devices fabricated with these crystalline phases. This is because potentially more dye molecules, with suitable energy levels, can be adsorbed on this surface. Furthermore, the method presents a significant energy advantage compared to the high-temperature method since the energy required for cleaning is greatly minimized

### 6.1. Low-temperature DSSCs

In this section the performance of low-temperature devices is discussed.

#### 6.1.1. First part

In the first part of this work, paste A was used to discover a suitable formulation in the electrolyte to obtain low-temperature solar cells with good performance. The results obtained are discussed below.

Even after washing and air-drying, the powders retained some organic components, according to FTIR readings. Therefore, the surface cleaning of the $TiO_2$ nanoparticles is an

essential step. Because organic chemicals impede the bonding sites between $TiO_2$ nanoparticles and the ITO surface, they can have an impact on the formation of paste.

Furthermore, a $TiO_2$ coating containing organic compounds may lessen the amount of active sites that the dye can use to bind to the surface, which would decrease the dye loading. Because impurities operate as potential surface states that increase charge transport resistance and, consequently, electronic recombination as the electrons spend longer time in contact with the redox electrolyte solution, they may also impair the device's performance.

Both heat treatment and UV-$O_3$ treatment were used to clean the $TiO_2$ nanoparticles. The FTIR spectra showed that the surface of the powders that had undergone heat treatment was cleaner. It is demonstrated that -OH groups—which are crucial for the dye's adsorption to the $TiO_2$ surface—were also eliminated. It is imperative to create techniques that use less energy. Consequently, considering its potential for low cost and time savings, investigating UV-$O_3$ for powder cleaning seems promising.

By adding $H_2TiF_6$ as an interparticle "binding" agent, an aqueous paste was created at low temperature—a maximum of 120 °C—without the need for organic binders. Film deposition demonstrated that the adhesion on the ITO substrate was sufficient.

We created three distinct electrolytes by varying the ratios of the solvents (ACN:VN, VA:ACN, and MN). Tests were conducted on both rigid and flexible devices under conventional irradiation settings (100 mW/cm$^2$, AM 1.5G).

Different electrolyte solvent compositions resulted in varying efficiency, as the manufactured devices showed. The average and standard deviation of all configurations evaluated under one sun are summarized in Table 6, which will be the basis for the subsequent study. Under one sun, the efficiencies of rigid devices made with VN:ACN, ACN:VN, and MN were 2.49 ± 0.11%, 1.73 ± 0.16%, and 1.63 ± 0.15%, respectively.

The characteristics of the used solvents are responsible for the variances in the results that were found. With increasing solvent viscosity, the order of acetonitrile, valeronitrile, and 3-methoxypropionitrile is first observed. The viscosity of the electrolytes is therefore anticipated to follow an increasing order of ACN:VN < VN:ACN < MN. As the viscosity increases in the acetonitrile/valeronitrile mixture, $J_{SC}$ rises from 3.85 ± 0.28 to 6.6 ± 0.29 mA $cm^{-2}$, demonstrating the intricate relationship between the current and viscosity. On the other hand, the 3-methoxy propionitrile has an even higher viscosity; in this instance, the current decreases to 5.08 ± 0.51 mA $cm^{-2}$.

While simultaneously imposing restrictions on the electronic transport phenomena inside the $TiO_2$ crystalline network, the integration of different electrolyte formulations may change the rate of electron injection to the $TiO_2$ conduction band or dye renewal by the redox shuttle species [187]. The ion diffusion inside the electrolyte is directly impacted by the solvent's viscosity; a higher viscosity typically results in a lower photocurrent because of the redox shuttle's mass transport restrictions, which in turn affects the dye regeneration kinetics [78][188][189].

This shows that using the traditional ACN:VN solvent mixture at an 85:15 ratio hinders the achievement of efficient electrical injection when using the low-temperature N719-sensitized film; the VN:ACN system performs better. A slight positive shift of $TiO_2$'s conduction band edge [190] in relation to an increase in viscosity, or a different arrangement of species within the electrolyte, may be the cause of the increase in short-circuit photocurrent from 3.85 ± 0.28 to 6.60 ± 0.29 mA $cm^{-2}$. This can be inferred from the small decrease in $V_{OC}$ that followed the increase in photocurrent.

On the other hand, the MN electrolyte solution's increased electrolyte viscosity significantly slows down ionic diffusion to impact dye molecule renewal, as evidenced by the decline in $J_{SC}$. Nevertheless, the MN solvent shows a marginally higher photocurrent than the ACN:VN solvent system, indicating that for this low-temperature system, a higher electrolyte viscosity may contribute favorably to the dye's electron injection into the $TiO_2$ conduction band. Still, it's clear that there's a perfect viscosity ratio. As the viscosity increases from 0.73 ± 0.01, 0.72 ± 0.01 to 0.55 ± 0.01 V for ACN:VN, VN:CAN, and MN, respectively, there is a discernible downward trend in the $V_{OC}$. It is widely recognized that the electrolyte configuration of ACN:VN can reduce recombination, thus improving the $V_{OC}$ and FF of a device [191].

When comparing ACN:VN with VN:ACN devices, a little drop in $V_{OC}$ of about 10 mV is seen. Given that an enhanced $J_{SC}$ is predicted to result in a larger electron density in the conduction band, this suggests that the viscosity increase may also have a minor boosting

influence on electronic recombination in VN:ACN devices. A more noticeable drop in $V_{OC}$ is shown in the case of MN devices. In this sense, the absence of chemicals in the formulation of MN electrolyte distinguishes it significantly from ACN:VN and VN:CAN combinations. The primary justification for employing MN electrolyte is its compatibility with low-temperature designs, as previously shown, and the positive outcomes that come from utilizing it consistently [102][192].

The key component of improving PV performance is additives. They have a significant impact on raising the $V_{OC}$ through reducing recombination kinetics and simultaneously causing changes in the band edges' energy [190][193][194]. When comparing ACN:VN devices to MN devices, there is a noticeable 180 mV dip, making it easy to see this effect. Due to a series resistance, carrier diffusion in the electrolyte might affect the FF in a DSSC. [14]. The ACN:VN devices obtained the best FF value of 0.58 ± 0.02, as can be seen. Electron injection from the dye to the $TiO_2$ conduction band appears to be limited in this arrangement. Compared to VN:ACN and MN configurations, this could lead to a longer time for the oxidized species in the electrolyte to regenerate fewer dye molecules, thus avoiding charge transfer problems. The FF for VN:ACN is significantly less, at 0.52 ± 0.01, in this instance.

This might be the result of a more viscous solvent mixed with better electronic injection. Higher current flow may cause a more dramatic difference in ion concentration, which could affect ionic diffusion more [195], making ion transport problems more apparent. Interestingly, MN showed an FF of 0.58 ± 0.01, which was quite similar to ACN:VN's. In this system, the rate of ionic diffusion seems to be more advantageous as viscosity rises. A

well-balanced ion concentration and optimal charge-carrier diffusion within the electrolyte may be facilitated by the slower electron injection rate and slower diffusion seen in this system as compared to VN:ACN. Keep in mind that the recombination kinetics and mechanism, which can vary greatly depending on the solvent, also have an impact on the FF. Even after post-heat treatments, organic molecules can still be seen on the surface of $TiO_2$, as seen by the FTIR spectra.

By acting as surface states, these substances can hinder effective electronic transport within the nanomaterial [22]. This variable may have an adverse effect by placing limitations on the photocurrent displayed by the devices, hence impeding improved performance. On an ITO-coated PEN substrate, a DSSC with the ideal electrolyte configuration was created. Under one sun, the FDSSC produced an efficiency of 1.0%. A $V_{OC}$ of 0.67 ± 0.01 V was observed in FDSSCs, indicating the possibility of some recombination in this system.

However, the $V_{OC}$ of the flexible DDSSC devices was more than that of the inflexible MN devices, offering more evidence of the improved suitability of the VN:ACN composition for the low-temperature system. In comparison, FDSSC devices showed a $J_{SC}$ of 2.73 ± 0.11 mA $cm^{-2}$, which is lower than any other systems. However, as VN:ACN devices showed, the FF of 0.54 ± 0.43 remained very close to the expected value for this system. Lastly, tests were conducted at 1000 lux using an interior light simulator on both rigid and flexible VN:ACN devices.

Table 9, which presents the average and standard deviation of rigid and FDSSCs evaluated in low-light simulations, will be used for the next study. FF maintained roughly the same value of 0.45 ± 0.01 and 0.47 ± 0.01, respectively, but the $V_{OC}$ of both devices is dramatically different, measuring 0.53 ± 0.01 V for ITO-coated glass devices and 0.46 ± 0.01 V for ITO-coated PEN devices. When it comes to $J_{SC}$, the difference is noticeably larger. The photocurrent of devices made on glass substrates was nearly twice as high as that of devices made on FPCSs, with values of 16.67 ± 0.63 and 34.70 ± 0.61 μA $cm^{-2}$, respectively. For the stiff and flexible devices, maximum power results were 8.52 ± 0.13 and 3.80 ± 0.17 μW $cm^{-2}$, respectively.

### 6.1.2. Second part

Although the films deposited in the first part of this work from the low-temperature paste demonstrated sufficient mechanical stability, further research is needed to explore the incorporation of suitable low-temperature methods to enhance this aspect while remaining compatible with large-scale production processes.

At a macroscopic level, the films made with paste A exhibited good adherence to the flexible ITO substrate. However, upon closer examination under SEM, both micro and macro cracks were observed, compromising the performance of the solar cell by reducing the surface area for dye molecule adsorption. Additionally, this leads to a significant problem in electronic transport within the crystal lattice due to the loss of connection between particles. Another

disadvantage this may cause is promoting greater electrolyte infiltration to the ITO surface, leading to easier electron recombination.

In the second part of this work, efforts were made to improve the properties of the low-temperature paste by enhancing particle dispersion to achieve a homogeneous film and to enhance paste transparency while reducing film thickness to improve electronic diffusion distance. For this purpose, a different assembly method was utilized in fabricating the devices in this section, allowing for a reduction in the distance between electrodes to facilitate ionic diffusion in the electrolyte.

The utilization of an organic dye with a high molar extinction coefficient holds promise for enhancing the performance and efficiency of ultra-thin-film systems. These organic dyes, characterized by bulky ligands modifying the chemical environment of the redox couple near the $TiO_2$ surface, may minimize recombination. In the second part of this work, the organic dye Y123 was used in conjunction with the copper redox pair, as these two elements have shown to produce high-efficiency cells when working together.

Films prepared with paste B demonstrated similar adherence behavior to the flexible ITO substrate. Ball milling proved to be more effective in breaking agglomerates and producing a film with higher transparency. The distribution of agglomerates in the film was significantly reduced. This allowed the film deposited with this paste to achieve a homogeneous thickness along the ITO.

Although the low-temperature pastes were prepared using different methodologies, all demonstrated the capability of interconnection between particles and good adherence to the ITO surface on the flexible plastic substrate, demonstrating the effectiveness of $H_2TiF_6$ acid.

The acid is only effective in the colloidal solution when there is an adequate concentration to create bonds between particles since it was observed that a highly diluted aqueous solution of $TiO_2$ does not change from liquid to solid consistency, nor does it adhere to the substrate.

Regarding paste C, with the concentration and consistency obtained, a maximum thickness of 1.7 μm could be achieved. This was made possible by the addition of TIIP, which completely changed the consistency of the liquid colloid to a viscous solution. This could be because TIIP, upon contact with water, breaks down the alkoxides, and the presence of acid in the water, small $TiO_2$ molecules could be functioning as a kind of extra nano glue that allows larger particles in the solution to bond together. Additionally, it could aid in breaking down any remaining agglomerates in the colloidal solution, resulting in a highly stable viscous solution.

However, when attempting to deposit thicknesses greater than this, the films were more prone to delamination and detachment from the ITO surface, so one way to increase the film thickness, up to 4-6 μm, could be to explore the preparation of a colloidal solution of higher concentration and conduct a study of the amount of TIIP necessary to maintain particle connection. Another alternative for the fabrication of low-temperature DSSCs with better performance would be to combine pastes with not-so-large agglomerates like those presented

by paste B along with the properties of a paste that provides better particle connection and transparency like that provided with paste C to obtain a suitable pore size for the utilization of a copper electrolyte.

The devices fabricated with paste C, using Y123 dye and copper electrolyte, show a clear trend of low efficiency compared to devices fabricated with Y123 dye and iodide electrolyte. This is largely due to the compact film, which presents a greater challenge in dye regeneration due to slower ionic diffusion.

Paste C, compared to the commercial paste, exhibits the expected behavior for a viscous paste. However, in the viscosity vs. shear stress graph, the behavior of low-temperature aqueous paste is an order of magnitude below the viscosity of the commercial paste. This provides important information as the aim in preparing a low-temperature paste is to implement it for use in the screen printing deposition method. In this regard, a study of the material concentration used in the paste and its effect on paste viscosity to improve deposition uniformity and film quality would be necessary. Optimizing the viscosity of the low-temperature paste is vital for the preparation of low-temperature films for flexible DSSCs.

The appearance of Paste A presented an opaque appearance, revealing the presence of substantial agglomerates within the film. These significant agglomerates may pose challenges by acting as points of light dispersion, impeding the transmission of light through the film, which can be observed through transmittance measurements in section 5.15. Consequently, paste B was devised to mitigate the agglomeration issue. With this paste, film

transparency could be significantly improved, however, the film still presented micro and macro cracks resulting in difficulty in electronic transport within the crystal lattice due to the lack of connection between particles. Film transparency could be improved by using $TiO_2$ particles directly from synthesis as they are already hydrated and well dispersed in a liquid medium, and by adding TIIP, it was possible to significantly improve particle interconnection, allowing for the production of a transparent film with good adherence to the flexible plastic substrate that can be chemically sintered at 120 °C, representing a significant energy advantage. It should be noted that the thickness of the films deposited using paste A obtained an approximate thickness of between 9 and 6 μm, films deposited with paste B obtained an approximate thickness of 6.5 μm, and films deposited with paste C an approximate thickness of 1.7 μm, so the transmittance values obtained in section 5.15 should be handled with care.

It was observed that films prepared with paste C using TIIP as an additive showed to have a better dye adsorption on the surface of the $TiO_2$. In this regard, based on the SEM images of this deposits and the transparency of these films it is evident that the higher dye adsorption was induced by the better dispersión of the particles in solution rendering the films with a high surface area since there are much less presence of big agglomerates rather than incrreasing -OH anchoring groups to the surface of the nanoparticles.

The method employed to assemble DSSCs using UV-curable adhesive surpasses the commonly used approach with melted plastic frames, as it enables a reduction in the distance

between electrodes, facilitating faster charge transport. Additionally, the use of a special resin for plastics allowed the manufactured cells to remain attached when bending the device.

The devices manufactured using paste B, Y123 dye, and copper electrolyte presented low efficiencies ranging from 0.30 to 0.60%. It can be observed from the photovoltaic parameters in the table that the voltage is high, which is representative of the copper redox pair; however, the current is very low. Remarkably, the cells that used the iodide electrolyte had a much higher efficiency compared to those that used the iodide electrolyte, ranging from 1.46 to 1.58%. In this case, it can be observed that the Voc is lower than the copper cells, however, the current is higher, as well as the FF.

Subsequently, cells fabricated with paste C and using copper electrolyte demonstrated better efficiencies compared to those fabricated with paste B. Overall, all photovoltaic parameters were favored, although the efficiencies only managed to stay in the range of 0.95 to 1.07%.

Cells fabricated with paste C and using the optimal iodide configuration found in the first part of this work showed higher efficiencies compared to cells fabricated with paste B. The increase in efficiency, ranging from 1.95 to 2%, is mainly due to the significant increase in current density. The efficiencies of this paste remain below those obtained with devices fabricated with paste A; however, it is important to mention that the thickness of the paste C film is much less compared to that of the devices fabricated with paste A, which demonstrates great potential for improving the efficiencies of these devices.

Using this optimal paste formulation, flexible solar cells were fabricated. The films deposited on flexible substrates exhibited good adherence and transparency. The manufactured cells presented an efficiency ranging from 1.18 to 1.33%, which is lower compared to the devices fabricated on ITO-Glass; however, they are approximately 33% below the efficiency. This is significant when comparing flexible devices fabricated with paste A, which are approximately 40% below the efficiency of their respective pairs on flexible substrates. The FF of the flexible cells appears to be the main factor in reducing efficiency.

These devices fabricated with paste C were also characterized under low-intensity conditions. On this occasion, the solar simulator used was previously calibrated, so the irradiance generated by the lamps is known and it was possible to calculate efficiency. The devices fabricated using the iodide electrolyte demonstrated efficiencies ranging from 6.52 to 6.82%, while devices using the copper electrolyte ranged from 4.49 to 4.0%. The flexible cells demonstrated an efficiency of between 3.80 to 4.42%, less than their rigid counterparts.

For the cells fabricated with the paste C, Y123 dye and copper electrolyte, it can be observed that the third semicircle is visible in the lower frequencies. This is a strong indicative that there are problems with the ionic diffusion inside the electrolyte. One of the main reasons is because the low-temperature film have a too small pore size which make it hard for the copper redox coupe to move since it is a big molecule. The second semicircle is smaller than the third onde at middle frequencies, which suggest that the diffusion problems are more pronounced than the electronic recombination.

For cells manufactured with paste C, Y123 dye, and iodide electrolyte, it can be observed that the third semicircle also appears; however, does not exhibit as strong an imaginary impedance component as devices using a copper electrolyte. This indicates that, although there is an electronic diffusion problem, it is of lesser magnitude because the iodide molecule is smaller, and despite the compact film, it does not have as significant an effect as in the case of copper cells. This becomes evident when comparing the JV curves of these devices, where the current density is higher in copper devices, suggesting better regeneration of dye by the iodide redox pair. In the case of devices using the iodide electrolyte, the second semicircle becomes more prominent at medium frequencies compared to the third, suggesting stronger recombination effects between $TiO_2$ and the electrolyte. Moreover, the first semicircle at high frequencies for these devices has a higher imaginary impedance component compared to cells manufactured with the copper electrolyte.

### 6.2. High-performance DSSCs

In this section, high-performance DSSCs were fabricated to demonstrate the feasibility of using low-temperature paste preparation methods for high-temperature regimes as well. In this regard, an anatase paste was prepared using particles directly from synthesis, similar to those used in paste C. However, the demonstrated efficiency was significantly lower than efficiencies obtained with commercial paste. To improve DSSC performance, a paste was prepared using the method employed for paste B. Surprisingly, device efficiencies increased significantly, reaching efficiencies comparable to those of cells using commercial paste. The results of this section are analyzed below.

High-performance DSSCs fabricated with commercial paste and anatase paste demonstrated a similar thickness of 4 μm, unlike brookite films that exhibited irregular morphology, as observed in SEM images.

The rheology of prepared pastes showed they were at least 2 orders of magnitude below commercial paste, indicating an opportunity area for improving paste quality.

Dye desorption tests showed that the synthesized anatase film had the highest dye adsorption on its surface compared to commercial paste due to its smaller particle size, which provides a larger surface area. Conversely, dye adsorption was lower in the brookite film due to its larger particle size, which reduces the surface area.

Cells fabricated with A-synth paste achieved efficiencies ranging from 4.94 to 6.58%, significantly lower than reference cell efficiencies of 9.3 to 9.8%. However, changing particle processing methods notably increased efficiency to values between 8.2 and 9.61%, demonstrating that in this case, the appearance of clusters in the paste had a positive impact by increasing pore volume, allowing copper redox pairs to diffuse through the porous film. Additionally, having smaller particle size than commercial paste compensates for dye adsorption on the surface. Cells fabricated with brookite demonstrated efficiencies ranging from 6.37 to 6.93%, lower than efficiencies obtained with anatase particles from A-Bmill paste but even higher than those fabricated with A-synth paste. This could be due to the larger particle size of brookite, as observed in SEM images, where overly large pores within the

film indicate that the poor performance of cells fabricated with A-synth paste was due to the compactness of the film resulting from a very small pore size.

# CONCLUSIONS

In this work, three crystalline phases of $TiO_2$ were synthesized and applied in DSSCs. Anatase and rutile were synthesized by modifying the pH conditions of the synthesis. These particles were used to prepare low-temperature pastes for flexible solar cells. The brookite phase was synthesized from amorphous $TiO_2$ and was used, along with the anatase particles, for the fabrication of high-performance DSSCs.

For the fabrication of a low-temperature DSSC, a mechanically stable, homogeneous film was found through the study of the colloidal properties of dispersion and the utilization of new and cutting-edge componentes and methods. An aqueous binder free paste with high transparency was prepared and deposited on both rigid and FPCSs by doctor blading without any additional sintering treatment.

It was demonstrated that avoiding the particles to dry it could be achieved the reduction of nanoparticles agglomeration which with a stable coloid that produce homogenous films with high transparency and low film thickness which is one of the main features that must be accomplished for flexible DSSC. In addition, this method for the processing and preparation of these pastes renders an easy reproducible method for large-scale manufacturing processes. According to the SEM images, It can be say that the $TiO_2$ powders tend to get compact and form massive agglomerates when they are air dried. This phenomenon can be either negative or positive for its use in DSSC. These findings demonstrate the high quality of the deposited film, supporting its suitability for future applications

The manufactured devices were measured for both outdoor and indoor conditions, obtaining promising results. This demonstrates its potential for future applications and underlines its suitability for further research and exploration.

For high-temperature DSSCs, it was evident that the particle size hinders the operation of a high-performance DSSC since, despite increasing the surface area, the pore size is decreased, which directly affects the ionic diffusion of large copper molecules. Therefore, it was demonstrated that agomerates formed with small particles can act positively in the system, managing to increase the pore size at the same time that the surface area increases, making the adsorption of more dye molecules possible and at the same time increasing the surface area. once more current generation.

In this work, we attribute this behavior to the quality of the ITO on the surface of the FPCS, as well as any potential drawbacks that may arise during the fabrication process of these devices, such as possible electrolyte leaks. It was demonstrated that washing the substrates following the utilized protocol increased the surface energy of the substrate, rendering it more hydrophilic. This effect improved the proper spreading of the waterbased paste upon deposition, leading to improved adherence to the substrate. However, owing to the fragile nature of the ITO layer on the PEN substrate as well as the acidity of the paste (pH = 2) this could have resulted in damaging the layer and losing electronic contact sites between $TiO_2$ and ITO and, thus, yielding a lower efficiency compared to rigid devices.

Two key factors account for the lower photoelectric performance observed in low temperature methods. Firstly, it can be attributed to the inadequate interparticle connection of $TiO_2$ impeding efficient electron transport [196], consequently limiting the overall device performance. Secondly, an unsatisfactory electrical connection between $TiO_2$ and ITO is evident, leading to an increase in series resistance. This additional resistance impedes the captured electrons from generating optimal electrical work, directly impacting the efficiency and performance of the solar cells [123].

In both high-intensity and low-intensity measurements, the FDSSCs exhibited lower performance compared to rigid devices. Under low-light conditions, the photoinduced electron transfer exhibits a notable reduction in comparison to high-intensity illumination in solar cells, attributable to the low photon flux [190]. The dependency of solar cell output power on the spectral composition of the incoming light is a widely recognized phenomenon [197][198]. At low light intensities, minimizing recombination processes becomes a major task. It is crucial to optimize the compact layer to prevent unwanted interaction between the TCO/electrolyte interface while simultaneously facilitating effective electrical contact between the $TiO_2$ film and the TCO [57].

# PERSPECTIVES

For future work, a low temperature blocking layer could be explored to avoid electronic recombination between the ITO films and the electrolyte. This takes on great relevance because this would allow copper electrolytes to be used, avoiding the presence of high recombination that it presents. Also in conjunction with this, the use of paste A could be explored as a low temperature dispersion paste on top of paste C that functions as a transparent active layer since paste A was shown to possess low transmittance but also maintain sufficient injection. electronics with which low temperature devices could take advantage of the light that could be wasted.

## BIBLIOGRAPHY


[1] Kim, M.B.; Han, H.G.; Roh, D.H.; Park, J.; Kim, K.M.; Kim, U.Y.; Kwon, T.H. Flexible Dye-Sensitized Solar Cells. In Flexible Energy Conversion and Storge Devices, 1st ed.; Zhi, C., Dai, L., Eds.; Wiley-VCH Verlag GmbH & Co.: Weinheim, Germany, 2018; pp. 239–281.

[2] Mozaffari, S.; Nateghi, M.R.; Zarandi, M.B. An overview of the Challenges in the commercialization of dye sensitized solar 1362 cells. Renew. Sustain. Energy Rev. 2017, 71, 675–686.

[3] Mahalingam, S.; Abdullah, H. Electron transport study of indium oxide as photoanode in DSSCs: A review. Renew. Sustain. Energy Rev. 2016, 63, 245–255.

[4] Baby, R.; Nixon, P.D.; Kumar, N.M.; Subathra, M.S.P.; Ananthi, N. A comprehensive review of dye-sensitized solar cell optimal fabrication conditions, natural dye selection, and application-based future perspectives. Environ. Sci. Pollut. Res. 2022, 29, 371–404.

[5] Gong, J.; Sumathy, K.; Qiao, Q.; Zhou, Z. Review on dye-sensitized solar cells (DSSCs): Advanced techniques and research trends. Renew. Sustain. Energy Rev. 2017, 68, 234–246.

[6] Pugalendhi, S., Gitanjali, J., Shalini, R., Subramanian, P. 1st ed. Handbook on Renewable Energy and Green Technology. CRC Press. 2024, pp 218. ISBN: 978-1-394-17480-5.

[7] Mondal, S., Kumar, A., Pachauri, R. K., Mondal, A. K., Singh, V. K., Sharma, A. K. 1st ed. Clean and Renewable Energy Production. Wiley. 2024, pp 560. ISBN: 978-1-394-17480-5.

[8] Haque, A., Kalam, A., Sharma, H. Smart Cities: Power electronics, Renewable Energy, and Internet of Things. CRC Press. 2024, pp. 337. ISBN: 1032669780.

[9] Duffie, J., Beckman, W., Blair, N. Solar Engineering of Thermal Processes, Photovoltaics and Wind. 5th ed. Wiley. 2020, pp. 928. ISBN: 1119540283.

[10] Goetzberger, A., Hoffmann, V. U., Photovoltaic Solar Energy Generation. 2005th ed. Springer. 2005, pp. 246. ISBN: 3540236767.

[11] Gueymard, C. A. A reevaluation of the solar constant based on a 42-year total solar irradiance time series and a reconciliation of spaceborne observations. Solar Energy. 2018. 168, 2–9.

[12] Li, G., Sheng, L., Li, T., Hu, J., Li, P., Wang, K. Engineering flexible dye-sensitized solar cells for portable electronics. Solar Energy. 2019. 177, 80-98.

[13] Dittrich, T. Materials Concepts for Solar Cells. 2nd ed. World Scientific. 2018, pp. 568. ISBN: 1786346370

[14] Wu, I., Lan, Z., Lin, J., Huang, M., Huang, Y., Fan, L., Luo, G. Electrolytes in Dye-Sensitized Solar Cells. Chemical Reviews. 2015. 115 (5), 2136-2173.

[15] Bella, F., Bongiovanni, R. Photoinduced polymerization: An innovative, powerful and environmentally friendly technique for the preparation of polymer electrolytes for dye-

sensitized solar cells. Journal of Photochemistry and Photobiology C: Photochemistry Reviews. 2013. 16, 1-21.

[16] Al-Ezzi AS, Ansari MNM. Photovoltaic Solar Cells: A Review. Applied System Innovation. 2022; 5(4):67.

[17] Kodigala, Subba R. Introduction. Thin Films and Nanostructures, vol. 35, 2010, pp. 1-19.

[18] Tiwari, G. N., Dubey, S. Fundamentals of Photovoltaic Modules and their Applications. 1st ed. Royal Society of Chemistry. 2009, pp. 424. ISBN: 1849730202.

[19] Hashmi, G.; Miettunen, K.; Peltola, T.; Halme, J.; Asghar, I.; Aitola, K.; Toivola, M.; Lund, P. Review of materials and manufacturing options for large area flexible dye solar cells. Renew. Sustain. Energy Rev. 2011, 15, 3717–3732.

[20] Li, B.; Huang, F.; Zhong, J.; Xie, J.; Wen, M.; Pen, Y. Fabrication of Flexible Dye-Sensitized Solar Cell Modules using Commercially Available Materials. Energy Technol. 2016, 4, 536–542.

[21] Freitag, M.; Teuscher, J.; Saygili, Y.; Zhang, X.; Giordano, F.; Liska, P.; Hua, J.; Zakeeruddin, M.; Moser, J.E.; Grätzel, M.; et al. Dye-sensitized solar cells for efficient power generation under ambient lighting. Nat. Photon. 2017, 11, 372–378.

[22] Pichot, F.; Pitts, J.R.; Gregg, B.A. Low-temperature sintering of TiO2 colloids: Application to flexible dye-sensitized solar cells.Langmuir 2000, 16, 5626–5630.

[23] Karthick, S.N.; Hemalatha, K.V.; Balasingam, S.K.; Clinton, F.M.; Akshaya, S.; Kim, H. Dye-Sensitized Solar Cells: History, Components, Configuration, andWorking

Principle. In Interfacial Engineering in Functional Materials for Dye-Sensitized Solar, 1st ed.; Pandikumar, A., Jothivenkatachalam, K., Bhojonaa, K.B., Eds.; Jhon Wiley & Sons: New York, NY, USA, 2020; pp. 1–16.

[24] Ahmad, S, K., Naqvi, N, S., Jaffri, S, B. Systematic review elucidating the generations and classifications of solar cells contributing towards environmental sustainability integration. Reviews in Inorganic Chemistry. 2021. 41, 1. pp. 21-39.

[25] Li, M.; Igbari, F.; Wang, Z.K.; Liao, L.S. Indoor Thin-Film Photovoltaics: Progress and Challenges. Adv. Energy Mater. 2020, 10, 2000641.

[26] Lye, Y., Chan, K., Ng, Z. A Review on the Progress, Challenges, and Performances of Tin-Based Perovskite Solar Cells." Nanomaterials. 13, 3, 2023, p. 585.

[27] Wu, I., Lan, Z., Lin, J., Huang, M., Huang, Y., Fan, L., Luo, G. Materials for Photovoltaics: Overview, Generations, Recent Advancements and Future Prospects. IntechOpen. 2022, pp. 112. ISBN: 978-1-83969-906-1.

[28] Dambhare, M. V., Butey, B., Moharil, S. V. Solar photovoltaic technology: A review of different types of solar cells and its future trends. Journal of Physics: Conference Series. 2021. 1913, 012053.

[29] Kurinec, S., Emerging Photovoltaic Materials. 1st ed. Wiley. 2019, pp. 1105. ISBN: 978-1119407546

[30] Yang, D. Handbook of Photovoltaic Silicon. Springer. 2020, pp 967. ISBN: 978-3-662-56471-4.

[31] Vijayan, K., Vijayachamundeeswari, S., Sivaperuman, K., Ahsan, N., Logu, T., Okada, Y. A review on advancements, challenges, and prospective of copper and non-copper based thin-film solar cells using facile spray pyrolysis technique. Solar Energy. 2022. 234, 81-102.

[32] Pastuszak, J., Węgierek, P. Photovoltaic Cell Generations and Current Research Directions for Their Development. Materials. 2022. 15(16), 5542.

[33] Sivaraj, S., Rathanasamy, R., Kaliyannan, G. V., Panchal, H., Jawad Alrubaie, A., Musa Jaber, M., Said, Z., Memon, S. A Comprehensive Review on Current Performance, Challenges and Progress in Thin-Film Solar Cells. Energies. 2022. 15(22), 8688.

[34] Razykov, T., Ferekides, C., Morel, D., Stefanakos, E., Ullal, H., Upadhyaya, H. Solar photovoltaic electricity: Current status and future prospects. Solar Energy. 2011. 85(8), 1580-1608.

[35] Hamakawa, Y. Thin-Film Solar Cells: Chapter 1: Background and Motivation for Thin-Film Solar-Cell Development. Springer. 2004. ISBN: 978-3-642-07879-8.

[36] Conibeer, G. Third-generation photovoltaics. Materials Today. 2007. 10(11), 42-50.

[37] James, S.; Contractor, R. Study on Nature-inspired Fractal Design-based Flexible Counter Electrodes for Dye-Sensitized Solar Cells Fabricated using Additive Manufacturing. Sci. Rep. 2018, 8, 17032.

[38] Yan, J.; Saunders, B.R. Third-generation solar cells: A review and comparison of polymer: fullerene, hybrid polymer and perovskite solar cells. RSC Adv. 2014, 4, 43286.

[39] Mingsukang, M.A.; Buraidah, M.H.; Arof, A.K. Third-Generation-Sensitized Solar Cells. In Nanostructured Solar Cells, 1st ed.; Das,N., Ed.; InTechOpen: London, UK, 2017; pp. 7–31.

[40] Buitrago, E.; Novello, A.M.; Meyer, T. Third-Generation Solar Cells: Toxicity and Risk of Exposure. Helv. Chim. Acta 2020, 103, 9.

[41] George, J.; Joseph, A.P.; Balachandran, M. Perovskites: Emergence of highly efficient third-generation solar cells. Int. J. Energy Res. 2022, 46, 21856–21883.

[42] Zdyb, A. Third Generations Solar Cells. 1st ed. 2023, pp. 150. ISBN: 1032052554

[43] R. Avilés-Betanzos, G. Oskam, D. Pourjafari. Low-Temperature Fabrication of Flexible Dye-Sensitized Solar Cells: Influence of Electrolyte Solution on Performance under Solar and Indoor Illumination. 2023. Energies. 16, 15.

[44] National Renewable Energy Laboratory. Available online: https://www.nrel.gov/pv/cell-efficiency.html (accessed on 20 April 2024).

[45] Ellis, H.; Vlachopoulos, N.; Häggman, L.; Perruchot, C.; Jouini, M.; Boschloo, G.; Hagfeldt, A. PEDOT counter electrodes for dye-sensitized solar cells prepared by aqueous micellar electrodeposition. Electrochim. Acta 2013, 107, 45–51.

[46] Lin, L.Y.; Ho, K.C. Dye-sensitized solar cells. In Encyclopedia of Modern Optics, 2nd ed.; Guenther, B.D., Steel, D.G., Eds.; Elsevier Inc.: Amsterdam, The Netherlands, 2018; Volume 5, pp. 270–281.

[47] Ito, S. Investigation of Dyes for Dye-Sensitized: Ruthenium-Complex Dyes, Metal-Free Dyes, Metal-Complex Porphyrin Dyes. In Solar Cells—Dye-Sensitized Devices, 1st ed.; Kosyachenko, L.A., Ed.; InTechOpen: London, UK, 2011; pp. 19–48.

[48] Grätzel, M. Photoelectrochemical cells. Nature. 2001. 414(6861), 338-344.

[49] Shen, J.; Cheng, R.; Chen, Y.; Chen, X.; Sun, Z.; Huang, S. A Novel TiO2 Tape for Fabricating Dye-Sensitized Solar Cells on Universal Conductive Substrates. ACS Appl. Mater. Interfaces 2013, 5, 13000–13005.

[50] Ren, Y., Zhang, D., Suo, J., Cao, Y., Eickemeyer, F. T., Vlachopoulos, N., Zakeeruddin, S. M., Hagfeldt, A., Grätzel, M. Hydroxamic acid pre-adsorption raises the efficiency of cosensitized solar cells. Nature. 2023. 613 (7942), 60-65.

[51] Park, N.G.; Kim, K.M.; Kang, M.G.; Ryu, K.S.; Chang, S.H.; Shin, Y.J. Chemical Sintering of Nanoparticles: A Methodology for Low-Temperature Fabrication of Dye-Sensitized $TiO_2$ Films. Adv. Mater. 2005, 17, 2349–2353.

[52] Nogueira, A.F.; Longo, C.; De Paoli, M.A. Polymers in dye sensitized solar cells: Overview and perspectives. Coord. Chem. Rev. 2004, 248, 1455–1468.

[53] Hagfeldt, A.; Boschloo, G.; Lindström, H.; Figgemeier, E.; Holmberg, A.; Aranyos, V.; Magnusson, E.; Malmqvist, L. A system approach to molecular solar cells. Coord. Chem. Rev. 2004, 248, 1501–1509.

[54] Lindström, H.; Holmberg, A.; Magnusson, E.; Lindquist, S.E.; Malmqvist, L.; Hagfeldt, A. A New Method for Manufacturing Nanostructured Electrodes on Plastic Substrates. Nano Lett. 2001, 1, 97–100.

[55] Li, M.; Igbari, F.; Wang, Z.K.; Liao, L.S. Indoor Thin-Film Photovoltaics: Progress and Challenges. Adv. Energy Mater. 2020, 10, 2000641.

[56] Kim, S.; Jahandar, M.; Jeong, J.H.; Lim, D.C. Recent Progress in Solar Cell Technology for Low-Light Indoor Applications. Curr. Altern. Energy 2019, 3, 3–17.

[57] Michaels, H.; Rinderle, M.; Freitag, R.; Benesperi, I.; Edvinsson, T.; Socher, R.; Gagliardi, A.; Freitag, M. Dye-sensitized solar cells under ambient light powering machine learning: Towards autonomous smart sensors for the internet of things. Chem. Sci. 2020, 11, 2895–2906.

[58] Zhang, D.; Stojanovic, M.; Ren, Y.; Cao, Y.; Eickemeyer, F.T.; Socie, E.; Vlachopoulos, N.; Moser, J.-E.; Zakeeruddin, S.M.; Hagfeldt, A.; et al. A molecular photosensitizer achieves a $V_{OC}$ of 1.24 V enabling highly efficient and stable dye-sensitized solar cells with copper(II/I)-based electrolyte. Nat. Commun. 2021, 12, 1777.

[59] Cao, Y.; Liu, Y.; Zakeeruddin, S.M.; Hagfeldt, A.; Grätzel, M. Direct Contact of Selective Charge Extraction Layers Enables High-Efficiency Molecular Photovoltaics. Joule 2018, 2, 1108–1117.

[60] Karim, N.A.; Mehmood, U.; Zahid, H.F.; Asif, T. Nanostructured photoanode and counter electrode materials for efficient Dye-Sensitized Solar Cells (DSSCs). Sol. Energy. 2019, 185, 165–188.

[61] Wu, T.-C.; Huang, W.-M.; Meen, T.-H.; Tsai, J.-K. Performance Improvement of Dye-Sensitized Solar Cells with Pressed $TiO_2$ Nanoparticles Layer. Coatings. 2023, 13, 907.

[62] Landmann, M., Rauls, E., Schmidt, W. G. The electronic structure and optical response of rutile, anatase and brookite $TiO_2$. Journal of Physics Condensed Matter. 2012, l, 24, 195503.

[63] Li, G., Fang, K., Ou, Y., Yuan, W., Yang, H., Zhang, Z., Wang, Y. Surface study of the reconstructed anatase $TiO_2$ (001) surface. Progress in Natural Science: Materials International. 31(1), 1-13.

[64] El-Desoky, M. M., Morad, I., Wasfy, M. H., Mansour, A. F. Synthesis, structural and electrical properties of PVA/$TiO_2$ nanocomposite films with different $TiO_2$ phases prepared by sol–gel technique. Journal of Materials Science: Materials in Electronics. 2020, 31, 20, pp. 17574–17584.

[65] Chen, J., Guan, M., Zhang, X., Gong, X. Insights into a rutile/brookite homojunction of titanium dioxide: Separated reactive sites and boosted photocatalytic activity. RSC Adv. 2019, 9, 63. 36615–36620.

[66] Sahadat Hossain, M., Ahmed, S. Easy and green synthesis of $TiO_2$ (Anatase and Rutile): Estimation of crystallite size using Scherrer equation, Williamson-Hall plot,

Monshi-Scherrer Model, size-strain plot, Halder- Wagner Model. Results in Materials. 2023, 20, 100492.

[67] Subramanian, A., Wang, H. Effect of hydroxyl group attachment on $TiO_2$ films for dye-sensitized solar cells. Applied Surface Science. 2012, 258(20), 7833-7838.

[68] Richhariya, G., Kumar, A., Tekasakul, P., Gupta, B. Natural dyes for dye sensitized solar cell: A review. Renewable and Sustainable Energy Reviews. 2017, 69, 705-718.

[69] Carella, A., Borbone, F., Centore, R. Research Progress on Photosensitizers for DSSC. Frontiers in chemistry. 2018, 6, 481.

[70] Sen, A., Putra, M. H., Biswas, A. K., Behera, A. K., Groβ, A. Insight on the choice of sensitizers/dyes for dye sensitized solar cells: A review. Dyes and Pigments. 2023, 213, 111087.

[71] Etgar, L., Schuchardt, G., Costenaro, D., Carniato, F., Bisio, C., Zakeeruddin, S. M., Nazeeruddin, M. K., Marchese, L., Graetzel, M. Enhancing the open circuit voltage of dye sensitized solar cells by surface engineering of silica particles in a gel electrolyte. Journal of Materials Chemistry A. 2013, ,1, 10142-10147.

[72] J. Li *et al.*, "Efficient dye-sensitized solar cells with [copper(6,6′-dimethyl-2,2′-bipyridine)2]2+/1+ redox shuttle," *RSC Adv*, vol. 7, no. 8, pp. 4611–4615, 2017, doi: 10.1039/c6ra25676g.

[73] Shen, Z., Eickemeyer, F. T., Gao, J., Pfeifer, L., Bradford, D., Freitag, M., Zakeeruddin, S. M., Grätzel, M. Molecular engineering of low-cost, efficient, and stable photosensitizers for dye-sensitized solar cells. *Chem*. 2023, 9, 12, 3637–3647.

[74] Yella, A., Lee, H. W., Tsao, H. N., Yi, C., Chandiran, A. K., Nazeeruddin, M. K., Diau, E. W., Yeh, C. Y., Zakeeruddin, S. M., Grätzel, M. Porphyrin-sensitized solar cells with cobalt (II/III)-based redox electrolyte exceed 12 percent efficiency. Science (New York, N.Y.). 2011, 334(6056), 629–634.

[75] Qi, Q., Li, R., Luo, J., Zheng, B., Huang, K., Wang, P., Wu, J. Push–pull type porphyrin based sensitizers: The effect of donor structure on the light-harvesting ability and photovoltaic performance. Dyes and Pigments. 2015, 122, 199-205.

[76] Lindh, L., Gordivska, O., Persson, S., Michaels, H., Fan, H., Chábera, P., Rosemann, N. W., Gupta, A. K., Benesperi, I., Uhlig, J., Prakash, O., Sheibani, E., Kjaer, K. S., Boschloo, G., Yartsev, A., Freitag, M., Lomoth, R., Persson, P., & Wärnmark, K. Dye-sensitized solar cells based on Fe N-heterocyclic carbene photosensitizers with improved rod-like push-pull functionality. Chemical Science. 2021, 12, 16035-16053.

[77] Ebenezer Anitha, A.,Dotter, M. A Review on Liquid Electrolyte Stability Issues for Commercialization of Dye-Sensitized Solar Cells (DSSC). Energies. 2023, 16(13), 5129.

[78] Masud, N.; Kim, H.K. Redox Shuttle-Based Electrolytes for Dye-Sensitized Solar Cells: Comprehensive Guidance, Recent Progress, and Future Perspective. ACS Omega 2023, 8, 6139–6163.

[79] Iftikhar, H., Sonai, G. G., Hashmi, S. G., Nogueira, A. F., Lund, P. D. Progress on Electrolytes Development in Dye-Sensitized Solar Cells. Materials (Basel, Switzerland). 2019, 12(12), 1998.

[80] Zeng, K., Chen, Y., Zhu, W.-H., Tian, H., and Xi, Y. Efficient Solar Cells Based on Concerted Companion Dyes Containing Two Complementary Components: An Alternative Approach for Cosensitization. J. Am. Chem. Soc. 2020, 142, 11, 5154–5161.

[81] Saygili, Y., Söderberg, M., Pellet, N., Giordano, F., Cao, Y., Muñoz-García, A. B., Zakeeruddin, S. M., Vlachopoulos, N., Pavone, M., Boschloo, G., Kavan, L., Moser, J.-E., Grätzel, M., Hagfeldt, A., and Freitag, M. Copper Bipyridyl Redox Mediators for Dye-Sensitized Solar Cells with High Photovoltage. J. Am. Chem. Soc. 2016, 138, 45, 15087–15096.

[82] Benesperi, I., Michaels, H., Edvinsson, T., Pavone, M., Probert, M. R., Waddell, P., Muñoz-García, A. B., Freitag, M. Dynamic dimer copper coordination redox shuttles. Chem. 2022, 8(2), 439-449.

[83] Michaels, H., Golomb, M. J., Kim, B. J., Edvinsson, T., Cucinotta, F., Waddell, P. G., Probert, M. R., Konezny, S. J., Boschloo, G., Walsh, A., and Freitag, M. Copper coordination polymers with selective hole conductivity. J. Mater. Chem. A, 2022,10, 9582-9591.

[84] Spinelli, G., Morritt, G. H., Pavone, M., Probert, M. R., Waddell, P. G., Edvinsson, T., Muñoz-García, A. B., and Freitag, M. Conductivity in Thin Films of Transition Metal Coordination Complexes. ACS Appl. Energy Mater. 2023, 6, 4, 2122–2127

[85] Benesperi, I., Singh, R., Freitag, M. Copper Coordination Complexes for Energy-Relevant Applications. Energies. 2020, 13(9), 2198.

[86] Fagiolari, L., Varaia, E., Mariotti, N., Bonomo, M., Barolo, C., Bella, F. Poly(3,4-ethylenedioxythiophene) in Dye-Sensitized Solar Cells: Toward Solid-State and Platinum-Free Photovoltaics, Advanced Sustainable Systems. 2021, 5, 11.2100025.

[87] Wei, W., Wang, H., Hu, Y. H. A review on PEDOT-based counter electrodes for dye-sensitized solar cells. *Int J Energy Res*. 2014, 38, 9, 1099–1111.

[88] Marchini, E., Caramori, S., Bignozzi, C. A., Carli, S. On the Use of PEDOT as a Catalytic Counter Electrode Material in Dye-Sensitized Solar Cells. Applied Sciences. 2021, 11(9), 3795.

[89] Reich, N., Van Sark, W., Turkenburg, W. Charge yield potential of indoor-operated solar cells incorporated into Product Integrated Photovoltaic (PIPV). Renewable Energy. 2011, 36(2), 642-647.

[90] Ursu, D., Casut, C., Albulescu, D., Vajda, M., Mosoarca, C., Miclau, M. Enhanced Indoor Conversion Efficiency of Dye-Sensitized Solar Cells by Optimizing Ball-Milling Process of $TiO_2$ Paste. Coatings. 2024, 14(3), 283.

[91] Müller, M. F. Indoor Photovoltaics Materials, Modeling and Applications. Wiley. 2020, pp. 304. ISBN: 1119605598

[92] Michaels, H., Rinderle, M., Benesperi, I., Freitag, R., Gagliard, A., Freitag, M. Emerging indoor photovoltaics for self-powered and self-aware IoT towards sustainable energy management. Chem. Sci., 2023,14, 5350-5360.

[93] Devadiga, D., Selvakumar, M., Shetty, P., Santosh, M. S. Dye-Sensitized Solar Cell for Indoor Applications: A Mini-Review. Journal of Electronic Materials. Springer 2021, 50, 6., pp. 3187–3206.

[94] Hora, C., Santos, F., Sales, M. G. F., Ivanou, D., Mendes, A. Dye-sensitized solar cells for efficient solar and artificial light conversion. ACS Sustainable Chem. Eng. 2019, 7, 15, 13464–13470.

[95] Mathews, I., Kantareddy, S. N., Buonassisi, T., Peters, I. M. Technology and Market Perspective for Indoor Photovoltaic Cells. Joule. 2019, 3, 1415–1426.

[96] Boschloo, G.; Lindström, H.; Magnusson, E.; Holmberg, A.; Hagfeldt, A. Optimization of dye-sensitized solar cells prepared by compression method. J. Photochem. Photobiol. A Chem. 2002, 148, 11–15.

[97] Yugis, A.R.; Mansa, R.F.; Sipaut, C.S. Review on metallic and plastic flexible dye sensitized solar cell. IOP Conf. Ser. Mater. Sci. Eng. 2015, 78, 012003.

[98] Zhang, D.; Yoshida, T.; Minoura, H. Low Temperature Synthesis of Porous Nanocrystalline $TiO_2$ Thick Film for Dye-Sensitized Solar Cells by Hydrothermal Crystallization. Chem. Lett. 2002, 31, 874–875.

[99] Zhang, D.; Yoshida, T.; Furuta, K.; Minoura, H. Hydrothermal preparation of porous nano-crystalline $TiO_2$ electrodes for flexible solar cells. J. Photochem. Photobiol. A Chem. 2004, 164, 159–166.

[100] Weerasinghe, H.C.; Sirimanne, P.M.; Franks, G.V.; Simon, G.P.; Cheng, Y.B. Low temperature chemically sintered nano-crystalline $TiO_2$ electrodes for flexible dye-sensitized solar cells. J. Photochem. Photobiol. A Chem. 2010, 213, 30–36.

[101] Weerasinghe, H.C.; Franks, G.V.; Plessis, J.D.; Simon, G.P.; Cheng, Y.B. Anomalous rheological behavior in chemically modified $TiO_2$ colloidal pastes prepared for flexible dye-sensitized solar cells. J. Mater. Chem. 2010, 20, 9954–9961.

[102] Holliman, P.J.; Connell, A.; Davies, M.; Carnie, M.; Bryant, D.; Jones, E.W. Low temperature sintering of aqueous $TiO_2$ colloids for flexible, co-sensitized dye-sensitized solar cells. Mater. Lett. 2019, 236, 289–291.

[103] Sasi, S.; Chandran, A.; Sugunan, S.K.; Krishna, A.C.; Nair, P.R.; Peter, A.; Shaji, A.N.; Subramanian, K.R.V.; Pai, N.; Mathew, S. Flexible Nano-$TiO_2$ Sheets Exhibiting Excellent Photocatalytic and Photovoltaic Properties by Controlled Silane Functionalization Exploring the New Prospects ofWastewater Treatment and Flexible DSSCs. ACS Omega 2022, 7, 25094–25109.

[104] Kijitori, Y.; Ikegami, M.; Miyasaka, T. Highly efficient plastic dye-sensitized photoelectrodes prepared by low-temperature binder-free coating of mesoscopic titania pastes. Chem. Lett. 2007, 36, 190–191.

[105] Miyasaka, T.; Ikegami, M.; Kijitori, Y. Photovoltaic Performance of Plastic Dye-Sensitized Electrodes Prepared by Low-Temperature Binder-Free Coating of Mesoscopic Titania. J. Electrochem. Soc. 2007, 154, A455.

[106] Li, X.; Lin, H.; Li, J.; Wang, N.; Lin, C.; Zhang, L. Chemical sintering of graded $TiO_2$ film at low-temperature for flexible dye-sensitized solar cells. J. Photochem. Photobiol. A Chem. 2008, 195, 247–253.

[107] Zhang, D.; Downing, J.A.; Knorr, F.J.; McHale, J.L. Room-temperature preparation of nanocrystalline $TiO_2$ films and the influence of surface properties on dye-sensitized solar energy conversion. J. Phys. Chem. B. 2006, 110, 21890–21898.

[108] Weerasinghe, H.C.; Sirimanne, P.M.; Simon, G.P.; Cheng, Y.B. Fabrication of efficient solar cells on plastic substrates using binder-free ball milled titania slurries. J. Photochem. Photobiol. A Chem. 2009, 206, 64–70.

[109] Dürr, M.; Schmid, A.; Obermaier, M.; Rosselli, S.; Yasuda, A.; Nelles, G. Low-temperature fabrication of dye-sensitized solar cells by transfer of composite porous layers. Nat. Mater. 2005, 4, 607–611.

[110] Kim, H.; Piqué, A.; Kushto, G.P.; Auyeung, R.C.Y.; Lee, S.H.; Arnold, C.B.; Kafafi, Z.H. Dye-sensitized solar cells using laser processing techniques. In Photon Processing in Microelectronics and Photonics, 3rd ed.; Dubowski, J.J., Geohegan, D.B., Träger, F., Herman, P.R., Fieret, J., Pique, A., Okada, T., Bachmann, F.G., Hoving, W., Washio, K., et al., Eds.; Proceedings of SPIE; The International Society for Optical Engineering: Bellingham, WA, USA, 2004; Volume 5339, p. 5339A-48.

[111] Kim, H.; Auyeung, R.C.Y.; Ollinger, M.; Kushto, G.P.; Kafafi, Z.H.; Piqué, A. Laser-sintered mesoporous $TiO_2$ electrodes for dye-sensitized solar cells. Appl. Phys A 2006, 83, 73–76.

[112] Yang, L.; Wu, L.; Wu, M.; Xin, G.; Lin, H.; Ma, T. High-efficiency flexible dye-sensitized solar cells fabricated by a novel friction-transfer technique. Electrochem Commun. 2010, 12, 1000–1003.

[113] Lindström, H.; Holmberg, A.; Magnusson, E.; Malmqvist, L.; Hagfeldt, A. A new method to make dye-sensitized nano-crystalline solar cells at room temperature. J. Photochem. Photobiol. A Chem. 2001, 145, 107–112.

[114] Lindström, H.; Boschloo, G.; Lindquis, S.-E.; Hagfeldt, A. A New Method for Manufacturing Dye-Sensitized Solar Cells on Plastic Substrates. In Molecules as Components of Electronic Devices—ASC Symposium Series 844; Marya, L., Ed.; American Chemical Society: Washington, DC, USA, 2003; pp. 123–132.

[115] Senthilarasu, S.; Peiris, T.A.N.; García-Cañadas, J.; Wijayantha, K.G.U. Preparation of nanocrystalline $TiO_2$ electrodes for flexible dye-sensitized solar cells: Influence of mechanical compression. J. Phys. Chem. C 2012, 116, 19053–19061.

[116] Zhao, X.; Lin, H.; Li, X.; Li, J. The effect of compression on electron transport and recombination in plastic $TiO_2$ photoanodes. Electrochim. Acta 2011, 56, 6401–6405..

[117] Zhao, X.; Lin, H.; Li, X.; Li, J. The effect of compression on electron transport and recombination in plastic $TiO_2$ photoanodes. Electrochim. Acta 2011, 56, 6401–6405..

[118] Yang, H.; Liu,W.; Xu, C.; Fan, D.; Cao, Y.; Xue,W. Laser sintering of TiO2 films for flexible dye-sensitized solar cells. Appl. Sci. 2019, 9., 823.

[119] Huang, W.M.; Tsai, J.K.; Wu, T.C.; Meen, T.H. Improvement of Dye-sensitized Solar Cells by Using Compact and Pressed Layer of $TiO_2$. In Proceedings of the 2022 5th

IEEE International Conference on Knowledge Innovation and Invention, Hualien, Taiwan, 22–24 July 2022; pp. 63–68.

[120] Weerasinghe, H.C.; Sirimanne, P.M.; Simon, G.P.; Cheng, Y.-B. Cold isostatic pressing technique for producing highly efficient flexible dye-sensitized solar cells on plastic substrates. Prog. Photovolt. 2012, 20, 321–332.

[121] Karuppuchamy, S., Nonomura, K., Yoshida, T., Sugiura, T., Minoura, H. Cathodic electrodeposition of oxide semiconductor thin films and their application to dye-sensitized solar cells. Solid State Ionics. 2002, 151(1-4), 19-27.

[122] Tan, W.; Chen, J.; Zhou, X.; Zhang, J.; Lin, Y.; Li, X.; Xiao, X. Preparation of nanocrystalline $TiO_2$ thin film at low temperature and its application in dye-sensitized solar cell. J. Solid State Electrochem. 2009, 13, 651–656.

[123] Miyasaka, T.; Kijitori, Y. Low-Temperature Fabrication of Dye-Sensitized Plastic Electrodes by Electrophoretic Preparation of Mesoporous $TiO_2$ Layers. J. Electrochem. Soc. 2004, 151, A1767.

[124] Ferrere, S.; Gregg, B.A. Large increases in photocurrents and solar conversion efficiencies by UV illumination of dye sensitized solar cells. J. Phys. Chem. B. 2001, 105, 7602–7605.

[125] Rawolle, M.; Niedermeier, M.A.; Kaune, G.; Perlich, J.; Lellig, P.; Memesa, M.; Cheng, Y.-J.; Gutmann, J.S.; Müller-Buschbaum, P. Fabrication and characterization of nanostructured titania films with integrated function from inorganic–organic hybrid materials. Chem. Soc. Rev. 2012, 41, 5131–5142.

[126] Orilall, M.C.;Wiesner, U. Block copolymer based composition and morphology control in nanostructured hybrid materials for energy conversion and storage: Solar cells, batteries, and fuel cells. Chem. Soc. Rev. 2011, 40, 520–535.

[127] Nilsson, E.; Sakamoto, Y.; Palmqvist, A.E.C. Low-temperature synthesis and HRTEM analysis of ordered mesoporous anatase with tunable crystallite size and pore shape. Chem. Mater. 2011, 23, 2781–2785.

[128] Shibata, H.; Ogura, T.; Mukai, T.; Ohkubo, T.; Sakai, H. Direct synthesis of mesoporous titania particles having a crystalline wall. J. Am. Chem. Soc. 2005, 127, 16396–16397.

[129] Longo, C.; Nogueira, A.F.; De Paoli, M.A.; Cachet, H. Solid-state and flexible dye-sensitized $TiO_2$ solar cells: A study by electrochemical impedance spectroscopy. J. Phys. Chem. B 2002, 106, 5925–5930..

[130] Longo, C.; Freitas, J.; De Paoli, M.A. Performance and stability of $TiO_2$/dye solar cells assembled with flexible electrodes and a polymer electrolyte. J. Photochem. Photobiol. A Chem. 2003, 159, 33–39.

[131] Haseloh, S.; Choi, S.Y.; Mamak, M.; Coombs, N.; Petrov, S.; Choprab, N.; Ozin, G.A. Towards flexible inorganic ‘mesomaterials’:One-pot low temperature synthesis of mesostructured nanocrystalline titania. Chem. Commun. 2004, 4, 1460–1461..

[132] Gutiérrez-Tauste, D.; Zumeta, I.; Vigil, E.; Hernández-Fenollosa, M.A.; Domènech, X.; Ayllón, J.A. New low-temperature preparation method of the $TiO_2$ porous

photoelectrode for dye-sensitized solar cells using UV irradiation. J. Photochem. Photobiol. A Chem. 2005, 175, 165–171.

[133] Nemoto, J.; Sakata, M.; Hoshi, T.; Ueno, H.; Kaneko, M. All-plastic dye-sensitized solar cell using a polysaccharide film containing excess redox electrolyte solution. J. Electroanal. Chem. 2007, 599, 23–30.

[134] Tebby, Z.; Babot, O.; Toupance, T.; Park, D.H.; Campet, G.; Delville, M.H. Low-temperature UV-processing of nano-crystalline nanoporous Thin $TiO_2$ films: An original route toward plastic electrochromic systems. Chem. Mater. 2008, 20, 7260–7267..

[135] Tebby, Z.; Babot, O.; Michau, D.; Hirsch, L.; Carlos, L.; Toupance, T. A simple route towards low-temperature processing of nanoporous thin films using UV-irradiation: Application for dye solar cells. J. Photochem. Photobiol. A Chem. 2009, 205, 70–76..

[136] Miyasaka, T.; Kijitori, Y.; Murakami, T.N.; Kimura, M.; Uegusa, S. Efficient Nonsintering Type Dye-sensitized Photocells Based on Electrophoretically Deposited $TiO_2$ Layers. Chem. Lett. 2002, 31, 1250–1251.

[137] Murakami, T.N.; Kijitori, Y.; Kawashima, N.; Miyasaka, T. UV Light-assisted Chemical Vapor Deposition of $TiO_2$ for Efficiency Development at Dye-sensitized Mesoporous Layers on Plastic Film Electrodes. Chem Lett. 2003, 32, 1076–1077.

[138] Murakami, T.N.; Kijitori, Y.; Kawashima, N.; Miyasaka, T. Low temperature preparation of mesoporous $TiO_2$ films for efficient dye-sensitized photoelectrode by

chemical vapor deposition combined with UV light irradiation. J. Photochem. Photobiol. A Chem. 2004, 164, 187–191.

[139] Uchida, S.; Tomiha, M.; Takizawa, H.; Kawaraya, M. Flexible dye-sensitized solar cells by 28 GHz microwave irradiation. J. Photochem. Photobiol. A Chem. 2004, 164, 93–96.

[140] Kado, T.; Yamaguchi, M.; Yamada, Y.; Hayase, S. Low Temperature Preparation of Nano-porous $TiO_2$ Layers for Plastic Dye Sensitized Solar Cells. Chem. Lett. 2003, 32, 1056–1057.

[141] Yamaguchi, T.; Tobe, N.; Matsumoto, D.; Arakawa, H. Highly efficient plastic substrate dye-sensitized solar cells using a compression method for preparation of $TiO_2$ photoelectrodes. Chem. Commun. 2007, 45, 4767–4769.

[142] Yamaguchi, T.; Tobe, N.; Matsumoto, D.; Nagai, T.; Arakawa, H. Highly efficient plastic-substrate dye-sensitized solar cells with validated conversion efficiency of 7.6%. Sol. Energy Mater. Sol. Cells 2010, 94, 812–816.

[143] Grinis, L.; Dor, S.; Ofir, A.; Zaban, A. Electrophoretic deposition and compression of titania nanoparticle films for dye-sensitized solar cells. J. Photochem. Photobiol. A Chem. 2008, 198, 52–59.

[144] Miyoshi, K.; Numao, M.; Ikegami, M.; Miyasaka, T. Effect of Thin $TiO_2$ Buffer on the Performance of Plastic-based Dye-sensitized Solar Cells Using Indoline Dye. Electrochemistry 2007, 76, 158–160.

[145] Lee, K.-M.; Wu, S.-J.; Chen, C.-Y.; Wu, C.-G.; Ikegami, M.; Miyoshi, K.; Miyasaka, T.; Ho, K.-C. Efficient and stable plastic dye-sensitized solar cells based on a high light-harvesting ruthenium sensitizer. J. Mater. Chem. 2009, 19, 5009–5015.

[146] Morita, S.; Ikegami, M.; Wei, T.C.; Miyasaka, T. Quantum conversion enhancement with $TiO_x$ compact layers for ITO-plastic-film based low-temperature-processed dye-sensitized photoelectrodes. Chem. Phys. Chem. 2014, 15, 1190–1193.

[147] Haque, S.A.; Palomares, E.; Upadhyaya, H.M.; Otley, L.; Potter, R.J.; Holmes, A.B.; Durrant, J.R. Flexible dye sensitized nanocrystalline semiconductor solar cells. Chem. Commun. 2003, 3, 3008–3009..

[148] Lee, K.-M.; Hsu, Y.-C.; Ikegami, M.; Miyasaka, T.; Thomas, K.R.J.; Lin, J.T.; Ho, K.-C. Co-sensitization promoted light harvesting for plastic dye-sensitized solar cells. J. Power Sources 2011, 196, 2416–2421.

[149] Kunzmann, A.; Valero, S.; Sepúlveda, Á.E.; Rico-Santacruz, M.; Lalinde, E.; Berenguer, J.R.; García-Martínez, J.; Guldi, D.M.; Serrano, E.; Costa, R.D. Hybrid Dye-Titania Nanoparticles for Superior Low-Temperature Dye-Sensitized Solar Cells. Adv. Energy Mater. 2018, 8, 1702583.

[150] Kim, J.; Lee, H.; Kim, D.Y.; Seo, Y. Resonant multiple light scattering for enhanced photon harvesting in dye-sensitized solar cells. Adv. Mater. 2014, 26, 5192–5197.

[151] Kim, J.; Lee, H.; Kim, D.Y.; Kim, S.; Seo, Y. Cobalt-based electrolytes for efficient flexible dye-sensitized solar cells. MRS Adv. 2019, 4, 481–489.

[152] Lindström, H.; Magnusson, E.; Holmberg, A.; Södergren, S.-E.; Lindquist, S.-E.; Hagfeldt, A. A new method for manufacturing nanostructured electrodes on glass substrates. Sol. Energy Mater. Sol. Cells 2002, 73, 91–101.

[153] Zhang, D.; Yoshida, T.; Minoura, H. Low-temperature fabrication of efficient porous titania photoelectrodes by hydrothermal crystallization at the solid/gas interface. Adv. Mater. 2003, 15, 814–817.

[154] Stathatos, E.; Chen, Y.; Dionysiou, D.D. Quasi-solid-state dye-sensitized solar cells employing nanocrystalline $TiO_2$ films made at low temperature. Sol. Energy Mater. Sol. Cells 2008, 92, 1358–1365.

[155] Miettunen, K.; Halme, J.; Lund, P. Segmented cell design for improved factoring of aging effects in dye solar cells. J. Phys. Chem. C 2009, 113, 10297–10302.

[156] Toivola, M.; Halme, J.; Miettunen, K.; Aitola, K.; Lund, P.D. Nanostructured dye solar cells on flexible substrates-Review. Int. J. Energy Res. 2009, 33, 1145–1160.

[157] Ma, T.; Fang, X.; Akiyama, M.; Inoue, K.; Noma, H.; Abe, E. Properties of several types of novel counter electrodes for dye sensitized solar cells. J. Electroanal. Chem. 2004, 574, 77–83.

[158] Upadhyaya, H.M.; Senthilarasu, S.; Hsu, M.H.; Kumar, D.K. Recent progress and the status of dye-sensitised solar cell (DSSC) technology with state-of-the-art conversion efficiencies. Sol. Energy Mater. Sol. Cells 2013, 119, 291–295.

[159] Wante, H.P.; Bala, S.; Romanus, I.O. Review: Low Temperature Sintering of $TiO_2$ for Dye Sensitized Solar Cells (DSSCs) Fabrication on Flexible Substrates. Eur. J. Mater. Sci. 2022, 9, 18–24.

[160] Inukai, K., Takahashi, Y., Ri, K., Shin, W. Rheological analysis of ceramic pastes with ethyl cellulose for screen-printing. Ceramics International. 2015, 41(4), 5959-5966.

[161] Biquert, J. The Physics of Solar Energy Conversion. CRC Press. 2020, pp. 470. ISBN: 1138584649

[162] Jieb, Y. A., Hossain, E. Photovoltaic Systems: Fundamentals. 1st ed. Springer. 2021, pp. 299. ISBN: 3030897796

[163] Struble J L., Ji, X. Handbook of Analytical Techniques in Concrete Science and Technology. Chapter 9: Rheology. Building Materials Science. 2001. 333-367.

[164] Asghar, H., Riaz, T., Mannan, H. A., Khan, S. M., Butt, O. M. Rheology and modeling insights into dye-sensitized solar cells (DSSCs) material: Bridging the gap to solar energy advancements. Renewable and Sustainable Energy Reviews. 2024, 193, 114298.

[165] Wagner, N. J., Mewis, J. Theory and Applications of Colloidal Suspension Rheology. Cambridge University Press. 2021. ISBN: 9781108394826

[166] Malkin, A. Y., Isayev, A. I. Rheology : concepts, methods, and applications. 2nd ed. ChemTec Publishing. 2012. ISBN: 978-1-895198-49-2

[167] Pujala, R. K., Dispersion Stability, Microstructure and Phase Transition of Anisotropic Nanodiscs. 2014th ed. Springer. 2014. ISBN: 978-3319045542

[168] Adamczyk, Z., Weroński, P. Application of the DLVO theory for particle deposition problems. Advances in Colloid and Interface Science. 1999, 83(1-3), 137-226.

[169] Syrrokostas, G., Leftheriotis, G., Yianoulis, P. Effect of acidic additives on the structure and performance of TiO2 films prepared by a commercial nanopowder for dye-sensitized solar cells. Renewable Energy. 2014, 72, 164-173.

[170] Danielsson, K., Persson, P., Gallego-Urrea, J., Abbas, Z., Rosenqvist, J., & Jonsson, C. Effects of the adsorption of NOM model molecules on the aggregation of TiO2 nanoparticles in aqueous suspensions. NanoImpact. 2018, 10, 177-187.

[171] Delforce, L., Hofmann, E., Nardello-Rataj, V., Aubry, J. $TiO_2$ nanoparticle dispersions in water and nonaqueous solvents studied by gravitational sedimentation analysis: Complementarity of Hansen Parameters and DLVO interpretations. Colloids and Surfaces A: Physicochemical and Engineering Aspects. 2021, 628, 127333.

[172] Gonzalez, Z., Yus, J., Sanchez-Herencia, A., Dewalque, J., Manceriu, L., Henrist, C., Ferrari, B. A colloidal approach to prepare binder and crack-free $TiO_2$ multilayer coatings from particulate suspensions: Application in DSSCs. Journal of the European Ceramic Society. 2019, 39(2-3), 366-375.

[173] Xu, Y., Shimizu, W., Xin, Y., Kato, K., Shirai, T. Effect of the ball milling process on surface hydration behavior of ceramic powder. Ceramics International. 2024, 50(11), 20790-20795.

[174] Vigneswari, M., Madhubala, V., Nagarajan, C., Sudha Periathai, R., Jeyapriya, R., Meenambigai, A. Power and efficiency of photovoltaic cell enhanced by Ce-

$Zn_2V_2O_7$:$V_2O_5$ multiphase nanoperovskite. Inorganic Chemistry Communications. 2023, 153, 110765.

[175] Malevu, T. Ball Milling synthesis and characterization of highly crystalline $TiO_2$-ZnO hybrids for photovoltaic applications. Physica B: Condensed Matter. 2021, 621, 413291.

[176] Ul-Hamid, A. A Beginners' Guide to Scanning Electron Microscopy. Springer. 2018, pp. 402. ISBN: 3319984810

[177] C. Suryanarayana and M. G. Norton, *X-Ray Diffraction*. Boston, MA: Springer US, 1998. doi: 10.1007/978-1-4899-0148-4.

[178] Waseda, Y. Matsubara, E. Shinoda, K. X-Ray Diffraction Crystallography X-Ray Diffraction Crystallography Introduction, Examples and Solved Problems. Springer. 2011. ISBN: 978-3642442551.

[179] Ramakrishnan, V. Biophysical Characterization of Functional Peptides. Springer Protocols. Humana Press. 2023, pp. 260. eBook ISBN: 978-1-0716-3405-9.

[180] Abidi, N. FTIR Microspectroscopy: Selected Emerging Applications. Springer International Publishing, 2022, pp. 134. eBook ISBN: 978-3-030-84426-4

[181] Perkampus, H .H. UV-VIS Spectroscopy and Its Applications. Springer Berlin Heidelberg. 1992, pp. 244, ISBN: 978-3-642-77479-9

[182] Navathe, G. J., Prasad, S. R., Mane, A. M., Barge, S. H., Dongale, T. D., Shaikh, V., Karanjkar, M. M., Teli, S. B., Patil, P. S., Prasad, N. R. A Critical Review on Design

and Development of New Generation Energy Storage Devices. ES Energy & Environment, 2022, 17, 11-32

[183] Rhee, S. W., Kwon, W. Key technological elements in dye-sensitized solar cells (DSC)," Korean Journal of Chemical Engineering. 2011, 28, 7, 1481–1494.

[184] Lasia, A., Electrochemical Impedance Spectroscopy and its Applications. Springer. 2014, pp. 367. ISBN: 978-1-4939-5126-0.

[185] Srinivasan, R., Fasmin, F. An Introduction to Electrochemical Impedance Spectroscopy. 1st ed. Boca Raton. CRC Press. 2021, pp. 262. eBook ISBN: 9781003127932

[186] García-Rodríguez, R., Jiang, R., Canto-Aguilar, E. J., Oskam, G., Boschloo, G. Improving the mass transport of copper-complex redox mediators in dye-sensitized solar cells by reducing the inter-electrode distance. Phys. Chem. Chem. Phys., 2017,19, 32132-32142.

[187] Feldt, S. M., Lohse, P. W., Kessler, F., Nazeeruddin, M. K., Grätzel, M., Boschloo, G., Hagfeldt, A. Regeneration and recombination kinetics in cobalt polypyridine based dye-sensitized solar cells, explained using Marcus theory. Phys. Chem. Chem. Phys., 2013,15, 7087-7097.

[188] Fabregat-Santiago, F., Bisquert, J., Palomares, E., Otero, L., Kuang, D., Zakeeruddin, S. M., Grätzel, M. Correlation between Photovoltaic Performance and Impedance Spectroscopy of Dye-Sensitized Solar Cells Based on Ionic Liquids. J. Phys. Chem. C 2007, 111, 17, 6550–6560.

[189] Guillén, E.; Fernández-Lorenzo, C.; Alcántara, R.; Martín-Calleja, J.; Anta, J.A. Solvent-free ZnO dye-sensitized solar cells. Sol. Energy Mater. Sol. Cells 2009, 93, 1846–1852.

[190] Juang, S.S.-Y.; Lin, P.-Y.; Lin, Y.-C.; Chen, Y.-S.; Shen, P.-S.; Guo, Y.-L.; Wu, Y.-C.; Chen, P. Energy harvesting under dim-light condition with dye-sensitized and perovskite solar cells. Front. Chem. 2019, 7, 209.

[191] Idígoras, J.; Pellejà, L.; Palomares, E.; Anta, J.A. The redox pair chemical environment influence on the recombination loss in dye-sensitized solar cells. J. Phys. Chem. C 2014, 118, 3878–3889.

[192] Holliman, P.J.; Mohsen, M.; Connell, A.; Kershaw, C.P.; Meza-Rojas, D.; Jones, E.W.; Geatches, D.; Sen, K.; Hsiao, Y.-W. Double linker triphenylamine dyes for dye-sensitized solar cells. Energies 2020, 13, 4637.

[193] Sharma, K.; Sharma, V.; Sharma, S.S. Dye-Sensitized Solar Cells: Fundamentals and Current Status. Nanoscale Res. Lett. 2018, 13, 381.

[194] Boschloo, G.; Hagfeldt, A. Characteristics of the iodide/triiodide redox mediator in dye-sensitized solar cells. Acc. Chem. Res. 2009, 42, 1819–1826.

[195] Kalaignan, G.P.; Kang, Y.S. A review on mass transport in dye-sensitized nanocrystalline solar cells. J. Photochem. Photobiol. C. 2006, 7, 17–22.

[196] Zhang, D.; Downing, J.A.; Knorr, F.J.; McHale, J.L. Room-temperature preparation of nanocrystalline $TiO_2$ films and the influence of surface properties on dye-sensitized solar energy conversion. J. Phys. Chem. B. 2006, 110, 21890–21898.

[197] Biswas, S.; Kim, H. Solar cells for indoor applications: Progress and development. Polymers 2020, 12, 1338.

[198] De Rossi, F.; Pontecorvo, T.; Brown, T.M. Characterization of photovoltaic devices for indoor light harvesting and customization of flexible dye solar cells to deliver superior efficiency under artificial lighting. Appl. Energy 2015, 156, 413–422.